PROMPT LEPTON PRODUCTION IN A PROTON BEAMDUMP EXPERIMENT

FELIX BERGSMA

PROMPT LEPTON PRODUCTION IN A PROTON BEAMDUMP EXPERIMENT

ACADEMISCH PROEFSCHRIFT

ter verkrijging van de graad van doctor in de Wiskunde en de Natuurwetenschappen aan de Universiteit van Amsterdam, op gezag van de rector magnificus prof. dr. S. K. Thoden van Velzen, in het openbaar te verdedigen in de Aula der Universiteit (Oude Lutherse Kerk, ingang Singel 411, hoek Spui) op vrijdag 23 maart 1990 te 13.30 uur.

door

FELIX BERGSMA

geboren te Amsterdam

Promotor : Prof. Dr. A. N. Diddens

Co-promotor : Dr. J. K. Panman

The work described in this thesis was part of the research program of the "Nationaal Instituut voor Kern Fysica en Hoge Energie Fysica (NIKHEF)". The author was financially supported by the "Stichting voor Fundamenteel Onderzoek der Materie (FOM)".

CONTENTS

1. INTRODUCTION

The aim of the beam dump experiment described in this thesis was to study rare sources of neutrinos in 400 GeV proton nucleus interactions, distinct from the conventional ones, such as the leptonic decay of pions, kaons and hyperons. One of these sources is, for example, the semi-leptonic decay of short-lived particles, which in this experiment consisted in majority of charmed D-mesons.

Since the cross-section of neutrinos in the energy range of this experiment is very small, a detector for these particles must be massive. The interactions of the neutrinos were registered in the CHARM neutrino detector, a calorimeter consisting of 78 marble target plates with detection elements interspersed to measure the energy deposited by interaction products of the neutrinos.
The name CHARM stands for CERN-Hamburg-Amsterdam-Rome-Moscow, the residences of the institutes participating in this experiment.

To reduce the conventional background of neutrinos produced in the decay of the abundant particles with a longer lifetime, a long target of high density (beam dump) was used in order to keep the path length of the particles in the hadronic cascade small, such that these particles had a much higher probability to interact than to decay. Copper was chosen as target material because of its good heat conductivity and reasonably high density. The short-lived particles ($\tau < 10^{-11}$ sec.) decay before they interact, thus the yield of their decay products was independent of the target density. Inspired by their short lifetime these particles are said to decay promptly.

Only neutrinos and muons penetrate downstream of the target. The muons were stopped in a long (200 m) iron shield which had at several positions gaps where the muon flux could be measured. Because of their small interaction cross-section most of the neutrinos passed through the muon shield and reached the CHARM detector, which was situated 480 m downstream of the target (see fig.14 of section 3.1).

To eliminate the conventional background, which is proportional to the inverse of the target density, two targets of different density were used. One was made of solid copper and the other one, with one-third density of the former, consisted of many copper plates with air gaps in-between. For the number of neutrino interactions in the detector one has to first order,

$$\begin{aligned} S_1 &= C+P \\ S_{1/3} &= 3C+P \end{aligned} \qquad (1)$$

in which S is the total event rate in the detector, P the prompt part and C the conventional part. From equation (1) P can be resolved if S_1 and $S_{1/3}$ are measured.

Another way of determining the conventional background is to simulate the hadronic cascade induced by 400 GeV protons in copper with Monte Carlo (MC) methods. The flux of conventional decay neutrinos and muons can be derived from the path lengths of the simulated pions, kaons and hyperons. This MC-calculation can be adjusted to yield the measured conventional muon flux in the iron shield. The neutrino flux obtained thus can then be subtracted from the total observed neutrino rate.
Also the prompt muon flux from well-known sources such as di-muonic ρ- and ω-decay has been estimated, which made it possible to investigate still unknown sources of prompt muons, to be compared with the prompt neutrino flux.

Similar experiments, performed previously, gave remarkable results: a prompt electron neutrino over muon neutrino ratio smaller than one [2], [3], [4], conflicting with e-μ universality, a prompt neutrino over anti-neutrino ratio bigger than one [3], [4], which could indicate substantial charmed baryon production and an unexplained excess of prompt muon-less events at low energies [4]. The uncertainties in these results were large and it was the aim of this experiment to clarify these matters.
In addition a value for the cross-section of D-meson production was derived, the universality of the weak coupling constant for electrons and muons was investigated and limits on the production of tau neutrinos, the production of neutral heavy scalar particles and the decay probability of neutral pions in a pair of neutrinos were obtained.

The work described in this thesis has been published in Zeitschrift fur Physik C 40 (1988) 497. In section 7.1 an acceptance calculation alternative to the published one of section 4.5.6 is described, which agrees with the latter and has a slightly reduced systematic error.

2. THEORY

Reactions involving neutrinos are governed by the so called Weak Interaction, first seen in nuclear β-decay. This type of interaction is weak relative to the electromagnetic interaction at low energies. E.g. the cross-section for $e^+e^- \rightarrow \mu^+\mu^-$ is of the order α^2/s and for $e^+e^- \rightarrow \nu\bar{\nu}$ of the order $G_F{}^2 s$ for $\sqrt{s} \ll 80$ GeV. Here $\sqrt{s}$ is the center of mass energy, $\alpha \approx 1/137$ is the fine structure constant and $G_F = 1.17\ 10^{-5}$ GeV^{-2} is the Fermi constant and $\hbar = c = 1$.

Neutrinos are fermions with spin 1/2 and have a very low mass or are massless (mass $\nu_e < 18 eV/c^2$, $\nu_\mu < 0.25$ MeV/c^2, $\nu_\tau < 35$ MeV/c^2 [93]). One of the peculiarities of neutrinos is that only their negative helicity state interacts with other particles: they are only observed with spin direction opposite to their momentum. For anti-neutrinos only the positive helicity state is active. This means that the weak interaction is not invariant under parity inversion, i.e. the probability for a certain weak process is not the same after the transformation P: $x \rightarrow -x$, $y \rightarrow -y$, $z \rightarrow -z$ and all other parameters fixed.
The weak interaction is also not invariant under charge conjugation (C = particle antiparticle interchange), it is almost invariant under CP and invariant under CPT (T = time reversal). As in QED the SU(3) symmetry of QCD is broken by the weak interaction as e.g. can be seen in the decay of $\pi \rightarrow \mu\nu_\mu$, i.e. no conservation of isospin. Still conserved are lepton number, baryon number and electric charge.
Neutrinos can change the charge of a lepton (l) or fermion (f) via the so called charged current interaction

$$\nu_l + f_1{}^c \rightarrow l^- + f_2{}^{c+1} \tag{2}$$

or can leave the charge unaltered and only exchange four-momentum via the neutral current interaction

$$\nu_l + f_1{}^c \rightarrow \nu_l + f_1{}^c \tag{3}$$

The symbol $f_n{}^c$ stands for a fermion of type n and charge c. Reaction 2 is responsible for the instability of the lightest charged hadrons, e.g. $\pi^-, K^- \rightarrow \mu^- + \nu_\mu$ and will be seen in this experiment as $\nu_\mu + N \rightarrow \mu^- + X$ (see fig.1). An example of reaction (3) occurring in this experiment is $\nu_\mu + N \rightarrow \nu_\mu + X$ (see fig.2).

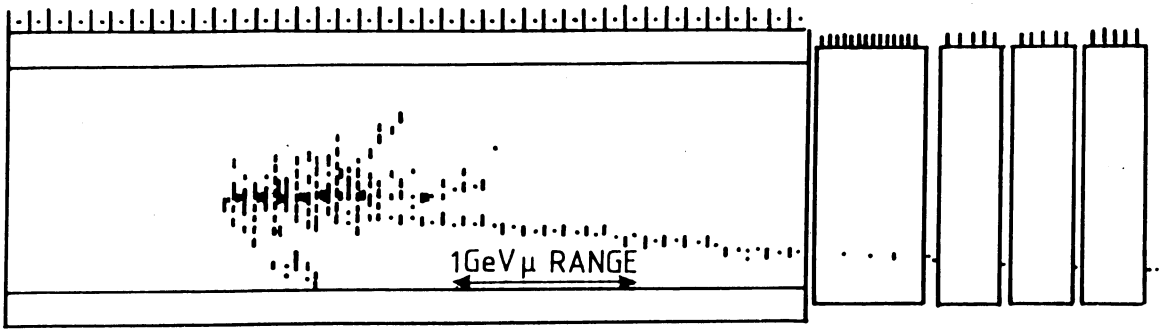

Figure 1: Example of a charged current neutrino-nucleus event in the CHARM neutrino detector. The track of the muon is clearly visible outside the hadronic shower. The neutrino beam enters the detector from the left. The bars denote hits in the scintillators, the dots denote hits in the proportional drift tubes.

2.1 THE STANDARD MODEL

At the time of writing of this thesis the best theory to describe the weak interaction is the Glashow-Salam-Weinberg (GSW) model or Standard Model [5], based on local gauge invariance using the group $SU(2)_L \times U(1)$. The group $SU(2)_L$ is necessary to include the weak interaction, the group U(1) covers the

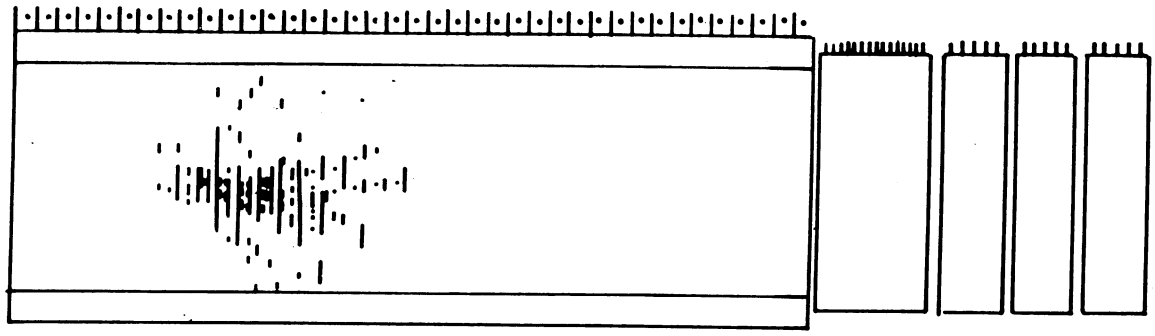

Figure 2: example of a neutral current neutrino-nucleus event in the CHARM neutrino detector. The neutrino beam enters the detector from the left. The bars denote hits in the scintillators, the dots denote hits in the proportional drift tubes.

electromagnetic interaction. The GSW model is a renormalizable theory (i.e. all possible reactions have finite cross-sections [6]) which unifies the electromagnetic and weak interaction.

Weak interactions are mediated by vector bosons in this theory, analogous to the photon in the case of the e.m. force. Since the range of the weak force is very small at low energies, these vector bosons have to be massive. Mass of the gauge fields is introduced via the Higgs mechanism, in the Standard Model with only one Higgs doublet. Three vector bosons are necessary, a positive and a negative one to account for the charged currents, called $W^{\pm}$, and a neutral one for the neutral currents, called Z^0.
The interaction between fermions and the weak vector bosons is organized in the following way:
Fermions are grouped in left-handed $SU(2)_L$ doublets generated by the third component of the weak isospin operator $T = 1/2\,\tau_1,\ 1/2\,\tau_2,\ 1/2\,\tau_3$, where τ_n are the Pauli spin matrices. For leptons one has

$$\begin{array}{lllllll} t_3 = +1/2 & \nu_e & \nu_\mu & \nu_\tau & .... & \text{charge} = 0 \\ t_3 = -1/2 & e^- & \mu^- & \tau^- & .... & \text{charge} = -1 \end{array} \qquad (4)$$

and for quarks

$$\begin{array}{lllllll} t_3 = +1/2 & \text{"up"} & \text{"charm"} & \text{"top"} & .... & \text{charge} = +2/3 \\ t_3 = -1/2 & \text{"down"} & \text{"strange"} & \text{"bottom"} & .... & \text{charge} = -1/3 \end{array} \qquad (5)$$

where t_3 stands for the eigenvalue of T_3 = the third component of the weak isospin. All right-handed fermions are singlets with $t_3 = 0$. The ν_τ lepton and the top quark have not yet been discovered.

A member of a weak $SU(2)_L$ doublet can change t_3 by a pointlike charged current interaction with a W boson:

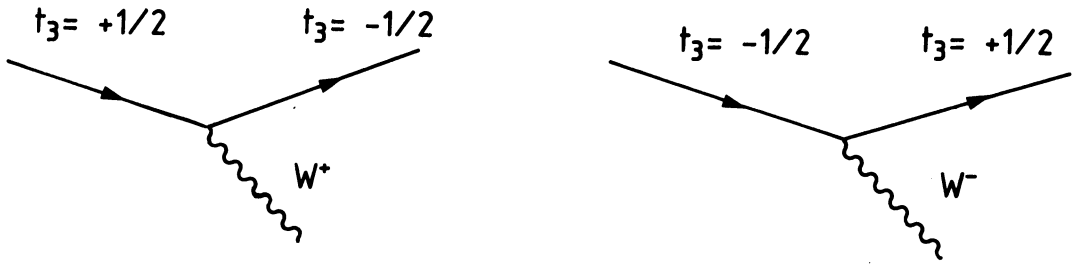

with left-handed coupling $-ig/\sqrt{2}\,\gamma_\mu(1+\gamma_5)/2$ and no right-handed coupling, where g = universal weak coupling constant and γ_n = Dirac matrices (see next section). Thus right-handed fermions and left-handed anti-fermions have no charged current interaction.

Also neutral current weak interactions are possible, without changing t_3, by exchange of a Z^0 boson:

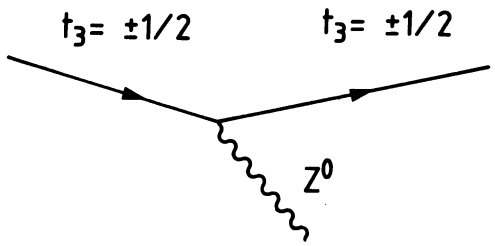

The NC interaction has also a right-handed part, created by the diagonalisation of the mass matrix of the neutral gauge fields which mixes the $SU(2)_L$ and U(1) components [5]

$$\begin{aligned} Z_\mu &= \sin\theta_W B_\mu + \cos\theta_W W_\mu{}^3 \\ A_\mu &= -\cos\theta_W B_\mu + \sin\theta_W W_\mu{}^3 \end{aligned}$$

in which θ_W = electro-weak mixing angle, Z_μ = Z boson, A_μ = photon, W^3 = third component of the $SU(2)_L$ gauge fields, B = U(1) gauge field. This results in neutral coupling constants $-ig/\cos\theta_W\gamma_\mu[g_l(1+\gamma_5)/2+g_r(1-\gamma_5)/2]$, with the left-handed and right-handed coupling constants g_l and g_r respectively,

$$\begin{aligned} g_l &= t_3 - Q\sin^2\theta_W \\ g_r &= \quad - Q\sin^2\theta_W \end{aligned} \qquad (6)$$

in which Q is the electric charge of the fermion and t_3 the weak isospin, given above. The coupling constants given in (6) imply that, except for neutrinos with Q = 0, also right-handed fermions and left-handed anti fermions participate in the neutral current interaction, which is recently confirmed by experiment [85]. The above given mixing of the neutral gauge fields is also responsible for the mass difference between W and Z:

$$M_Z = M_W/\cos\theta_W$$

With the above given vertices, the Feynman diagrams of processes (2) and (3) are given in fig.3 .

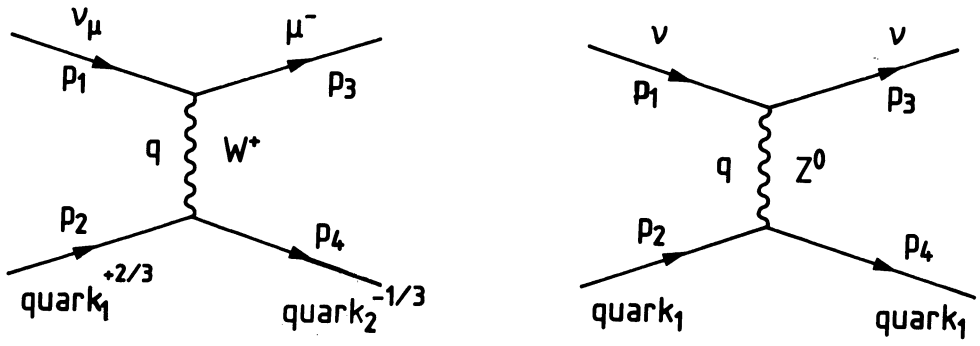

Figure 3: Feynman diagrams of charged and neutral current two body interaction.

The quark flavours of the $SU(2)_L$ doublets given in (5) do not coincide with the mass eigenstates of QCD:

$$q'_i = \Sigma_j V_{ij} q_j \tag{7}$$

in which V_{ij} is the Kobayashi-Maskawa matrix [93]. The fact that only the quarks with charge $-1/3$ mix is a question of convention. Because of the mixing (7), decays like $K^+ \rightarrow \mu\nu_\mu$ are possible, even though the weak s' and u flavour are not in the same $SU(2)_L$ doublet.

The Higgs mechanism, which is postulated to give mass to the weak intermediate vector bosons and fermions, introduces a scalar Higgs bosons (H). The Standard Model contains one neutral Higgs boson. The coupling of H to fermions is

$$g_H = -igm_f/2M_W \tag{8}$$

in which g = weak coupling constant, m_f = fermion mass and M_W = W mass. From (8) one can see that the strength of the coupling between a Higgs and a fermion is proportional to the fermion mass, thus a Higgs would decay preferably to the heaviest fermion – anti-fermion pair allowed by its own mass.

2.2 NEUTRINO-NUCLEUS INTERACTIONS

According to current knowledge nuclei are build up of nucleons, i.e. protons and neutrons, which are held together by the strong interaction. The nucleons consist of pointlike particles, quarks, which carry the quantum numbers of the nucleon and are held together by the exchange of gluons, the field quanta mediating the strong interaction.
In this section neutrino-quark interactions will be described and the momentum distribution of quarks inside the nucleon and of nucleons inside the nucleus will be treated.

2.2.1 NEUTRINO-QUARK INTERACTIONS

The cross-section for lepton-quark interaction

$$l_1(p_1) + q_1(p_2) \rightarrow l_2(p_3) + q_2(p_4) \tag{9}$$

with the four-vectors $p_n = (p_{123}, E_4)$ and mass $p_n^2 = -m_n^2$

can be written as [5]

$$d\sigma/dt = 1/128\pi \cdot |M|^2/\{(p_1 \cdot p_2)^2 - m_1^2 m_2^2\} \tag{10}$$

in which $t = q^2 = (p_1 - p_3)^2 = (p_2 - p_4)^2$ and $|M|^2$ = squared interaction amplitude, averaged over all possible spin values.
M is obtained by applying Feynman rules [7] to the graph of fig.3 and one finds:

$$M = g^2/8\, J_\mu(\text{lepton})\, [(-g^{\mu\nu} + q^\mu q^\nu)/(q^2 - M_V^2)]\, J_\nu(\text{quark}) \tag{11}$$

in which q^μ = transferred 4-momentum = $(p_3 - p_1)^\mu$, g = weak coupling constant, M_V = W,Z mass and J_μ = weak current (see below). The term between braces is the W,Z propagator, except for the mass of the weak boson, similar to the photon propagator of QED.
For the neutrino energies attained in this experiment one has $q^2 \ll M_V^2$ and (11) can be written as

$$M = G_F/\sqrt{2}\, J_\mu(\text{lepton}) J^\mu(\text{quark}) \tag{12}$$

which is the old Fermi current x current formula with (CC only)

$$G_F = g^2/8M_W^2$$

For the weak currents in (12) one has:

$$J_\mu = u_1^\dagger \gamma_0 \gamma_\mu O u_2 \tag{13}$$

in which $u_{1,2}$ = Dirac spinor of resp. outgoing and incoming fermion, $\gamma_{\mu,0}$ = Dirac matrices [5], O = operator and † denotes complex conjugation.
J_μ is called a current because J_{123} can be interpreted as current density operators and J_4 as charge density operator, in analogy with QED.
The operator O can be written as:

$$O = g_l(1+\gamma_5) + g_r(1-\gamma_5)$$

The projection operator $P^\pm = (1 \pm \gamma_5)$ filters out, in case of massless fermions, the positive or negative helicity state of a Dirac spinor. The coupling constants g_l and g_r are given in the previous section for CC and NC. (The γ_5 used here differs from the one of Bjorken and Drell by a minus sign.)

The most general case of reaction (9) will have different left- and right-handed coupling constants for the lepton and quark currents, say f_l and f_r for leptons, g_l and g_r for quarks. This gives for the squared matrix elements, summed over all spin directions:

$$\begin{aligned} |M|^2 = {} & (G_F)^2 \cdot \\ & + 128\,(g_l^2 f_l^2 + g_r^2 f_r^2)\,(p_3\cdot p_4)(p_1\cdot p_2) \\ & + 128\,(g_r^2 f_l^2 + g_l^2 f_r^2)\,(p_3\cdot p_2)(p_1\cdot p_4) \\ & - 128\,(g_l^2 f_l f_r + g_r^2 f_l f_r)\, m_3 m_1 (p_4\cdot p_2) \\ & - 128\,(g_l g_r f_l^2 + g_l g_r f_r^2)\, m_4 m_2 (p_3\cdot p_1) \\ & + 512\,(g_l g_r f_l f_r)\, m_3 m_1 m_4 m_2 \end{aligned} \tag{14}$$

For anti-particles one has to make the change $g_l \leftrightarrow g_r$ or $f_l \leftrightarrow f_r$, since the spinor for an anti-particle can be written as $\gamma_0\gamma_5$ x spinor of particle and $(\gamma_0\gamma_5 u)^\dagger \gamma_0\gamma_\mu(1\pm\gamma_5)\gamma_0\gamma_5 u = u^\dagger\gamma_0\gamma_\mu(1\mp\gamma_5)u$.

Now neutrino-quark scattering in the rest frame of the quark will be considered.

If the incoming particle is a neutrino $f_l = 1$ and $f_r = 0$ as discussed in the previous section, then (14) is reduced to

$$\begin{aligned} |M_\nu|^2 = {} & (G_F)^2 \cdot \\ & + 128\, g_l^2\, (p_3\cdot p_4)(p_1\cdot p_2) \\ & + 128\, g_r^2\, (p_3\cdot p_2)(p_1\cdot p_4) \\ & - 128\, g_l g_r\, m_4 m_2 (p_3\cdot p_1) \end{aligned} \tag{15}$$

For incoming neutrinos equation (10) becomes:

$$d\sigma/dt = 1/128\pi\, |M_\nu|^2/(p_1\cdot p_2)^2 \tag{16}$$

The four-momentum of the quark in its rest frame is $(0,m_2)$ and any product $(p_2\cdot p_n)$ can be written as

$$(p_2\cdot p_n) = -m_2 E_n \tag{17}$$

A quantity which can be determined experimentally is the fraction y of the neutrino energy transferred to the quark, in the rest frame of the quark:

$$y = p_2\cdot q/p_2\cdot p_1 = (E_4 - m_2)/E_1 \tag{18}$$

The last equality is only true in the restframe of the quark.
For t in (16) one has, using (17)

$$t = q^2 = (p_2 - p_4)^2 = 2m_2E_4 - m_2^2 - m_4^2 = 2m_2E_1y + m_2^2 - m_4^2$$

and

$$dt = 2m_2E_1dy = -2(p_1.p_2)dy \tag{19}$$

Substituting (19), (17) and (15) in (16) one finds for the first term in (15)

$$d\sigma/dy = G_F^2/\pi\ g_l^2\ 2m_2E_1\ [\ 1 - (m_2^2 - m_4^2 - m_3^2)/2m_2E_1\ ] \tag{20}$$

for the second term

$$d\sigma/dy = G_F^2/\pi\ g_r^2\ 2m_2E_1\ [\ 1-y]\ [\ 1-y+(m_2^2 - m_4^2 + m_3^2)/2m_2E_1\ ] \tag{21}$$

and for the third term

$$d\sigma/dy = G_F^2/\pi\ g_lg_r\ m_2m_4\ [\ y+(m_2^2 - m_4^2 + m_3^2)/2m_2E_1\ ] \tag{22}$$

At the energies considered here, in most of the cases only the lightest quarks (u,d) will be produced in (9), which means $m_2 \approx m_4$ and the terms involving the particle masses in (20)-(22) reduce to

$$\pm m_3^2/2m_2E_1$$

The outgoing lepton will be in most cases not heavier than the muon, thus $m_3 \leq 0.106$ GeV/c^2 and since in this experiment a cut of 2 GeV in neutrino energy is made, the terms involving the particle masses in (20)-(22) will be negligible in most cases.
For heavy quark or heavy lepton production one can only neglect the mass terms if

$$E_\nu \gg m_h^2/2m_{u,d} \tag{23}$$

in which m_h = mass of heavy quark or lepton, $m_{u,d}$ = mass of up, down quark.
Neglecting the terms involving the particle masses in (20)-(22) one gets:

$$d\sigma/dy = (G_F^2/\pi)\ s\ [\ g_l^2 + g_r^2(1-y)^2 - g_lg_rm_2m_4y\ ]$$

where $\sqrt{s}$ = center of mass energy of neutrino-quark system. When $E_\nu \gg m_2m_4$ also the interference term can be neglected

$$d\sigma/dy = (G_F^2/\pi)\ s\ [\ g_l^2 + g_r^2(1-y)^2\ ] \tag{24}$$

For anti-quarks one has to replace $g_l \leftrightarrow g_r$:

$$d\sigma/dy = (G_F^2/\pi)\ s\ [\ g_r^2 + g_l^2(1-y)^2\ ] \tag{25}$$

Results (24) and (25) can be understood as follows:
if a left-handed neutrino scatters on a quark via a left-handed coupling

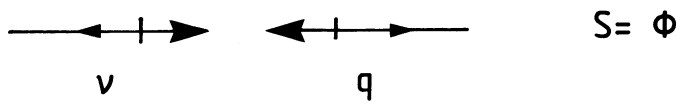

the total spin S = 0, and there is no preferred direction for the outgoing neutrino and quark.
If a right-handed anti-neutrino scatters on a quark via a left-handed coupling

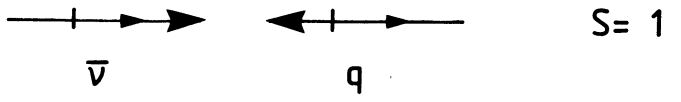

the total spin S = 1 and the case of maximal energy transfer of the anti-neutrino to the quark, which means 180^0 scattering

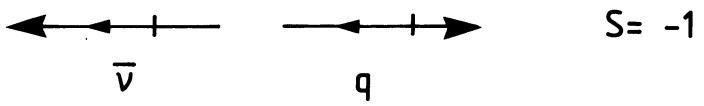

would violate conservation of angular momentum.

Table 1: Quark quantum numbers.

Flavour	Q	I_z	S	C	B	T
Down	− 1/3	− 1/2	0	0	0	0
Up	+ 2/3	+ 1/2	0	0	0	0
Strange	− 1/3	0	− 1	0	0	0
Charm	+ 2/3	0	0	1	0	0
Bottom	− 1/3	0	0	0	− 1	0
Top	+ 2/3	0	0	0	0	1

Q = charge, I_z = isospin z-component, S = strangeness, C = charm, B = bottomness, T = topness

SUMMARY

Charged current neutrino-quark scattering or anti-neutrino anti-quark scattering:

$$d\sigma/dy = (G_F^2/\pi)s \tag{26}$$

Total cross-section

$$\sigma = (G_F^2/\pi)s \tag{27}$$

Charged current anti-neutrino quark scattering or neutrino anti-quark scattering:

$$d\sigma/dy = (G_F^2/\pi)s\,(1-y)^2 \tag{28}$$

Total cross-section

$$\sigma = 1/3\,(G_F^2/\pi)s \tag{29}$$

Neutral current neutrino-quark scattering or anti-neutrino anti-quark scattering given in equation (24).

Total cross-section

$$\sigma = (G_F^2/\pi)s\,[\,g_l^2 + 1/3\,g_r^2\,] \tag{30}$$

where g_l and g_r are given in equation (6). Neutral current neutrino anti-quark scattering or anti-neutrino quark scattering given in equation (25).

Total cross-section

$$\sigma = (G_F^2/\pi)s\,[\,1/3\,g_l^2 + g_r^2\,] \tag{31}$$

2.2.2 NEUTRINO-NUCLEON INTERACTIONS

As will be described in section 2.3, the quarks inside a nucleon behave as almost free particles at large momentum transfer.
Assume a quark inside a nucleon hit by a neutrino carried a fraction x of the nucleon momentum p_N, see fig.4.

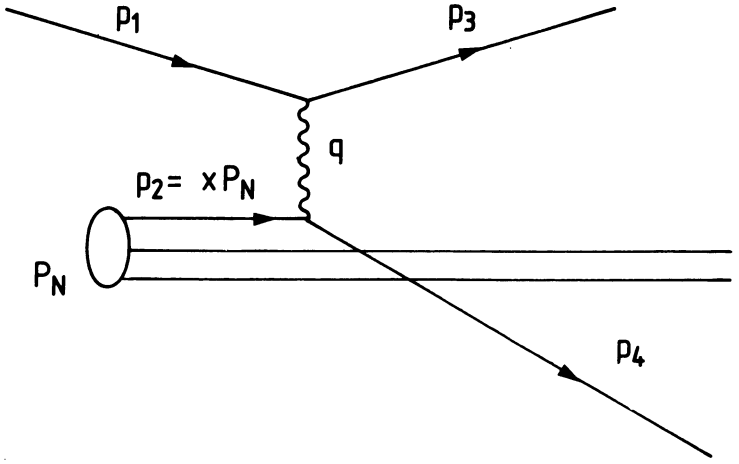

Figure 4: Neutrino nucleon scattering.

In the case of light quark (u,d,s)-production, the mass of the quark is negligible and

$$(xp_N + q)^2 = 0 \rightarrow x = -q^2/2q.p_N \tag{32}$$

further

$$Q^2 = -q^2 = -(p_1 - p_3)^2 = 2E_1E_3(1-\cos\theta) \tag{33}$$

where θ is the angle between the neutrino and the outgoing lepton and the lepton mass is neglected.
In the rest frame of the nucleon one has $p_N = (0,0,0,M)$ and

$$p_N.q = M(E_3 - E_1) \tag{34}$$

With (32), (33) and (34) one obtains

$$x = E_1E_3(1-\cos\theta)/M(E_1 - E_3) \tag{35}$$

Thus x can be determined by measuring the outgoing lepton energy and scattering angle if the neutrino energy is known.

The nucleon consists of three valence quarks, uud for the proton and udd for the neutron (see table 1), which carry its quantum numbers. The valence quarks attract each other by the exchange of gluons, the quanta of the SU(3) gauge fields of QCD.
In the gluon field of the valence quarks virtual $q\bar{q}$-pairs are created, called sea-quarks. The momentum of the nucleon is shared by valence quarks ≈ 37%, sea-quarks ≈ 14% and gluons ≈ 49%.
The momentum distribution of a certain quark inside a nucleon will be denoted by q(x), where q stands for u,d,s,c,... ; the momentum distribution of the gluons will be given by g(x). Thus one must have

$$\int_0^1 [\{\Sigma_{q,\bar{q}}\, q(x)\} + g(x)]\, dx = 1$$

The functions q(x) and g(x) are called structure functions and more details can be found in [8].

For the proton the x-distributions of u,d and s will be denoted by respectively u(x), d(x) and s(x) and more heavy quarks will be neglected, because at the energy scale of this experiment they play a role of minor importance.
Since the proton consists of uud, one must have

$$ {}_0\int^1[u(x)-\bar{u}(x)]dx/x=2 \qquad {}_0\int^1[d(x)-\bar{d}(x)]dx/x=1 \qquad {}_0\int^1[s(x)-\bar{s}(x)]dx/x=0 $$

The last term must vanish because strange quarks only appear in the sea and are thus created as quark anti-quark pairs.

Charged current interactions of a neutrino and a nucleon can only involve quarks with charge $-1/3$, $-2/3$ = d,s,$\bar{u}$ and anti-neutrino nucleon charged current interactions can only involve quarks with charge $+1/3$, $+2/3$ = $\bar{d}$, $\bar{s}$, u .
Thus for charged current neutrino proton interactions one gets with equations (26) and (28):

$$ d^2\sigma/dxdy = (G_F^2/\pi)\, s\, [\, d(x) + s(x) + \bar{u}(x)(1-y)^2\,] \tag{36} $$

where $\sqrt{s}$ is the center of mass energy of the neutrino proton system.
For charged current anti-neutrino proton interactions

$$ d^2\sigma/dxdy = (G_F^2/\pi)\, s\, [\, \bar{d}(x) + \bar{s}(x) + u(x)(1-y)^2\,] \tag{37} $$

Because of isospin symmetry the quark distribution functions for the neutron can be obtained from those of the proton by making the change $u \leftrightarrow d$ in (36) and (37). Thus e.g. the up-quark distribution of the neutron will be denoted by d(x).
For an isoscalar target N, i.e. a target with an equal amount of up and down quarks (i.e. $N_{proton} = N_{neutron}$ like marble = $CaCO_3$ with 44 protons and 44 neutrons per molecule) one has for charged current neutrino-nucleon scattering:

$$ d\sigma/dy = G_F^2/2\pi\, s\, [\, U + D + 2S + (\bar{U} + \bar{D})\,(1-y)^2\,] \tag{38} $$

and for charged current anti-neutrino nucleon scattering:

$$ d\sigma/dy = G_F^2/2\pi\, s\, [\, \bar{U} + \bar{D} + 2\bar{S} + (U + D)\,(1-y)^2\,] \tag{39} $$

where $Q = {}_0\int^1 q(x)$.
Using [5]

$$ U = 0.28 \quad D = 0.15 \quad \bar{U}=\bar{D}=0.03 \quad S=\bar{S}=0.01 \tag{40} $$

one gets for CC ν-N_{iso}:

$$ d\sigma/dy = G_F^2/2\pi\, s\, [\, 0.45 + 0.06(1-y)^2\,] \tag{41} $$

and for CC $\bar{\nu}$-N_{iso}

$$ d\sigma/dy = G_F^2/2\pi\, s\, [\, 0.08 + 0.43(1-y)^2\,] \tag{42} $$

The neutral current interaction is slightly more complicated because of the left- and right-handed couplings in equation (6).
If one denotes (see (6))

$$ \begin{aligned} (\mp 1/2 \pm 1/3\sin^2\theta_W)^2 &= G_A \\ (\pm 1/3\sin^2\theta_W)^2 &= G_B \\ (\pm 1/2 \mp 2/3\sin^2\theta_W)^2 &= G_C \end{aligned} \tag{43} $$

$$(\mp 2/3\sin^2\theta_W)^2 = G_D$$

One gets for NC ν scattering on an isoscalar target:

$$d\sigma/dy = G_f^2/2\pi\ s \cdot \tag{44}$$

$(U + D + 2S)$	$[\ G_A + G_B(1-y)^2\ ]$
$(U + D)$	$[\ G_C + G_D(1-y)^2\ ]$
$(\bar{U} + \bar{D} + 2\bar{S})$	$[\ G_B + G_A(1-y)^2\ ]$
$(\bar{U} + \bar{D})$	$[\ G_D + G_C(1-y)^2\ ]$

With (40) and $\sin^2\theta_W = 0.24$ equation (44) gives

$$d\sigma/dy = (G_F^2/2\pi)s\ [\ 0.131 + 0.035(1-y)^2\ ] \tag{45}$$

and for NC $\bar{\nu}$ scattering on an isoscalar target:

$$d\sigma/dy = G_f^2/2\pi\ s \cdot \tag{46}$$

$(U + D + 2S)$	$[\ G_B + G_A(1-y)^2\ ]$
$(U + D)$	$[\ G_D + G_C(1-y)^2\ ]$
$(\bar{U} + \bar{D} + 2\bar{S})$	$[\ G_A + G_B(1-y)^2\ ]$
$(\bar{U} + \bar{D})$	$[\ G_C + G_D(1-y)^2\ ]$

With (40) and $\sin^2\theta_W = 0.24$ equation (46) gives

$$d\sigma/dy = (G_F^2/2\pi)s\ [\ 0.035 + 0.131(1-y)^2\ ] \tag{47}$$

From (38), (39), (44) and (46) one can see that for equal fluxes of ν and $\bar{\nu}$ in a beam

$$d\sigma/dy \propto [\ 1 + (1-y)^2\ ] \tag{48}$$

for NC and, except for a small difference due to the strange sea, this is also the case for CC.

The formulae above are only true for absolutely free, massless quarks. In reality the structure functions will depend on Q^2, but for the applications in this thesis, concerning ratios of y-distributions, the above approximations are sufficiently precise (for more details concerning the Q^2-dependence of the structure functions see [8]).
Also neglected is the Fermi-motion of the nucleons inside the nucleus. The same remark is true for this approximation as for the q^2-dependence of the structure functions.

2.3 THE PRODUCTION OF HEAVY FLAVOURS IN HADRON – HADRON INTERACTIONS

Exact calculations of physical quantities (e.g. cross-sections) in field theory are usually impossible. A technique often used is to treat the interaction between fields as a perturbation of the free field case. The measurable quantities are approximated by a power series in a dimensionless variable, called coupling constant, characteristic for the interaction strength [21]. E.g. for a two body cross-section this looks like:

$$\sigma(A+B \rightarrow C+D) = N \cdot K \cdot (\ O(\alpha) + O(\alpha^2) + \ldots\ldots\ )$$

in which N = normalization factor, K = kinematical factor, α = coupling constant. This technique only works when $\alpha \ll 1$ and has proved to be very successful in QED, where $\alpha \approx 1/137$. Because of the large coupling constant of the strong interaction, calculations using perturbative expansion in QCD are in most cases impossible.

Due to vacuum polarization the effective coupling constant of the strong interaction will depend on the square of the transferred four-momentum:

$$\alpha_s(Q^2) \approx 4\pi/\{b_0 \log(Q^2/\Lambda^2)\} \tag{49}$$

in which $b_0 = 11/3 \cdot N_{colour} - 2/3 \cdot N_{flavour} = 7$ for 3 colours and 6 flavours (see [8]).
Equation (49) implies a potential proportional to distance, which confines the quarks into hadrons. The confinement range is of the order $\hbar/\Lambda$, and since the hadron size is measured to be $\approx 10^{-15}$ m , one must have $\Lambda \approx 0.2$ GeV. From (49) it follows that $\alpha_s \to 0$ if $Q^2 \to \infty$, so for highly energetic, deep inelastic reactions the quarks inside hadrons appear as almost free particles (asymptotic freedom), for which perturbative field theory is applicable. Thus, particle production at high P_t and/or high x_F in high energy hadron – hadron interactions is a good testing ground for QCD [9].

Another area where perturbative QCD might work is the production of heavy flavours. The mass of a charm quark, probed in deep inelastic electromagnetic and weak interactions, is about 1.2 GeV/c^2 , so for the production of a charmed quark anti-quark pair a minimal Q^2 of 5.8 (GeV/c)^2 is necessary, which gives with (49) $\alpha_s \approx 0.36 < 1$. This value of α_s makes it possible to apply perturbation techniques, but the higher order contributions will be non-negligible. With the next flavours, in order of increasing mass, bottom and top, higher order terms are expected to become less and less important. Unfortunately they are only produced at an energy scale which is not reachable by this experiment. The top quark has not been discovered yet.
The lowest order QCD Feynman graphs for $c\bar{c}$ production are shown in fig.5 .

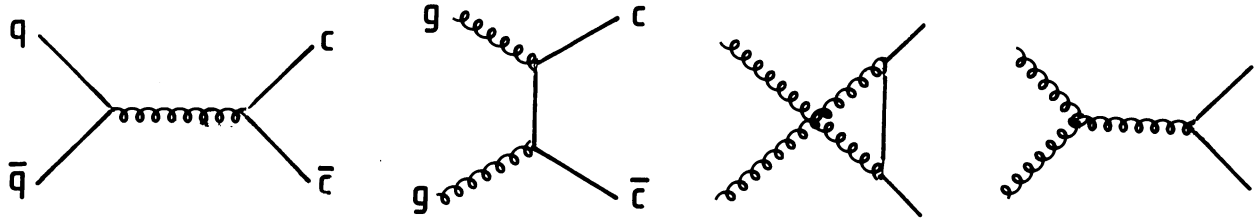

Figure 5: Feynman diagrams of quark- and gluon-fusion.

These processes are usual called quark- and gluon-fusion. See e.g. [10] for the calculation of their cross-sections. To calculate the charm cross-section in hadron – hadron interactions one needs in addition the momentum distributions of gluons, valence-quarks and sea-quarks inside the hadrons as seen by high Q^2 probes. These distributions, called structure functions, have been measured with deep inelastic scattering of electrons, muons and neutrinos on hadrons, which couple only to the electric or weak charge of the quarks inside the hadron [8]. For charm production in proton – proton collisions one gets:

$$\sigma(pp \to c\bar{c}X) = \int dx_a \int dx_b f^{g,q}(x_a) f^{g,\bar{q}}(x_b) \sigma(gg, q\bar{q} \to c\bar{c}) \tag{50}$$

where $f^{g,q}(x_a)dx_a$ = probability of heaving a gluon or quark in proton a which carries a momentum fraction between x and $x+dx$ $(0 < x < 1)$. The integration in (50) should only be carried out in a region where $x_a x_b s > (2m_c)^2$, so the result depends upon the mass of the charm quark m_c.
After the $c\bar{c}$-pair has been created in this way on a short time scale where quarks and gluons can be considered as weakly interacting particles, they can not leave the surrounding glue cloud as free quark because of the long distance confinement force: the outgoing c-quark will dress itself up with an anti-quark or two other quarks to form a colourless meson or baryon. Here perturbative QCD is not applicable anymore. The hadronization of highly energetic quarks has been parametrized with the help of fragmentation functions $D^C(z_c)$, giving the probability that an outgoing quark c produces a hadron C carrying a momentum fraction z_c of the original quark ($0 < z < 1$) [63]. In table 2 some known charmed hadrons are listed together with some parameters.
The fragmentation function has to be multiplied into the term $\sigma(gg, q\bar{q} \to c\bar{c})$ of (50). Its form can be estimated theoretically [8] and measured in e^+e^- reactions.
Calculations of this type have been carried out by e.g. [11], [90]. The LEBC-EHS collaboration [81] uses structure functions from [12], quark- and gluon-fusion sub-process cross-sections from [10] and the Lund-fragmentation model [64]. Compared with their 400 GeV p-p results it turns out that the calculated

Table 2: Some properties of charmed hadrons.

NAME	MASS [MeV/c^2]	LIFETIME [s]	BR → e+X	BR → e+ν_e	BR → μ+ν_μ
$D^\pm$	1869.3±0.6	$10.69\ ^{+0.34}_{-0.32}\ 10^{-13}$	$19.2\ ^{+2.3}_{-1.6}$ %	< 2.5%	< 7 10^{-4}
D^0	1864.5±0.6	(4.28±0.11) 10^{-13}	(7.7±1.1)%		
$D_s^\pm$	1969.3±1.1	$4.36\ ^{+0.38}_{-0.32}\ 10^{-13}$			
Λ_c^+	2284.9	$1.79\ ^{+0.23}_{-0.17}\ 10^{-13}$	(4.5±1.7) %		

cross-section is too low by a factor of ≈ 2. This is repaired by introducing a k-factor as in the Drell-Yan process [8]. A k-factor between 1.2 and 2.7 for a charm quark mass ranging from 1.2 to 1.4 GeV/c^2 is needed. The x_F-dependence of the measured and predicted cross-section from LEBC-EHS is shown in fig.6. It has been parametrized like:

$$\partial\sigma/\partial x_F \partial P_t^2 \propto (1-x_F)^n\, e^{-bP_t^2} \tag{51}$$

with $n = 4.9 \pm 0.5$ and $b = (1.0 \pm 0.1)$ (GeV/c)$^{-2}$. This value of b gives a mean P_t of 0.89 GeV/c. Compared with 800 GeV p-p data [13] the energy dependence of the charm cross-section is found compatible with the fusion model.

Some ISR experiments [14], [15] have reported substantial forward production of Λ_c in p-p interactions at $\sqrt{s} = 62$ GeV, with n of equation (51) around 2 and a cross-section ≈ 100 μb. Also other experiments find forward produced charmed hadrons, e.g. [16], [17] in neutron-nucleon and [18], [76], [83] in pion-nucleon interactions, although their cross-sections are lower than the ISR experiments. The fusion model is not able to describe these data: it gives a value around 6 for n and the total cross-section is an order of magnitude lower [19].
A solution to this is the process of flavour excitation: a charmed anti-quark in one of the hadrons is kicked out of the sea by a quark or gluon from the other hadron, the remaining c-quark recombines with two quarks of the first hadron to form a fast charmed baryon.
The flavour-excitation sub-processes (see fig.7) can be calculated reliably [10]. Since it is difficult to estimate the Q^2-dependent x-distribution of the charm-sea [11] and, also, the recombination process is subject to speculations, the uncertainties in this model are larger than in the case of fusion. In fig.8 the energy dependence of the charm cross-section as calculated by Odorico [90] is shown.
Also the contribution from fusion is indicated in this figure. Flavour-excitation decreases rapidly with growing Q^2 and is expected to be smaller than the fusion contribution in case of bottom and top production.
Another attempt to explain forward charm-production is the introduction of a Q^2-independent "charm – sea", called intrinsic charm, entirely based on non-perturbative QCD. The creation of a forward charmed hadron is then supposed to take place via diffractive scattering (see [20]). Exact calculations for this process are not possible.

The x_F-dependence of particle production near $x_F = 1$ in hadron – hadron interactions can be estimated using quark counting rules [80], which have no strong theoretical basis and are largely empirical. The most recent version reads:

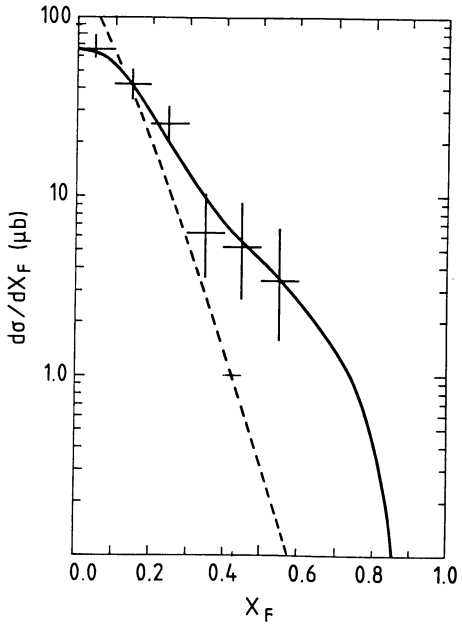

Figure 6: x_F-dependence for pp → c + X from LEBC-EHS [81]. The dashed curve shows the basic parton level prediction for quark- and gluon-fusion and the solid curve includes fragmentation effects as simulated by coloured string breaking with the Lund model.

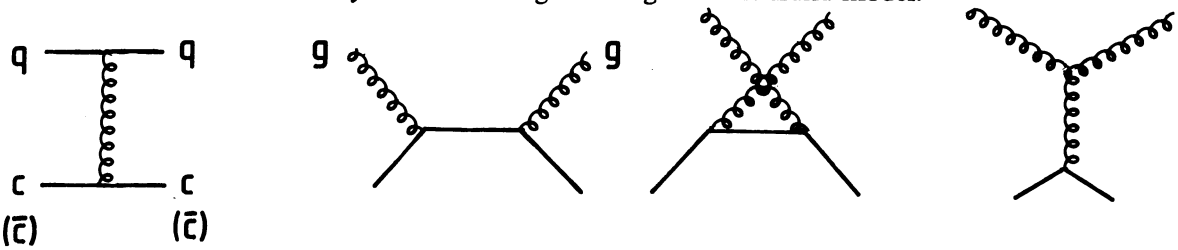

Figure 7: Feynman diagrams for flavour excitation sub-processes.

$$\partial\sigma/\partial x \propto (1-x)^{2n_H+n_{PL}-1} \tag{52}$$

in which n_H is the number of spectator quarks of the original hadron and n_{PL} is the number of spectator quarks involved in the point-like $c\bar{c}$-creation. For Λ_c-production this would mean $(1-x)^1$, similar to Λ_s production, for D-production one gets $(1-x)^3$, similar to kaon production, all for a proton as incoming projectile. The Λ_c and $\overline{D}$ from the same interaction cannot have both this x-dependence. Forward D production is much more unlikely than forward Λ_c production, as seen in forward Λ_s and K production, because in the first case two quarks of the incoming proton have to be hit instead of one.

For the cross-sections based on perturbative QCD one expects a linear dependence on the atomic weight A, i.e. proportional to the number of nucleons. In the case of diffractive production one expects a dependence proportional to $A^{2/3}$, as for the pion and kaon cross-sections, since this process is supposed to take place on the surface of the nucleus. Nuclear effects can soften the spectra at high values of x_F, so that even in case of a A^1-dependence for hadron–hadron interactions, the A exponent will become smaller for hadron-nucleus interactions at higher x_F, see Barton et al. [87] for the case of light-hadron production.

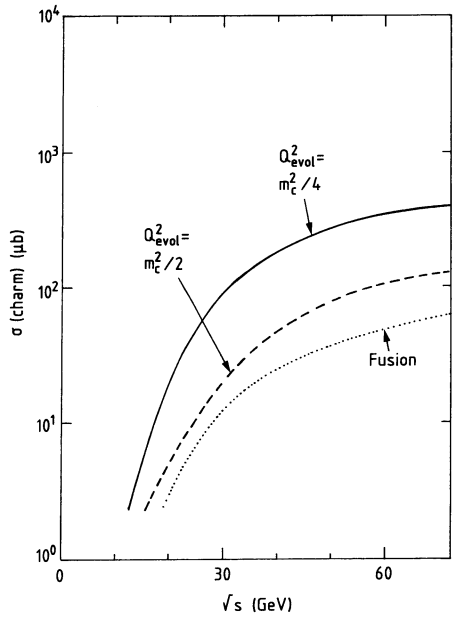

Figure 8: Energy dependence of charm cross-section as calculated by Odorico [90]. The dotted curve gives the contribution of quark- and gluon-fusion only. The dashed and the full line give the result with the contribution of flavour excitation included for different evolution scales of the charm sea. The full curve is used for calculations in this work.

2.4 (SEMI)-LEPTONIC DECAY OF CHARMED HADRONS

2.4.1 BRANCHING RATIOS FOR VARIOUS D-DECAYS.

It will be shown in this section that semi-leptonic charm-decay will give rise to an equal flux of prompt electron and muon neutrinos, according to current theories. In section 10.1.1 some theories which would cause an asymmetry in these fluxes are discussed.
The lightest charmed hadrons can only decay via the weak interaction. In fig.9 the Feynman graph for this decay in the GSW-model is given.

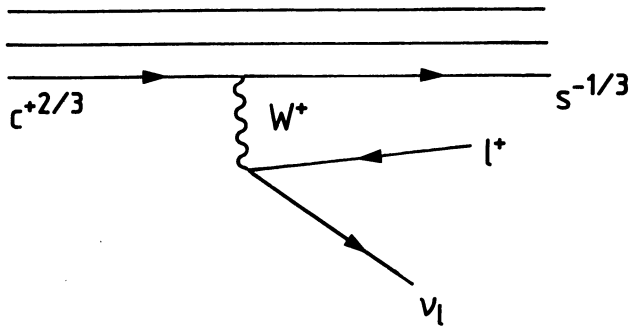

Figure 9: Charmed hadron decay.

In this model the matrix element is the same for any leptonic weak isospin doublet. Thus, because of the small mass difference between electron and muon compared to the charm quark mass, this model predicts:

$$\text{branching ratio } (c \rightarrow s\, e\, \nu_e) = \text{branching ratio } (c \rightarrow s\, \mu\, \nu_\mu)$$

In most cases the created strange quark will combine with the spectator quark(s) to form a strange hadron. Semi-leptonic branching ratios for some charmed hadrons are given in table 2 . For charged D-mesons a small probability exists of purely leptonic decay, i.e. $D^{\pm} \rightarrow l^{\pm} + \nu(\bar{\nu})$, because the mass eigenstates of the strong and weak interaction do not coincide, so the "strong" d quark is partly a "weak" s quark, which together with the charm quark can create a lepton pair via W exchange. The probability for this process is given by:

$$\Gamma(M \rightarrow l\,\nu) = G_F^2/4\pi\; f_M^2 m_l^2 m_M \{1-(m_l/m_M)^2\}^2\; U_{KM}^2 \tag{53}$$

in which G_F = Fermi constant, f_M = weak decay constant for meson M, m_M = mass of meson M, m_l = mass of lepton, U_{KM} = Kobayashi-Maskawa matrix element. The neutrino is assumed to be massless.
$\Gamma = 0$ for $m_l = 0$, because of helicity suppression. Comparing the lifetimes of $\pi^{\pm}$ and $D^{\pm}$, assuming $1 \leq f_D/f_\pi \leq 2$, Berger et al. [92] find:

$$\Gamma(D^{\pm} \rightarrow \mu^{\pm}\nu)/\Gamma(D^{\pm} \rightarrow \mu\nu_\mu X) \leq 3.6\; 10^{-3} \tag{54}$$

where a semi-leptonic branching ratio for $D^{\pm}$ of 19.2% is used. The purely leptonic decay of $D^{\pm} \rightarrow e^{\pm}\nu$ is smaller than $D^{\pm} \rightarrow \mu^{\pm}\nu$ by a factor $(m_\mu/m_e)^2$. So here is a source for asymmetry in the decays into $\nu_e - \nu_\mu$, although the magnitude is very small and in this experiment unmeasurable. The decay $D \rightarrow \tau\nu_\tau$ is according to (53) a factor $\approx$ 2 higher than $D \rightarrow \mu\nu_\mu$ and thus also negligible (a τ mass of 1.7842 GeV/c^2 was used). The decay $D \rightarrow \tau\nu_\tau X$ is not possible because the mass difference between D and τ is too small.
For the semi-leptonic decay of D_s it was assumed that $\Gamma(D_s^{\pm} \rightarrow l^{\pm}\nu X) = \Gamma(D^{\pm} \rightarrow l^{\pm}\nu X)$ because there is no conservation law known which discriminates between the two cases and the mass difference between D and D_s is small ($\approx$ 100 MeV/c^2). Taking the lifetimes for $D^{\pm}$ and $D_s^{\pm}$ and the semi-leptonic branching ratio for $D^{\pm}$ from table 2 one gets:

$$\text{branching ratio } D_s^{\pm} \rightarrow l^{\pm}\nu X \approx 8\ \% \tag{55}$$

for $l = e,\mu$.
Using (53), (54) and (55), $\tan\theta_c = 0.25$ and assuming $f_D = f_{D_s}$ one finds:

$$\text{Branching ratio } (D_s \rightarrow \mu\,\nu_\mu) \approx 0.2\ \% \tag{56}$$

Again this is not enough for a measurable asymmetry between ν_e and ν_μ. It follows from (53) that:

$$\Gamma(D_s \rightarrow \tau\nu_\tau)/\Gamma(D_s \rightarrow \mu\nu_\mu) \approx 9 \tag{57}$$

where the values of table 2 are used (and $m_\tau = 1.7842$ GeV/c^2). Equation (57) is only true if the mass of the tau neutrino is much smaller than the mass difference of 186.3 MeV/c^2 between D_s and τ. In [93] an upper limit is given of $m_{\nu_\tau} < 70$ MeV. From (56) and (57) one derives:

$$\text{Branching ratio } (D_s \rightarrow \tau\nu_\tau) \approx 2\ \% \tag{58}$$

This reaction would give rise to an excess of prompt events without a muon. Since in $\nu_\tau + N \rightarrow \tau + X$ the branching ratio $(\tau \rightarrow \mu\nu\nu) = 17.6\%$, all other decays would look like (0μ)-events; in addition the charged current ν_τ reactions are suppressed because of the high τ mass (see chapter 8).

2.4.2 LEPTON ENERGY SPECTRA IN SEMI-LEPTONIC DECAY OF HEAVY FLAVOURS

The Feynman graphs for weak decay of a charge + 2/3 quark and a charge − 1/3 quark are given in fig.10.
All particles involved have spin 1/2. Since in the weak interaction only left-handed currents are active one gets for the decay of quark Q:

$$\begin{aligned} Q^{+2/3} &\rightarrow q^{-1/3} + l^+ + \nu_l \qquad l^+ = R \qquad q^{-1/3},\ \nu_l = L \\ Q^{-1/3} &\rightarrow q^{+2/3} + l^- + \bar{\nu}_l \qquad \bar{\nu}_l = R \qquad q^{+2/3},\ l^- = L \end{aligned} \tag{59}$$

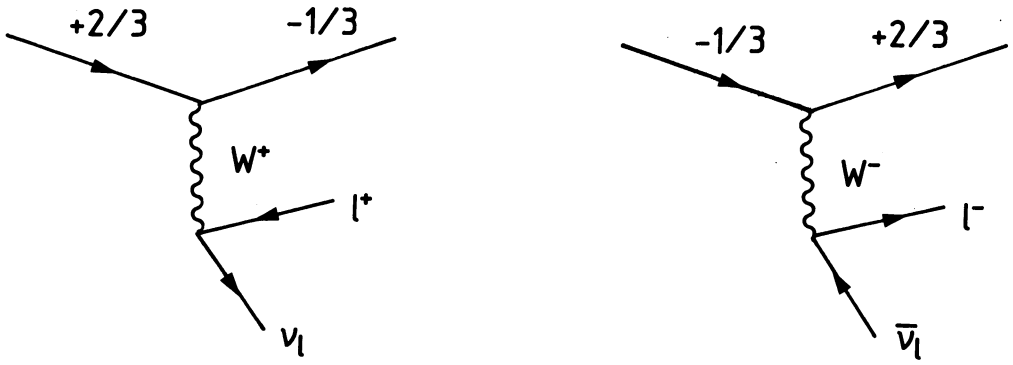

Figure 10: Decay of quarks with charge $+2/3$ and $-1/3$.

in which L = left-handed, R = right-handed.
If q, l and ν_l were massless, their energy spectrum would be given by [21]

$$dN_{q,l,\nu}/dx = 6x^2[(2-4\rho/3)-(2-16\rho/9)x] \tag{60}$$

were $x = p/p_{max} = 2p/m_Q$ and ρ is the Michel-parameter which has a value between 0 and 1.
The left-handed and right-handed particles in (59) have a different ρ parameter: to have $x = 1$ in 3-body decay a particle should be emitted in opposite direction of the two others. This is not possible for the right-handed particles in (59) (see fig.11) and as a result $\rho = 0$. For the left-handed particles in (59) this is only possible if they are emitted in opposite direction of the Q-spin (see fig.11), in this case $\rho = 3/4$.

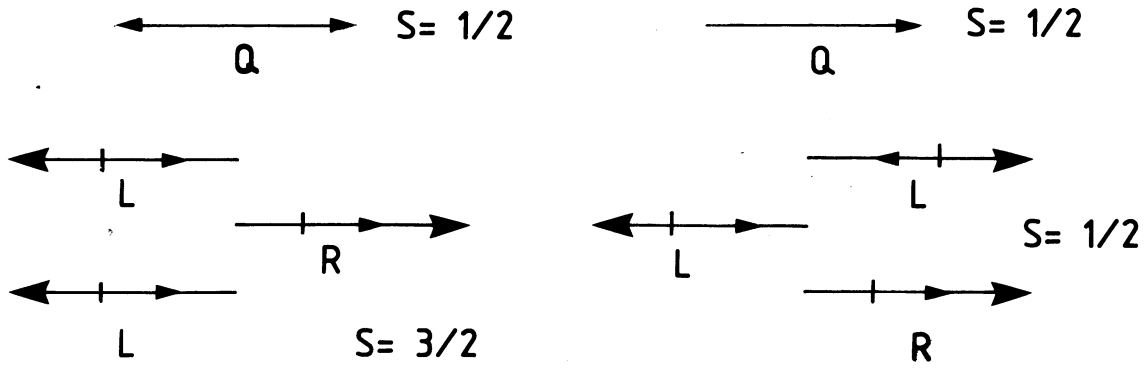

Figure 11: Decay of quarks with charge $+2/3$ and $-1/3$.

In fig.12 the Michel spectra for $\rho = 0$ and $\rho = 3/4$ are shown. Thus in charm-decay one has for l $\rho = 0$ and for ν $\rho = 3/4$, in bottom-decay the reverse.
This is similar to muon decay: $\mu^- \rightarrow e^- \bar{\nu}_e \nu_\mu$, in which $\bar{\nu}_e$ has $\rho = 0$ and e^-, ν_μ $\rho = 3/4$. The spectra of (60) have to be corrected for:

1. The finite mass of q in (59). In case of $c \rightarrow sl\nu$ one has $m_c \approx 1.2$ GeV/c^2 and $m_s \approx 0.3$ GeV/c^2. The mass of l can be neglected in case of e and μ.

2. QCD corrections for virtual gluons and gluon bremsstrahlung

3. Fermi motion of decaying quark and spectator inside meson.

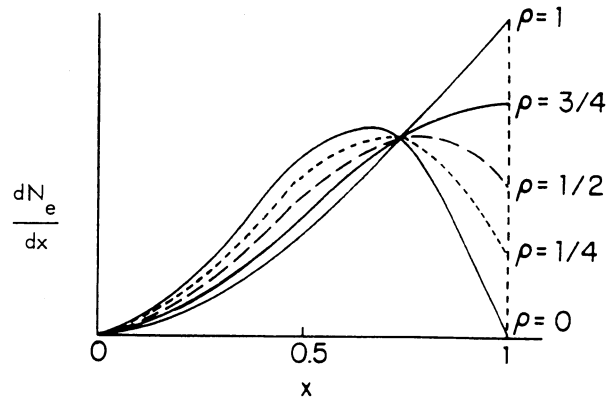

Figure 12: Michel spectra for different values of ρ.

Altarelli et al. [84] have suggested a model which takes into account these corrections in case of charm and bottom decay. For $D^{\pm}$-decay they have fitted the charged lepton spectrum obtained from the model to experimental data with as free parameters the mass of the s-quark, the mass of the spectator $\bar{d}$-quark and the Fermi momentum given to the spectator quark. The data used came from the DELCO-collaboration [78] which measured $e^+e^- \to \Psi''' \to D^+D^- \to e^{\pm} + (>2$ charged particles) and is shown in fig.13 together with the fit.

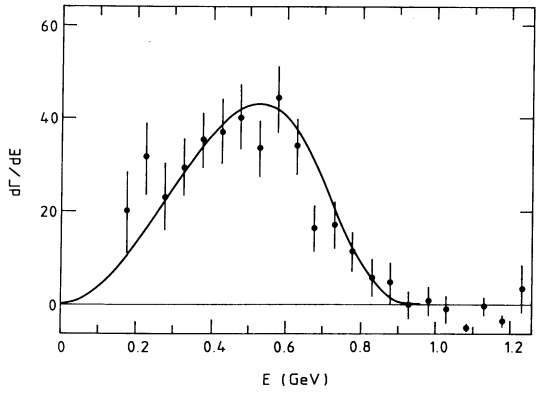

Figure 13: Electron spectrum in rest frame of D in case of semi-leptonic decay from [78]. The curve shows the fit of the spectator-model [84].

This fit gave a very small value for the Fermi motion and is compatible with no Fermi-motion.
Thus tuned, the model gave a neutrino spectrum that could be parametrized like: $1/\Gamma_{tot}\partial\Gamma/\partial x = 21.24\ x^{2.3}(1-1.13x)$ for $0<x<0.885$ and $=0$ for $0.885<x<1$, where $x=2E_\nu/M_D$, with a mean x-value of 0.551 and maximum at $x=0.617$.
The prediction of this model for the spectrum of the charged lepton in the case of bottom decay ($\approx$neutrino spectrum in charm decay) is in agreement with data from ARGUS [22]

3. EXPERIMENTAL LAYOUT

3.1 THE PROTON BEAM

A 400 GeV proton beam was supplied by the CERN Super Proton Synchrotron (SPS), with a one-turn, 23 μsec long extraction and repetition rate of 12 sec. The maximal intensity was ca. 1.3 10^{13} particles/pulse (see table 3). The dumps were placed at the downstream end of the 290 m long decay tunnel, used for wide-band and narrow-band neutrino beams. In fig.14 the layout of the beam, target, shield and detector is given.

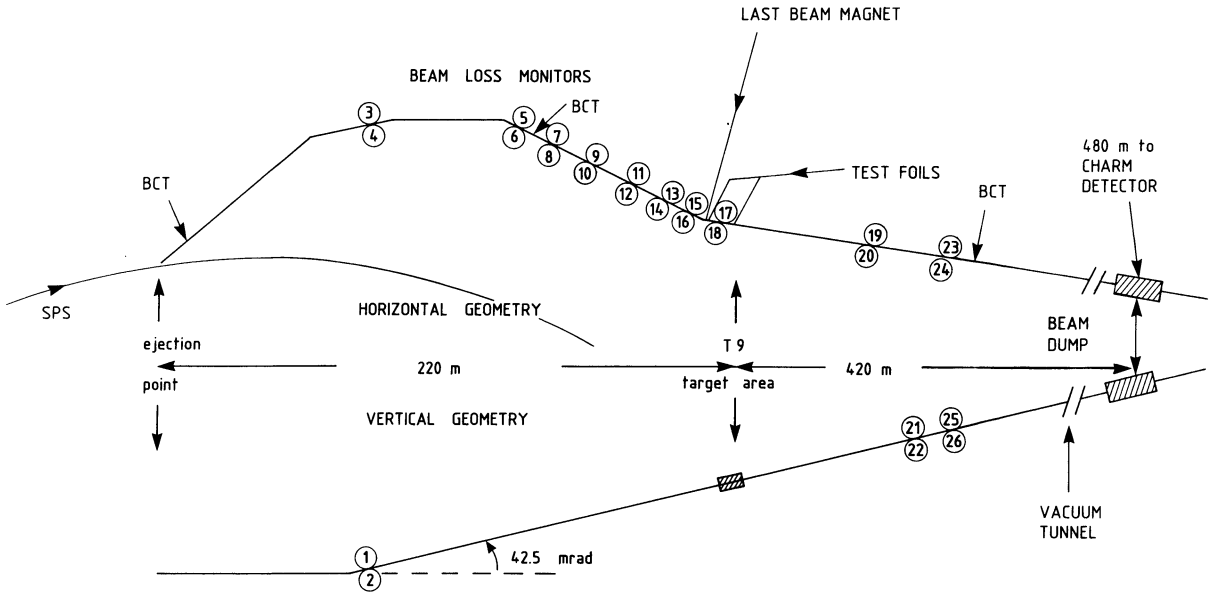

Figure 14: Situation of the targets, beam current transformers (BCT) and beam loss monitors (numbers in circle). Also the position of the calibration foils for the loss monitors is indicated. The counters in the horizontal (vertical) geometry measure the losses in the horizontal (vertical) plane.

The beam steering was carried out with dipole and quadrupole magnets. All magnets after the slow neutrino split (downstream of the second BCT in fig.14) were powered continuously, which assured stable beam conditions. The beam intensity was measured with three beam current transformers (BCT), the most downstream one was placed close to the last magnet (see fig.14). To control the steering, equipment to visualize its position could be moved into the beam. During data taking the beam position was monitored with a secondary emission (SEM)-grid 45 cm upstream of the target (see appendix C and F). Since the last bending magnet had a distance of 420 m from the target, a shift of 1 cm measured on the SEM-grid corresponded to a shift of only 2.2 cm of the beam axis at the detector. The resolution of the SEM-grid was better than 0.5 cm.

Great care has been taken to avoid any contact (scraping) of the beam with its environment such as vacuum pipe, magnets etc., by making all apertures as big as possible. The secondaries created by scraping have on average a very long free decay path, so they would cause a large background of neutrinos and muons, which would be hard to control. During normal operation the beam ran through vacuum, except for the exit window of the vacuum pipe (100μm Ti) at a distance of 1m from the target and the SEM-grid.
In order to detect beam scraping, 26 loss monitors were mounted pair-wise around the beam line, left and right and above and below the vacuum pipe at strategical places (see fig.14). These loss monitors, whose signals were recorded continuously during data taking, consisted of ionization chambers sensitive to an eventual beam halo and were calibrated with aluminum foils of different thickness, which could be moved into the beam at about 440 m upstream of the dump. Foils of 7.1 μm, 14.1 μm and 80.6 μm thickness were available, which induced inelastic interactions with probabilities of 1.8 10^{-5}, 3.6 10^{-5} and 20.5 10^{-5} per proton respectively. Relating the results of this calibration to the observed rate of neutrino interactions from normal neutrino beam operation

Table 3: Main parameters of the experimental set-up.

proton beam:	Energy:	400 GeV
	spill time:	23 μsec
	repetition cycle:	12 sec
	typical intensity:	1.3 10^{13} ppp
dump target:	dimension:	41.5 x 31 x 302.5 cm^3
	density $\rho = 1$:	solid copper 8.96 g/cm^3
	density $\rho = {}^1/_2$:	laminated, 2.5 cm copper 2.5 cm Air over $^2/_3$ of the total length
	density $\rho = {}^1/_3$:	laminated, 2.5 cm copper 5.0 cm Air over the total length
distance:	upstream end of target- - centre of fiducial volume:	487.3 m
fiducial volume:	Mass:	90.6 tons
	cross-section:	2.4 x 2.4 m^2
	solid angle:	24.3 μsr
	average density:	1.38 g/cm^3
number of protons on target: (deadtime corrected)	density $\rho = 1$:	$(13.26 \pm 0.13) \times 10^{17}$
	density $\rho = {}^1/_3$:	$(6.35 \pm 0.07) \times 10^{17}$

with a target at the same location the estimation was made that a 10 μm Al foil produced a neutrino flux in the detector corresponding to 1 % of the expected prompt flux, derived from [4].

3.2 THE BEAM DUMP TARGETS

Targets of three different densities were used (see fig.15).

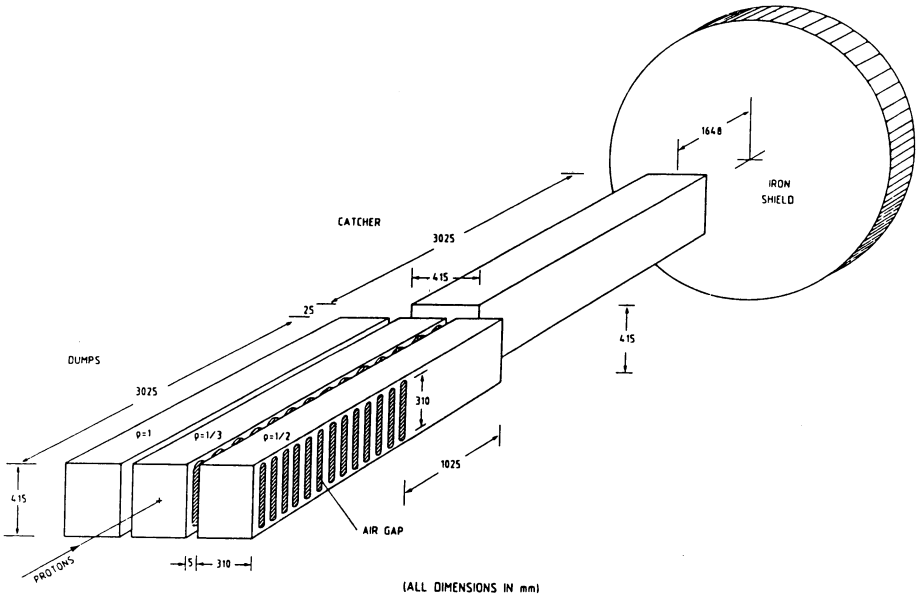

Figure 15: Target arrangement.

The most dense target consisted of a solid copper block, with size 302.5 x 41.5 x 31.0 cm, i.e. 20 proton interaction lengths long, which will be called density one ($\rho = 1$) target. A target which had one third of the density of the first one was made by taking a block of copper with the same dimensions as the $\rho = 1$ target and milling 40 slots of 5 cm in the copper (see fig.15). The remaining amount of copper was 1 m = 6.7 proton interaction lengths. It will be called density one third ($\rho = 1/3$) target in the following. These two targets were used to take the neutrino data.

A third target with density one half was used in a few runs to check the extrapolation method on the muon flux. It was constructed in the same way as the $\rho = 1/3$ target by milling 20 slots of 5 cm over a length of 2 m only. So the $\rho = 1/2$ part had in total 1 m of copper, like the $\rho = 1/3$ target. The assembly of $\rho = 1$, 1/3, 1/2 targets ($\rho = 1/3$ in the middle to minimize lateral leakage) could be shifted perpendicular to the beam direction. Sensors detected the target which was actually in place.
The targets were initially cooled with water. After problems with the water supply pipes which broke off due to shock waves caused by the beam impact, the $\rho = 1$ target was replaced by an air-cooled one. The $\rho = 1/3$ and $\rho = 1/2$ target remained the same. Behind the target a solid copper block, called "catcher", of 302.5 x 41.5 x 41.5 cm was installed to prevent the (permanent) iron shielding from becoming too radioactive. The catcher could be moved horizontally over its own width (41.5 cm), thus enlarging the air gap behind the target from 2.5 cm to 470 cm and making it possible to perform some tests of systematic effects (see appendix B).

3.3 MUON SHIELD AND MUON FLUX MONITORING

To prevent muons from reaching the neutrino detector, a shield was used, consisting of iron, concrete and earth (see fig.16 and table 35 of appendix B).

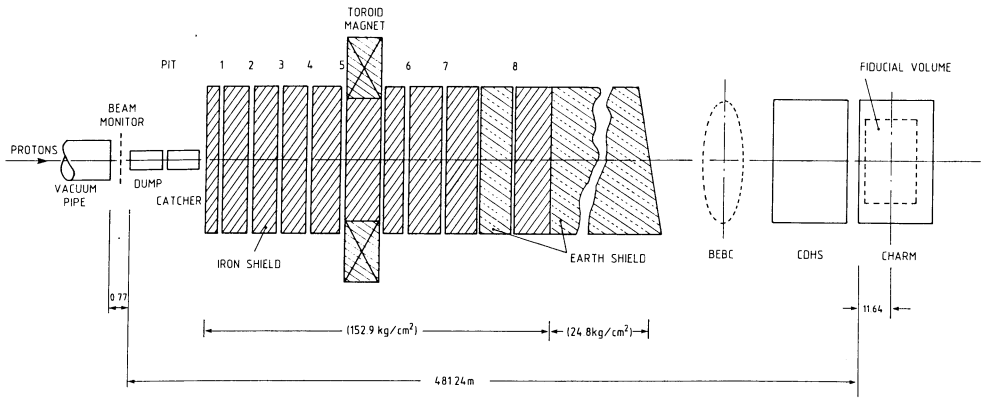

Figure 16: Target, muon shield and detector position.

Just behind the target the shield was made out of an array of cast-iron disks, one disk was 40 cm thick, had a diameter of 2.7 m and a density of 7.25 gr/cm^3. At several distances in this array gaps were left free for equipment to measure the muon flux. These gaps were numbered from 1-8, gap 1 was the most upstream one. The amount of iron between the gaps is given in table 35 of appendix B. Between gap 5 and gap 6 a toroidal iron ($\rho = 7.8$ gr/cm^3) magnet was installed of 6 m diameter and 10 m length, in which the radial field was non-zero in an outer shell of 2 m thickness. This magnet served to spoil muons at the edge of the shield: bending back into the shield one sign and deflecting further away from beam axis the other sign.

Since neutrino flux and muon flux are strongly correlated and the charged muons are much easier to detect, the muon flux was used to monitor the neutrino flux. With the help of the muon flux one could check burst-by-burst the quality of the neutrino beam e.g. its steering, intensity etc. The muon flux was also used to check the density extrapolation method, the influence of temperature changes and shock waves and to estimate the leakage of the density 1/3 target (see appendix B). Since the energy – loss of muons in iron is well known [91], one can use the flux monitor system in the gaps as a (coarse) muon spectrometer. This has been done to normalize the Monte Carlo simulation of the conventional neutrino flux and to analyse the prompt muon flux.

The muon flux in the gaps of the μ-shield is monitored with the help of a large system of silicon detectors [23], also referred to as solid state detectors (SSD). Such a detector is a reverse-biased silicon diode in which traversing minimum-ionizing particles create electron-hole pairs in the depletion layer. Because of the electric field in the depletion layer the electron-hole pairs drift apart, resulting in a current. The charge delivered by the silicon detector is collected by a charge amplifier, which gives an output voltage proportional to the flux of charged particles through the detector. More details are given in [23] and appendix B.

3.4 THE NEUTRINO DETECTOR

The reaction products from neutrino interactions one can distinguish are hadrons, electrons and muons. Since the cross-section for neutrino interactions is very small (e.g. at 40 GeV $\approx$ 2 10^{12} times smaller than the proton cross-section) a detector for these particles must be massive. However most detection elements (in our case plastic scintillator, proportional drifttubes and streamer tubes) have low density. In order to keep the size of the detector within limits one can sandwich the detection elements between volumes of more heavy target material.

Most particles created in the initial neutrino interaction reinteract in the detector and start a cascade or shower. The energy of the cascade will be deposited in the target material; the detection elements between the target plates sample the amount of particles at regular distances in the cascade. A highly energetic electron will start an electromagnetic (e.m.) cascade, consisting of photons and electrons created by a succession of bremsstrahlung and pair-production.
A highly energetic hadron will create new hadrons forming a hadronic cascade, which in general will have a more irregular shape than an electromagnetic shower, because the amount of particles created is smaller. In addition the secondary particles can have a variety of rest masses and the average transverse momentum is higher than for the particles created in electromagnetic cascades.

Hadronic showers have an electromagnetic component due to π^0-production. The detector was optimized to have good angular resolution for hadronic showers. This means that the length of both shower types should be approximately the same, which is also an advantage if one wants to search for e.m. showers inside hadronic showers (see section 4.6.2). From Monte Carlo simulations it followed that one has to choose target material for which the absorption length for pions is about four times the radiation-length. The cheapest convenient material available with these properties was marble ($CaCO_3$), with nuclear interaction length λ_π = 95 g/cm^2 and radiation length X_0 = 33 g/cm^2. (Also aluminum with λ_π = 106.4 g cm^{-2} and X_0 = 24.01 g cm^{-2} could have been used, but would have been much more expensive.)

The energy resolution of a sampling target calorimeter depends in first approximation on how many particles of the shower are seen by the detection elements:

$$R \propto 1/\sqrt{N_{seen}} \propto 1/\sqrt{E_{shower}}$$

The number of detected particles is larger if the target plate thickness is smaller, thus the target plate thickness determines the energy resolution. The design criterium was to have an energy resolution of 10 GeV at 200 GeV shower energy. A Monte Carlo study showed that a plate thickness of 8 cm for marble would be sufficient. The detector had in total 78 such plates, as is shown in fig.17.

At the downstream end material of a higher density, iron, was chosen to fully range out all particles, i.e. to prevent energy from escaping the calorimeter undetected. This so called end-calorimeter consisted of 15 iron discs of 5 cm thickness and diameter of 370 cm.

Muons, produced e.g. in charged current muon neutrino interactions, were in most cases not absorbed, but left the detector at the end or side. To determine the momentum and charge sign of the muons the target calorimeter was equipped at the downstream end with a muon spectrometer of magnetized iron and was surrounded by a magnetized iron frame. The iron discs of the end-calorimeter were magnetized.
The curvature of muon tracks was measured with the drift time information of the proportional tubes (see section 3.4.3).

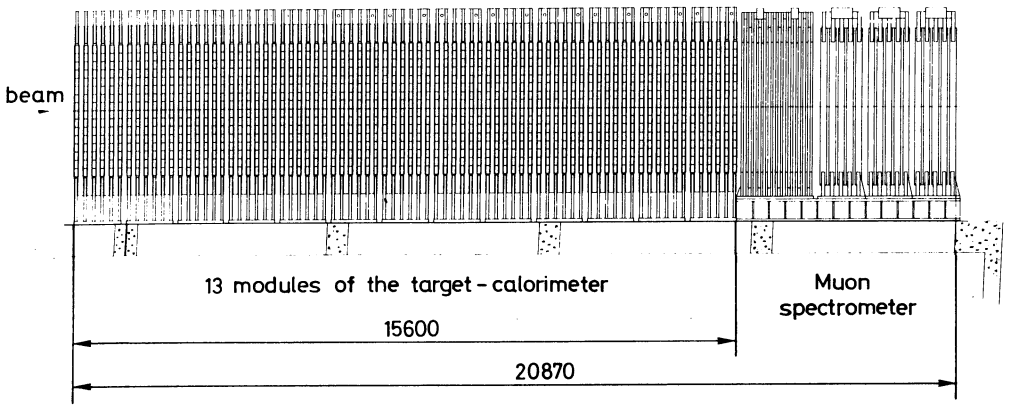

Figure 17: Side view of the neutrino detector.

The muon spectrometer consisted of 15 iron discs of 370 cm diameter and 15 cm thickness. The discs were mounted together in groups of 5 surrounded by a coil to produce the magnetic field. In order to pass the coil through, a central hole of 16.7 cm diameter had to be left free in each disk. End calorimeter and muon spectrometer are shown in fig.18.

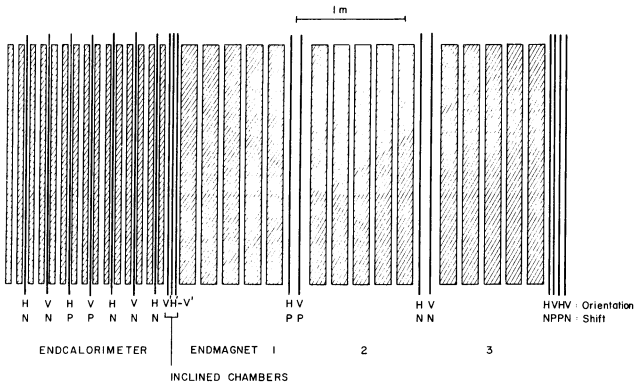

Figure 18: Endsystem with proportional drift tube planes. H = PDTs horizontal, V = PDTs Vertical. N, P indicates staggering, see text.

Each marble plate of 300 x 300 x 8 cm^3 was surrounded by an iron frame of 8 cm thickness and 45 cm width (see fig. 19). The windings of the coils were wrapped around the vertical sides of these frames.
All windings were made of copper tube through which cooling water was pumped. The direction of the magnetic fields could be changed to create focussing conditions for μ^+ or μ^-.
The magnetic field in the iron of frame and end-system was determined by measurement of the charge induced in small pick-up coils, wound around the legs of the frame and small holes in the discs of the end-system, during ramping up of the current. At the nominal magnetization current of 1 kA the field strength in the frame was 1.45 Tesla in the top and bottom legs and 1.54 Tesla in the lateral legs where the coils were situated. Measurements in three different frames gave the same result within ± 1%. At 0.5 kA the field was 15 % smaller.
In several discs of the end-system 20 pick-up coils were placed at five different radii and at four angles, differing by 22.5^0. The nominal current of 1 kA gave a field strength varying from 2.1 Tesla at 8 cm radius to 1.6 Tesla at 185 cm with an average value of 1.7 Tesla. Azimuthally the maximum deviation from uniformity was 2 %, the difference between central disc and outer disc was always less than 3 %. The field strength in the end-magnet and the end-calorimeter were the same within 2 %.

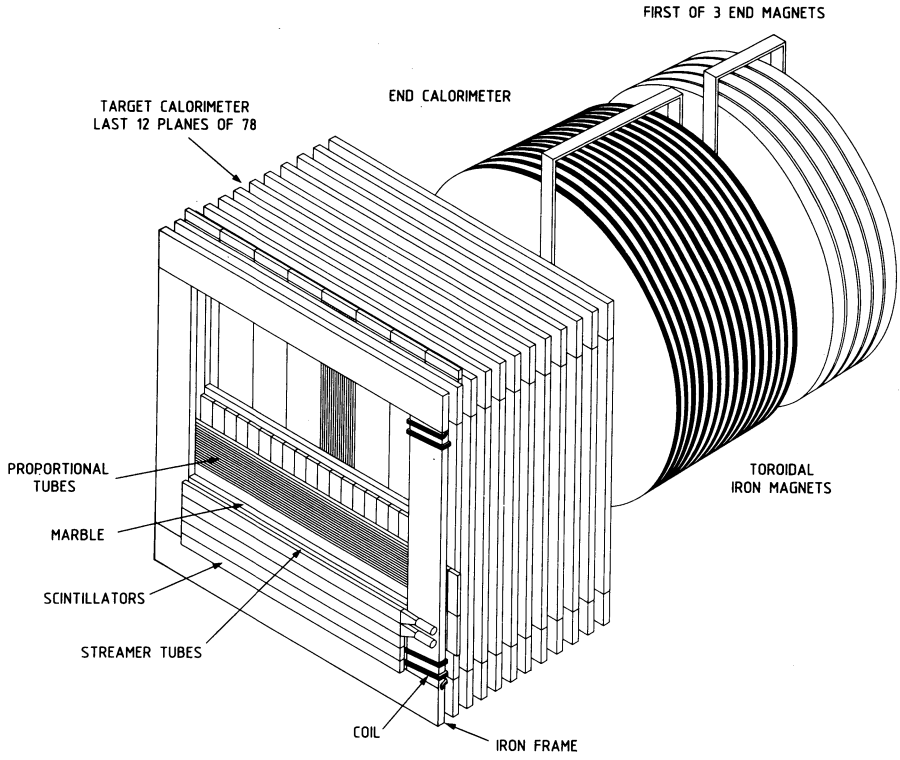

Figure 19: Layout of detector.

3.4.1 ACTIVE ELEMENTS

The CHARM detector had as active elements planes of scintillators, proportional drift tubes (PDT) and streamer tubes (ST), interspersed between the target plates.

The scintillator system was used as the main energy sampling device, because it had the best energy resolution. It also provided the signals for the trigger because it was faster than all the other elements. The scintillators only covered the marble plates of the target calorimeter. There were 78 scintillator planes, each plane consisted of 20 scintillators of 300 x 15 x 3 cm^3. In addition one plane with a surface of 4 x 4 m^2 was mounted in front of the first target plate to detect incoming charged particles ("veto-plane").

Proportional drift tubes (PDT) were used for precise determination of the position of single tracks, shower vertices and of the shower direction. They were mounted in planes of 128 tubes of 400 x 4 x 4 cm^3, 96 planes in total. The PDT-system was especially important for the determination of the muon momentum from the curvature of the muon track in the magnetic field of the frame and the end-magnet. At the places which were not covered by scintillators, i.e. the iron frame surrounding the marble plates, the end-calorimeter and end-magnet, the PDTs were the only devices to measure the energy deposition of particles.

Every scintillator plane was followed by a plane of streamer tubes of the same dimensions with an orientation perpendicular to that of the PDTs. One plane consisted of 256 tubes of 350 x 1 x 1 cm^3. The main purpose of the streamer tube system was to improve the precision of the shower vertex position determination.

Six planes of scintillation counters were inserted in the gaps of the end-magnets to measure the radiation loss by bremsstrahlung and pair-production of highly energetic muons passing through the iron. Each plane was composed of 18 scintillation counters, 9 on each side of the central hole for the coil (see Fig.20).

A general view of the detector is given in fig.17 and 19. During this experiment one module of six marble planes was used in a separate experiment to look for decay products of long-living, penetrating neutral particles. This module was placed beside the main neutrino detector [24]. Thus in this experiment only 71 marble planes were used. In the following sections the active elements will be described in more detail.

3.4.2 THE SCINTILLATOR SYSTEM

The scintillator system was designed to be able to register single minimum-ionizing particles (MIP) as well as showers up to 200 GeV and to be linear within 1 % over its full range. The first requirement was necessary to be able to use cosmic rays for calibration and monitoring. As scintillating material NE 114 (polyvinyl toluene + doping) from Nuclear Enterprises was used in the form of polished bars of 300 x 15 x 3 cm^3. Twenty bars were put together to form a plane of 300 x 300 cm^2. The detector had in total 78 such planes (see fig.17) interspersed between the marble plates, in total 21 tons of scintillator material. The orientation of the bars alternated between horizontal and vertical position in neighbouring planes. A bar had on one end a plane mirror and was viewed from the other end, through a 50 cm long triangular light guide, by a 2", 12 stage photomultiplier (PM), EMI 9839A, with a quantum efficiency > 15 % for blue light. The PMs were pressed against the light guide by a spring. No optical grease was used. To protect against magnetic fields the PMs were surrounded by a mu-metal shield. A minimum-ionizing particle traversing at the middle of the scintillator gave about 56 photo electrons and about 46 if traversing at the mirror end. A correction was made for the light attenuation along the scintillator (see 3.4.8.). The gain of the PMs (ca $2 \cdot 10^6$) was adjusted to equalize the response of the different channels to within ±20%. A MIP gave a signal of about 7.5 pC and 15 ns length, or ca 40mV on a 50 Ω resistor. The scintillator response was calibrated and monitored with the help of cosmic rays (see 3.4.8.).

High-energy muons may lose a considerable amount of their energy by bremsstrahlung when passing through iron. Six planes of scintillation counters were inserted in the gaps of the end-magnets (see fig.18) to detect and measure this energy loss. Each plane consisted of 18 scintillators, mounted as shown in fig.20.

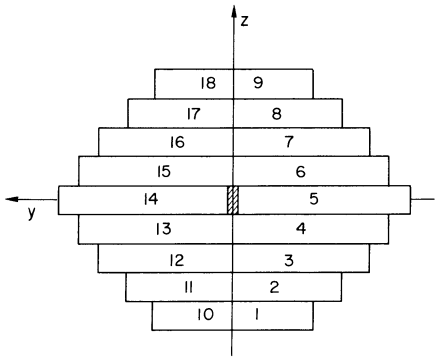

Figure 20: Bremsstrahlung counters of end-magnets.

The time difference between the signal from the bremsstrahlung counters and the last scintillation counter planes of the calorimeter was measured and recorded in order to detect cosmic ray muons entering the muon spectrometer from the back. These last events could fake quasi-elastic charged current muon neutrino interactions.

A special scintillator plane was mounted in front of the detector to veto incoming charged particles. To increase its efficiency the veto plane was constructed of two layers of scintillator bars, 40 bars in total. The two layers were shifted by half a scintillator width to avoid leaks.

For reasons of economy the scintillator signals were transported by simple twisted-pair cables. Ten twisted-pairs were grouped in one cable, which was surrounded by a copper shield. A twisted-pair had a specific

impedance of 100 Ω, a risetime of 15 ns and a crosstalk of charge between any two pairs $< 10^{-4}$ after 30 m of transmission.
In order to drive the twisted-pair cable with a balanced signal the circuit of fig.21 was used: the anode and last dynode give (almost) the same signal, but with opposite sign. In this way a high rejection for common mode noise was achieved.

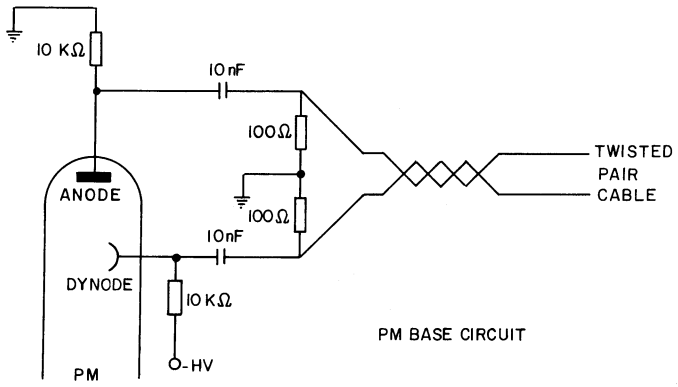

Figure 21: Photomultiplier circuit with balanced signals.

From each PM (1560 channels in total) the signal was guided to a signal "splitter", where it was duplicated via a high impedance input balanced amplifier and sent to a system of strobed discriminators (one per channel, see 3.4.5.), which prepared the trigger decision. From the splitter the signal continued to the ADCs. The cable lengths between PMs and splitter were adjusted to ensure that signals from a relativistic particle travelling through the centre of the calorimeter in the direction of the neutrino beam coincided at the splitter to within 2 ns. The maximum cable length was about 30 m, the minimum cable length about 12 m. Between the splitter and the ADCs a twisted-pair cable of 80 m was used for each channel in order to create the delay required for the trigger logic to generate gating pulses for the ADCs in time with the arrival of the signals to be analyzed.
Isolating 1:1 transformers were used to adapt the balanced signal of the twisted-pair cable to the single ended 100 Ω input of the ADCs. Per scintillator channel two 8 bits ADCs were used, 95% of the signal went to one ADC (high sensitive ADC), 5% to the other ADC (low sensitive ADC). In this way a dynamic range equivalent to 5000 channels was achieved. The ADCs were based on LeCroy QT 100 D charge-to-time convertors and had a sensitivity of 0.25 pC/channel and a maximum conversion time < 12 μs. The pedestals were adjusted to be in channel 4 to 8. The maximum pulse height of 5000 channels was reached if 150 minimum-ionizing particles would simultaneously traverse one single scintillator. The probability of such an event is about 1% for a 200 GeV shower. The ADC modules had a buffer memory to store 50 events.

3.4.3 THE PROPORTIONAL DRIFT TUBE (PDT) SYSTEM

A proportional drift tube consists of a conductive tube filled with gas and an anode wire at the centre (see fig.22), on which a high voltage is applied.
A charged particle traversing the tube ionizes the gas along its track. Electrons and positive ions drift apart due to the electric field and induce a signal on the wire. The charge is collected by a charge amplifier, which gives an output voltage proportional to the collected charge.
If the applied voltage over the tube is high enough the drifting electrons ionize new gas molecules, so the initial charge gets amplified. Since this (gas) amplification only occurs very close to the wire, where the (radial) field is strongest, the output signal is still proportional to the initial charge caused by the traversing particle and independent of the drift distance.
If the high voltage is increased further, every local ionization in the gas would induce a cloud of ionized gas along the full length of the anode wire: the tube becomes conductive until the high voltage drops below a certain value. This mode of operation is called the Geiger mode. Because of the long time it takes before the tube is able to detect a next particle this mode was not useful for this experiment.

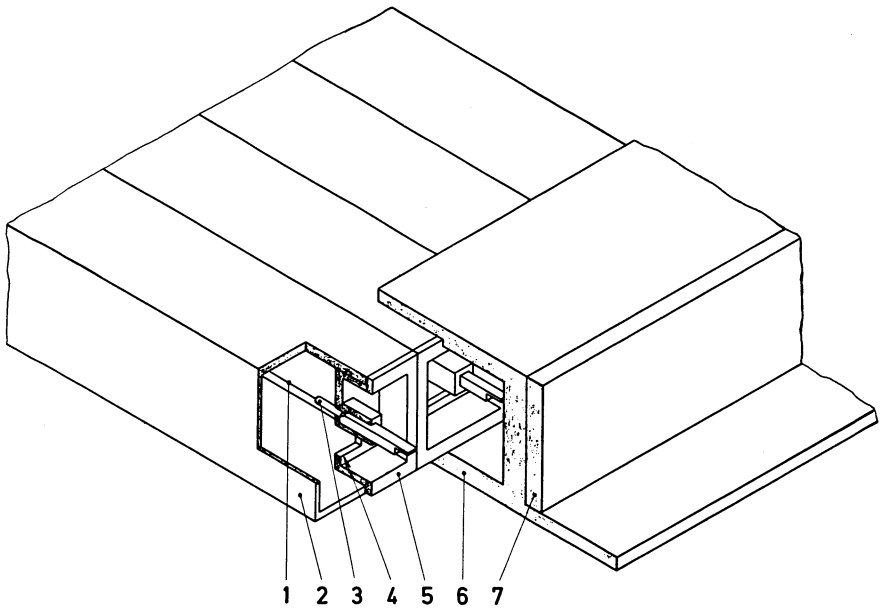

Figure 22: Details of the mechanical design of the proportional drift tubes. (1) sense wire; (2) aluminum tube; (3) wire support; (4) gas inlet/outlet; (5) insulator; (6) tube support and manifold, aluminum; (7) cover plate.

The drift speed of the electrons is of the order of a few cm/μs and almost constant over a large electric field range. By measuring the time delay between the crossing of the particle (given by the scintillator signal) and the arrival of the charge on the wire, one can determine the distance at which the particle crossed the anode wire.

In this experiment square tubes of internal cross-section 2.9 x 2.9 cm^2 and length 400 cm were used. Sixteen such tubes were glued together to form a chamber, of which 8 were mounted in one plane of 400 x 400 cm^2 and 93% active surface. The detector had 96 PDT-planes: 78 in the target calorimeter, 7 in the end-calorimeter, 8 in the end-magnet and 3 inclined planes between the end-calorimeter and the end magnet (see fig.17, 18). The inclined planes, rotated clockwise around the direction of the neutrino beam at angles of -12.5^0, 12.5^0 and -12.5^0 respectively, were used to solve ambiguities between the horizontal and vertical projection in events which had more than one track.
The orientation of the wires was horizontal or vertical (except for the 3 inclined planes) and alternated every other plane. In the target calorimeter the wires were perpendicular to the orientation of the scintillators in the same gap between the marble plates. Every third and fourth plane of each projection was shifted laterally by one-half the wire distance to solve the left-right ambiguity of the drift time for tracks and to avoid large inefficiencies along tracks.

A gas mixture of 95 % argon and 5 % propane was used under 30 mbar overpressure. The propane is a so-called quenching gas which absorbs ultraviolet radiation and it was added to allow for a high gas gain without having the tube working in the Geiger mode. A high voltage of 1.5 kV was used, giving an average drift velocity of 3.56 cm/μs. An average space resolution of 1.3 mm could be achieved. The gas amplification was 7.5 x 10^4, a minimum-ionizing particle, crossing the tube perpendicular to the anode wire gave a charge of about 4.3 pC. The gas was circulated by pumps and slowly refreshed at a rate of one volume per week.
It was found experimentally [25] that adding a small amount of water vapour (5 vol.%) to the gas prevented the deposition, after long usage, of an insulating layer on the wires.

PDT-ELECTRONICS

Measurement of charge and drift time was organized per chamber of 16 wires (8 per plane). The electronic channels of the 16 tubes were mounted on two printed circuit cards: one contained the analog circuits ("analog card"), the other one contained scalers and memories required for storing the information of one event for each channel and the necessary drivers and logic ("logic card"). The cards were put on top of each other and mounted on the chamber by a 50-way printed circuit board connector. Sixteen chambers, forming two planes, were read out in series by a single CAMAC readout module. There were 48 read-out modules working in parallel. Data was transferred into a buffer memory, allowing 256 charge and time measurements (from any 256 tubes) to be stored, or, for showers of average size, 20 to 40 events equally distributed over the detector.

The block diagram of the PDT front-end electronics is given in fig.23. and the timing of some important signals is shown in fig.24.

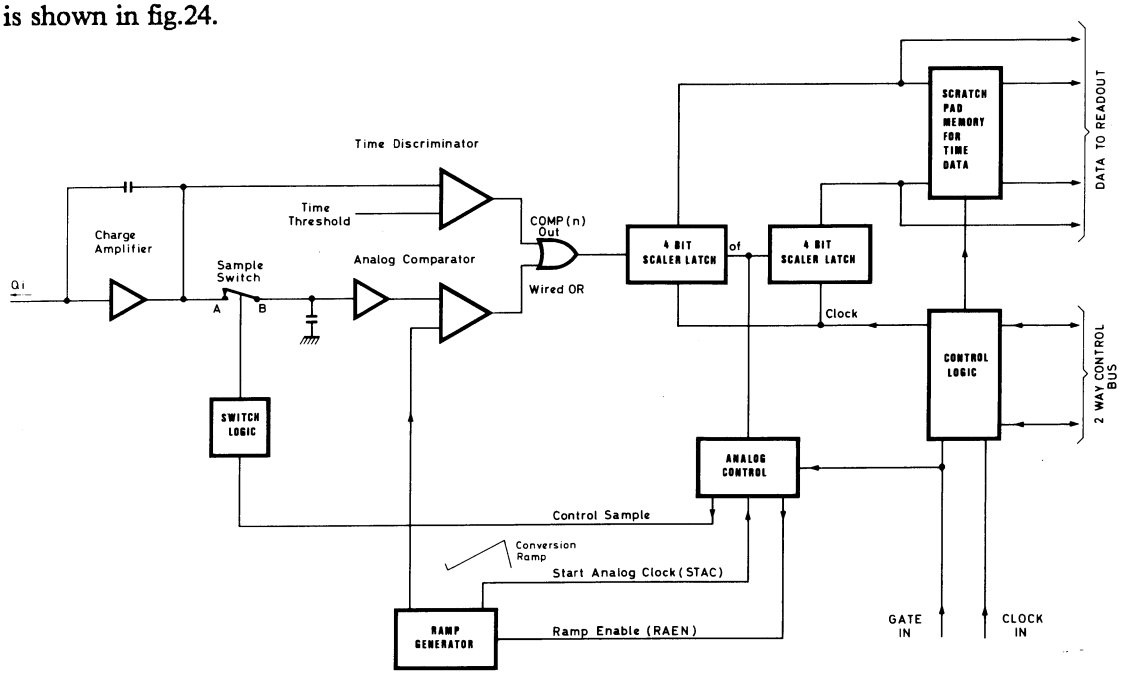

Figure 23: Electronic principle of PDT-readout. For explanation see text.

Via a high voltage separation capacitor the signal of the wire was fed into an operational amplifier configured as a charge amplifier, converting an input charge Q into a voltage $V = Q/C_f$, where C_f is the feed back capacitance (actually a more complicated feed back circuit was used, see next section).
The output signal of the input amplifier was split into two ways: the first leg (fast) was used to generate the time information, the second leg (slow) generated the charge amplitude information. The timing discriminator gave the signal COMP as soon as the input amplifier signal exceeded the threshold of 12 mV. COMP was used to start the scaler latch on the logic card (2x4 bits per channel) counting 20 MHz clock pulses. After the first 4 bits gave an overflow (= 800 ns after the crossing of the threshold) one of two things could happen (see timing diagram):

1. No GATE-signal arrived within 800 ns. The counting was terminated, the scaler reset and the analog signal was not stored.

2. There was a GATE-signal within 800ns : the trigger logic had decided that the event should be stored. The sample (MOS) switch opened and the output level of the input amplifier was stored on capacitor C_s. Since the rise time was approximately 800 ns the stored level was close to the maximum of the signal.

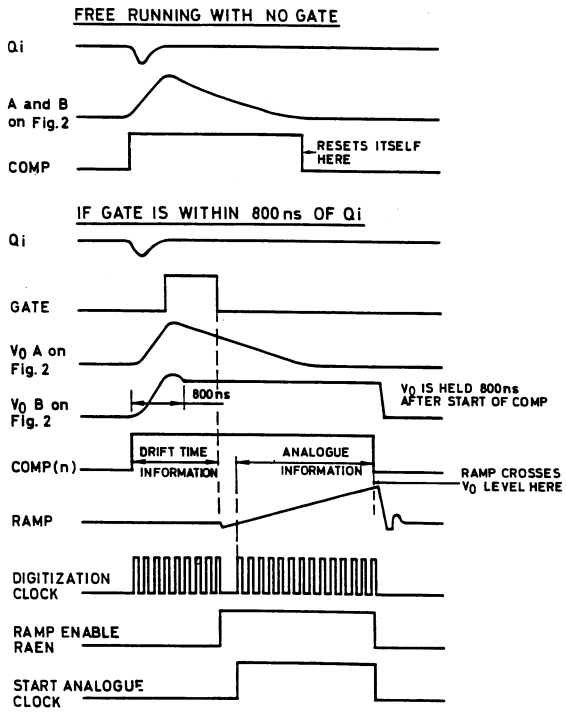

Figure 24: Waveforms of PDT-electronics. For explanation see text.

At the falling edge of GATE, which was the late time reference for the drift time measurement (the start of GATE was a fixed time after the scintillator strobe and also its length was fixed) the drift time contents of the scalers was transferred to their latches and from there to the scratch-pad memory. The scalers were reset. Also at the trailing edge of GATE the ramp generator was started and would produce a voltage rising linearly with time. When the voltage of the ramp generator crossed a certain lower level the scalers started counting clock pulses. This continued untill the ramp voltage equaled the on C_s stored analog signal and the analog comparator stopped the scalers, whose contents after the longest conversion were transferred to their latches. So the pulse height of a certain channel = (scaler content) x (clock frequency)$^{-1}$ x (Volt/time of ramp generator). At that moment the drift time information was stored in the scratch pad memory and the pulse height in the latches of the scalers, the card was ready for readout.

After the last pulse height conversion of the 256 channels connected to one read-out module had ended, the data were transferred to the memory of that module. Channels without data were not stored.

When a GATE-signal was given, the minimum dead-time of the system was the length of GATE (= 1 μs) plus the time necessary to transfer the time information to the scratch-pad memory = 3.2 μs, in total 4.2 μs. The maximum dead-time occurred, when a channel had to convert the maximum pulse height, which took 12.7 μs and together with the length of GATE the dead-time became 13.7 μs. (occasionally a much higher dead-time could occur, as for instance all channels on a double plane had data, caused by a cosmic shower. In this case the data transfer to the read-out module, at a rate of 2 MHz, took 256 μs. The next event could still be taken, the pulse height stored on the storage capacitor (C_s in fig.23) and the time on the scalers, but the read-out had to be finished before the card could accept another event. These cases occurred very rarely.

THE FEED BACK CIRCUIT OF THE INPUT AMPLIFIER

For the precise determination of the position of a muon track the charge gain of the input amplifier must be sufficiently high to give a clean signal for a traversing minimum-ionizing particle (MIP). On the other hand one

wants also a high dynamic range to determine the lateral shape of highly energetic electromagnetic showers, with a high amount of MIPS/cm^2. This last requirement is especially important for direct recognition of electromagnetic showers inside hadronic showers (see section 4.6.2).
For this reason a feed back circuit as shown in fig.25 was used for the input amplifier.

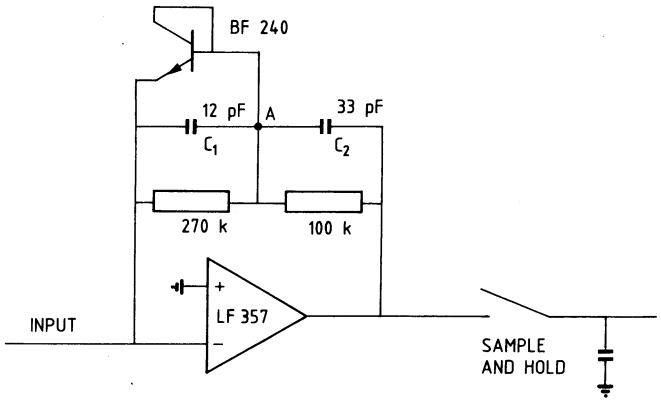

Figure 25: Feed-back circuit of input amplifier.

At low output voltages the silicon diode is non-conductive. The charge gain is:

$$A = (C_1 + C_2)/(C_1 \cdot C_2) = 114\ \text{mV/pC}$$

When the voltage at point A reaches $\approx$ 0.6 V the diode will conduct and C_1 is bypassed. The charge gain becomes:

$$A = 1/C_2 = 30\ \text{mV/pC}$$

Thus from input charge 0 to 0.6 x C_1 = 7.2 pC (= 1.7 MIP) the gain was 114 mV/pC and above that 30 mV/pC (see fig.26). The resistors are chosen such that for both states the time constant is 3.3 μs. As diode a transistor (BF240) with base and collector connected was used which was found in practice to gave the fastest switching between the two states.

TESTING OF PDT-ELECTRONICS

In order to test the more than 800 analog electronic cards a test set-up was built. With the help of a pulse generator and a CAMAC-controlled attenuator the full input pulse range could be scanned. The card to be tested was connected to a read-out module of the same type used in the detector. After every input pulse a GATE-signal was generated within 800 ns by a timing circuit. The CAMAC-crate with read-out module, attenuator and output/input registers was controlled by a Hewlett Packard 21 MX mini-computer and later by a CAVIAR CAMAC-processor [26].
For every card a graph as shown in fig.26 was produced.
Tests were made for the value of the two charge gains, the position of the change-over point and the correct drift time. The reference values were entered by measuring a special card, the tolerances around these values were fixed. If a card passed the test, a sheet with the date, the card number and measured features was printed.
An example of such a test sheet is given in fig.27.
At 15 input charge points (see fig.26) the amplitude and drift time were measured 5 times. In the upper part of the test sheet one sees for each of the 16 channels the intercept with the x-axis (marked offst), the two slope values and the position of the bending point. Channel 17 is the mean of all 16 channels. The charge is given in pico Coulomb (pC), the amplitude and drift time in scaler counts. "Err n" means the maximum deviation from the straight line fit in the region between marker n and n + 1 (see fig.26). In the second part of the test sheet the maximum rms value for 5 measurements over the 15 values of input charge are given for amplitude and drift time. The last column gives the maximum deviation from the reference drift time at the marker positions.

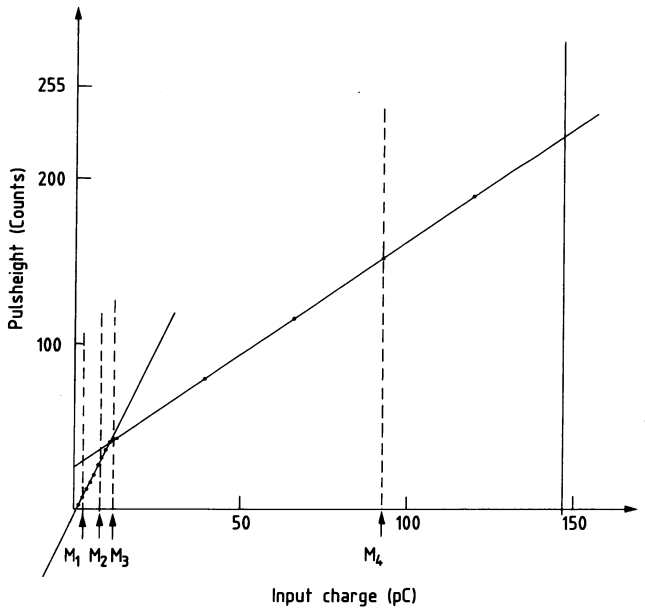

Figure 26: Characteristic of input amplifier.

Norms and tolerances are given at the bottom. If any channel deviated more than the allowed tolerance from the norm value an asterisk would be printed behind its value.
The failure rate was on average five cards per week, giving a MTBF/card of 26 x 10^3 hours.

3.4.4 THE STREAMER TUBE (ST) SYSTEM

Planes of streamer tubes were added after three years of operation of the detector to improve the angular resolution of showers [27]. These streamer tubes looked similar to the already used proportional drift tubes (see previous section). They have properties similar to Geiger tubes, but, due to a high amount of quenching gas (isobutane), the ionization is limited to a small region near the anode wire where the primary avalanche, caused by a drifting electron, took place. This way of operating is called the limited streamer mode [28]. As with a Geiger-Muller tube one only gets a yes/no signal, but the dead-time is much smaller ($\approx$ 300 μs) and the dead region is limited to $\approx$ 10 mm of wire at the place where the streamer occurred.
Other features of these tubes are: high output charge ($\approx$ 50 pC), gas composition and high voltage uncritical and because of the thick wires (50-100 μm diam.) they are robust.
In the CHARM detector tubes with 0.9 x 0.9 cm^2 inner cross-section and 267 cm length were used. Two extruded aluminum profiles of 8 tubes were glued together to form a chamber of 16 wires. Sixteen of these chambers formed one plane of 267 x 265 cm^2 with 86% active surface. The anode wire was made of stainless steel and had a diameter of 50 μm. The planes were centered on the beam axis with the wires perpendicular to the proportional drift tubes in the same plane (see fig.19). In total 77 planes were installed.
A gas mixture of 1/3 argon and 2/3 isobutane was used under an over pressure of 30 mbar. The total gas volume of 4500 l was circulated by pumps and refreshed at a rate of 3.2 l/min. The gas flow could be interrupted for more than one day without changing the performance of the system. A high voltage of 3.7 kV was applied.

READOUT ELECTRONICS

Sixteen channels were mounted on a daughter card to accept and buffer the signals from the wires of one chamber (see fig.28).
One channel consisted of an input discriminator, a latch and a FIFO-memory, which could store 40 events. The outputs from the comparator were latched by a signal derived from the scintillators. The output of the latches

CARDNR. 1214 DATE 82/03/23

WIRE	OFFST	SLOPE1	SLOPE2	YB	XB	ERR1	ERR2	ERR4
1	-4.9	4.19	1.33	38.15	10.27	-.38	-1.31	.21
2	-3.83	4.07	1.34	38.51	10.4	-.36	-.47	-.49
3	-3.23	4.14	1.35	39.96	10.45	-.28	-.71	-.98
4	-2.83	4.07	1.35	40.73	10.7	-.36	.92	-.59
5	-4.63	4.2	1.35	39.76	10.58	.25	-.95	1.01
6	-3.14	4.2	1.35	40.21	10.33	-.34	.31	-.78
7	-3.31	4.29	1.35	40.62	10.24	-.22	-.8	.49
8	-3.95	4.24	1.35	39.14	10.16	.19	-.44	1.33
9	-3.95	4.24	1.38	40.2	10.17	.19	-.49	.66
10	-2.83	4.07	1.35	40.57	10.66	-.36	.12	.68
11	-3.83	4.07	1.37	39.87	10.73	-.36	-.47	.35
12	-4.18	4.23	1.35	39.96	10.45	-.3	-.7	-.98
13	-3.83	4.23	1.35	39.27	10.2	.33	-.52	.86
14	-4.18	4.12	1.34	40.18	10.77	-.24	-.59	-.7
15	-2.83	4.07	1.33	40.31	10.59	-.36	-.47	1.39
16	-3.79	4.07	1.35	39.48	10.62	-.2	-.51	-.38
17	-3.64	4.16	1.35	39.8	10.45	-.17	-.74	.47

OFFST IN CTS
SLOPE IN CTS/PC; XB,YB=BENDINGPOINT IN PC,CTS
ERROR N=MAX. ERR.BETWEEN MARKER N AND N+1 (CTS)
WIRE 17=MEAN OF ALL WIRES

WIRE	MAX.SGM.AMPL.	MAX.SGM.TIME	MAX.TIME DEV. (CTS)
1	.98	.49	-.65
2	.98	.49	-.65
3	.89	.4	-.65
4	1.32	.49	-.65
5	1.02	.49	-.65
6	1.32	.4	-.65
7	.89	.49	-.65
8	.74	.49	-.65
9	.98	.49	-.65
10	.98	.49	-.65
11	.98	.49	-.65
12	.89	1111	-.65
13	.89	1111	-.65
14	1.33	.4	-.65
15	.49	1111	-.65
16	.98	.49	-.65
17	2.03	.49	

NORMS AND TOLERANCES

OFFSET: -4. +/- 1.5 CTS
SLOPE1: 4.21073+/- .4 CTS/PC
SLOPE2: 1.36287+/- .1 CTS/PC
YB: 40.8938+/- 5 CTS
XB: 10.4392+/- 1 PC
ERR,SGM.AMP,SGM.TIME,TIME DEV.(CTS): 10 5 1 1
SGM.MEAN AMP.,SGM.MEAN TIME(CTS): 10 2
MARKERPOS.(PC): 2.60943 7.79014 11.6559 92.5861
NS,M1(DB),N1,SN: 15 22 10 5
TMS AT MRKRPS(CTS): 16.2 17.175 17.5375 18.6625 18.7625
INPUTCHARGE= 146.739PC
1111=ABS(.1

Figure 27: PDT-test sheet, explanation in text.

were written into the FIFO-memory buffer 5 μs after the trigger, if no slow veto had occurred. A mother card grouped the data from 16 daughter cards. A grandmother card grouped the data from 12 mother cards and finally the CAMAC read-out box treated the outputs from 7 grandmother cards. At the end of the accelerator burst, the FIFOs were read in parallel. Their outputs were scanned by the readout box, suppressing zeros and loading the event buffer of this box with one event from the tubes. The event buffer could contain events up to 660 hits. Once an event was buffered, a CAMAC transfer could take place.

3.4.5 TRIGGER

The trigger decision logic used the scintillator signals because they were the fastest available. As described in (3.4.2.), the signal of every scintillator arrived, due to adjusted cable lengths, within ± 2 ns at a strobed discriminator, one for each channel.
These discriminators were part of a system called RMH (Receiver-Memory-Hybrid [29], based on parts designed for wire chambers), which contained logic for strobing, holding, resetting or reading the information of each

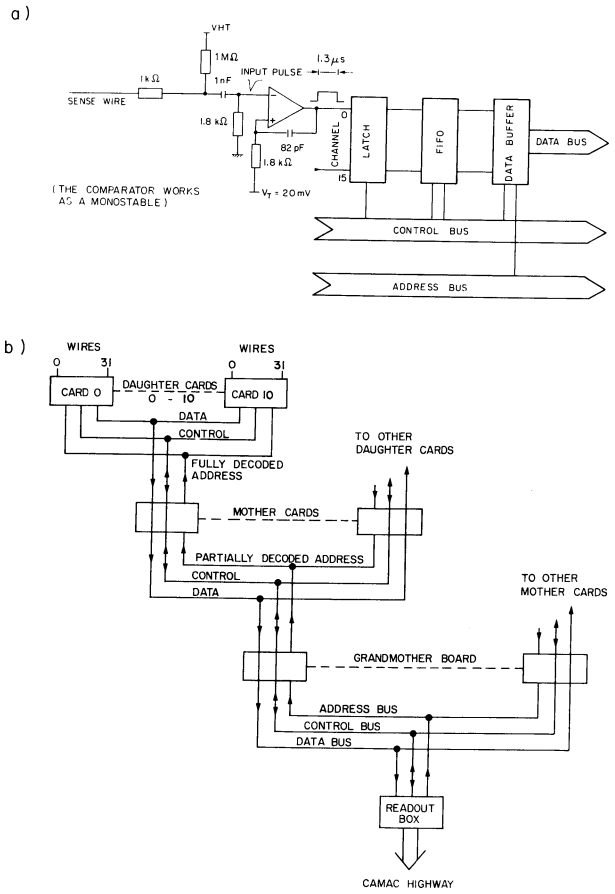

Figure 28: The streamer tube electronics. a) the logic of the daughter card. b) the read-out system. For explanation see text.

scintillator channel. The hold function was used to memorize the event pattern while a trigger decision was taken. If the event was accepted by that decision, the information was retained and read into a fast buffer memory, otherwise it was reset after 400 ns. The fast buffers were read out via CAMAC, together with all other event information. As strobe the H3-signal (see below) was used.
These signals were fed into a linear adder and if the sum of pulse heights of all scintillators was above a certain threshold, a discriminator generated the strobe signal. For each plane the RMH-modules produced 5 signals:

1. H: at least one scintillator above threshold
2. D: at least two scintillators above threshold
3. T: at least three scintillators above threshold
4. S: at least one of the side scintillators above threshold
5. E: energy deposition in the plane greater than a preselected value.

The H-signals of all planes were put into another majority logic, which could generate 4 signals designated by HM (M from 1 to 4), which were produced if at least M planes with a H-signal were present. The same was done for the other signals to generate DM, TM and SM. The H-signal of every 4th plane was put in a majority

logic to form a penetration signal, called PM, which meant, assuming (a) particle(s) traversing the detector, in at least $(M-1)\cdot 4+1$ planes at least one scintillator above threshold.
With these signals the trigger decision was made and timing signals formed to be sent to scintillator ADCs, proportional drift tubes and streamer tubes. The trigger system made use of CAMAC-controlled programmable logic units (PLU), which offered the possibility to set the trigger conditions by computer.

The trigger used was: strobe · H4 · vetobar · burst : the strobe (H3) gave the timing for analyzing the trigger variables; H4 means at least one scintillator above threshold in at least four planes; "vetobar" stands for no hit in the veto plane in front of the detector (= no incoming charged particle) and "burst" means that the burst gate had to be enabled. This gate was 33 μs long and centered around the accelerator burst of 23 μs duration. Some scalers were also recorded in a 10 ms wide gate around the spill to control the right timing of the burst gate (see appendix D).

3.4.6 DATA ACQUISITION

For the data acquisition (DAQ) a 16 bit NORD 100 from NORSK DATA CORPORATION was used, to control the CAMAC-system. CAMAC [30] (Computer Aided Measurement And Control) is a standardized system to link many small sub-units to a computer for data exchange. Examples of such sub-units used in this experiment are the scintillator ADCs (see 3.4.2.) and the PDT and streamer tube read-out boxes (see 3.4.3. and 3.4.4.). These sub-units have dimensions of 221.5 x 305 x 17.2 mm^3 and are placed side by side in a crate which has room for 26 of them.
They are connected by an 86-pin printed circuit board connector to the crate bus in the back plane of the crate. Two slots are occupied by the crate-controller, which has two lines to every sub-unit, one for slot selection and one for service request. The rest of the bus, e.g. address and data lines, are common to all slots. The crate delivers the power for all sub-units. The crate-controller is connected by a bus, the branch high-way, to a subunit, called branch controller, in the system crate. Up to 7 crates can be connected to a branch. The branch controller can address the crate controllers and takes care of data exchange. Several branch controllers can be put in the system crate, which is connected to the computer via a system crate controller. Bus-lines, bus-protocols, addressing scheme and function selection are all defined by the CAMAC standard.

The CAMAC-system used by this experiment had 7 branches:

1. four read-only branches for the scintillator ADCs (see 3.4.2.). In total 2 x 1560 ADCs.

2. one read-only branch for ADCs of the bremsstrahlung counters and analog plane sum (see 3.4.2.).

3. A branch for proportional drift tube and streamer tube read-out boxes. Four crates were used for the PDTs with 12 read-out boxes per crate, one read-out box per two planes (see 3.4.3.).

4. A branch for miscellaneous units.

A read-out cycle, controlled with timing signals from the SPS, looked as follows:

1. Accelerator burst, 23 μs long, repetition rate 12 s. Physics trigger 33 μs active, data accumulated in local memory of CAMAC-modules.

2. End of burst, interrupt to NORD 100 to start a read-out cycle. For every event the following were read: buffered scalers and pattern units for event count, trigger identification, etc.; scintillator ADCs; proportional drift tube pulse heights and drift times; bremsstrahlung counter ADCs; RMH fast buffer memory; streamer tube hits.
   The reading was performed with CAMAC block transfer in DMA mode. Some checks on the integrity of the data were made and error messages printed on a line-printer in case of faults. The ADC-information was reformatted by only keeping values of two counts above pedestal. For this purpose a pedestal file was kept in memory and continuously updated.
   The event was written to tape and send via a CAMAC-link to the monitor computer (see 3.4.7.).

3. After the last event was written to tape and also in the case of an empty burst the contents of several scalers was read and put on tape, e.g. dead-time counts, pulse trains of BCTs, SSDs etc. (see appendix D).

4. A request to the NFM link module was sent for beam information from the muon flux monitoring system (see section 3.3). The NFM-block was sent to tape and to the monitor computer.

5. Until the next burst, cosmic ray events (single tracks) and ADC pedestal events for calibration and monitoring were taken (see section 3.4.8.).

3.4.7 MONITORING

In order to check the proper functioning of the detector components a mini-computer, Hewlett Packard 21MXE, was used. This computer received data from the data acquisition computer via a CAMAC-link. Not all events were used for monitoring, the amount depended on computer occupation and link-speed and was usually 50% of the total number.
Checks were made on:

1. Scintillators: histograms of number of hits and mean pulse height of every channel could be displayed.

2. Proportional drift tubes: for every channel out of 12288 the number of hits, mean pulse height and mean drift time could be displayed. Cosmic-ray data was used.

3. Streamer tubes: the hit distribution of 19712 tubes could be displayed.

4. Scintillator ADCs: pedestals and the ratios of high-sensitive over low-sensitive ADC readings (see 3.4.2.) were monitored.

5. Trigger: a histogram of the frequency of every trigger type was available.

6. Beam information, histograms of:
   amount of protons on target from the BCTs
   the beam position from the SEM-grid in front of the target
   the signal from the beam-loss monitors
   the muon flux in the gaps of the iron shield as measured with the SSD-detectors.

The operator could select the display of data with the help of a touch-screen. The incoming events were stored on a disk buffer and could be displayed in graphical form (see fig.1 and 2).

In order to increase the amount of fast memory available per program running on the HP 21 MX, some special software was written to avoid system limitations (see appendix E).

An example of a display of the proportional drift tubes, made during a service period, is shown in fig.29. For the last plane of the target calorimeter, the seven planes of the end-calorimeter and two of the inclined planes (see fig.18) the number of hits (below), the mean pulse height (middle) and mean drift time (above) per wire are shown for cosmic ray interactions. The "dip" in the hit distribution for the end-calorimeter planes is due to chambers with a reduced length, necessary to let the magnet coil pass through the plane of PDTs.
One sees a hot wire in plane 83, and a clear timing problem in plane 82, caused by noise induced on the data bus. In plane 78 one sees a card (= 16 wires) with a mean drift time which is too low. Zooming in on this card would show 15 wires with a too low, and one with a correct drift time. This last one was a channel with a mal-functioning scaler-latch (see section 3.4.3). In this way on-line diagnostics to check the functioning of the electronics was possible.

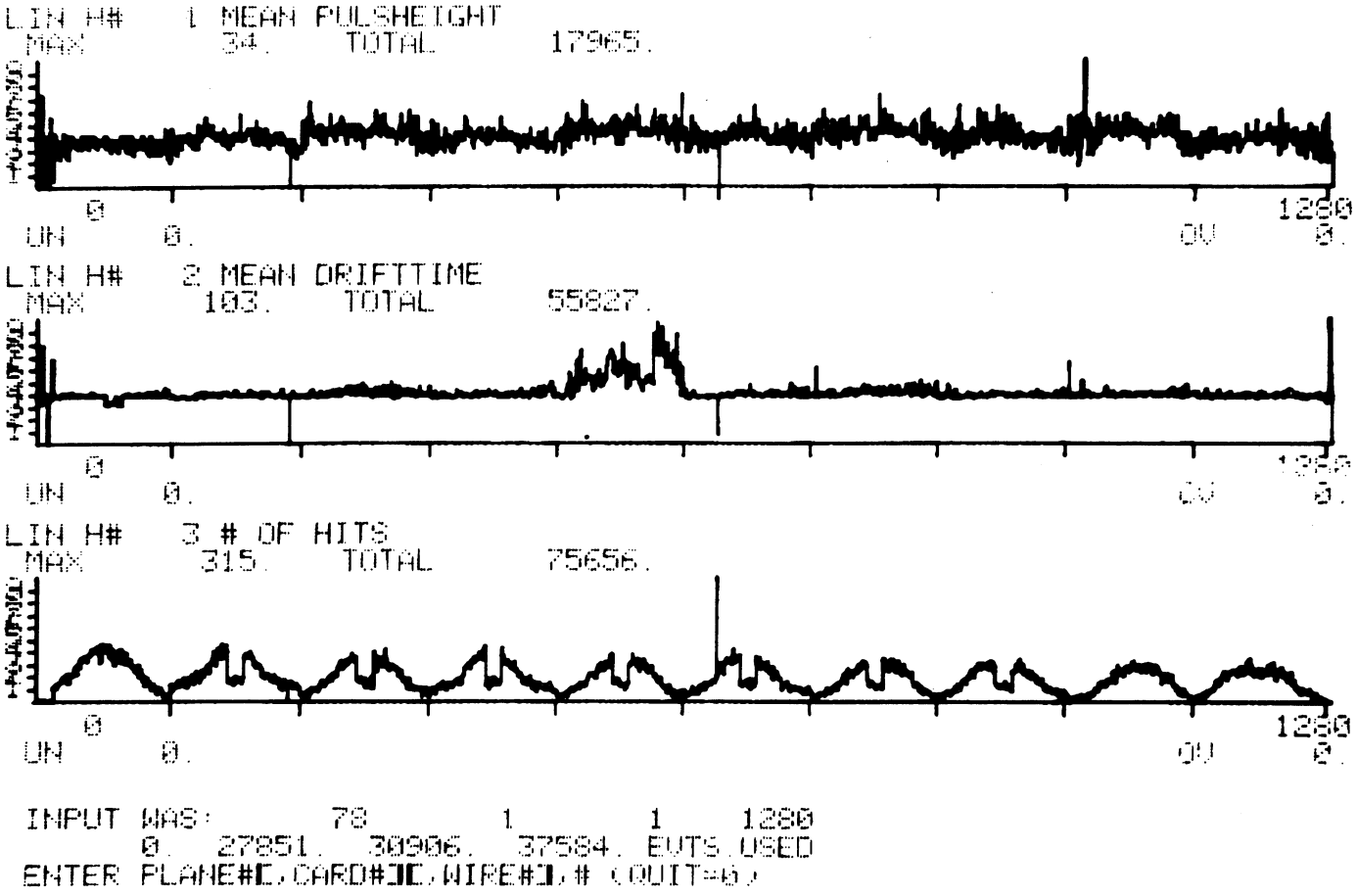

Figure 29: Example of on-line display from the monitor computer: check of proportional drift tube system. Starting from plane 78, ten planes = 1280 wires are displayed. For more details see text.

3.4.8 CALIBRATION

The energy calibration [70] of the detector was carried out in 3 stages:

1. Before every run period a large amount (> 400.000 tracks) of cosmic ray data was taken to determine the attenuation length of the scintillators. The mean pulse height at 18 different positions on each scintillator was calculated and used to fit a response curve. The fitted parameters were put on a file and used for the analysis of that period.

2. To correct for small sensitivity changes during run time, caused by fluctuations in high voltage, gas mixture etc., cosmic ray data taken in-between machine bursts were used to calculate gain-constants for scintillators and proportional drift tubes. About 2500 cosmic events were necessary to create a calibration file with gain constants, which took on average less than one day during neutrino data taking. With this file pulse heights of scintillators and proportional tubes were converted to visible energy of equivalent amount of minimum-ionizing particles.

3. The ratio of visible energy over shower energy as function of shower energy was determined by exposing the detector to test beams of π^- (5 – 140 GeV) and e^- (5 – 50 GeV). Here also the vertex and shower angle resolution were measured. In addition the test beam data were used for the development of software to separate electromagnetic and hadronic showers. The energy resolution of the scintillators

for hadrons was $[(44.3/\sqrt{E}+8.1)\pm 1.8]$ % and for electrons $[(18\pm 1)/\sqrt{E}]$ % (E in GeV). The complete parametrization of the detector response is given in [70].

4. The momentum of a muon traversing the magnetized iron of frame or end-system is obtained by a least-square fit of start position, direction and $1/p_\mu$ to the track position from the PDT-system according to a method of Regler [31]. Multiple scattering and energy loss of the muon are taken into account. The measurement of the magnetic field strength in the iron is described above. The momentum resolution for 80 GeV/c muons was approximately 25% in the frame magnet and 16% in the forward muon spectrometer. For muons stopping in the detector the momentum could be determined from the range.
   For some muons stopping in the end-system the momentum could be determined both by a fit to the track curvature and by range. In fig.30 both methods are compared and show agreement.

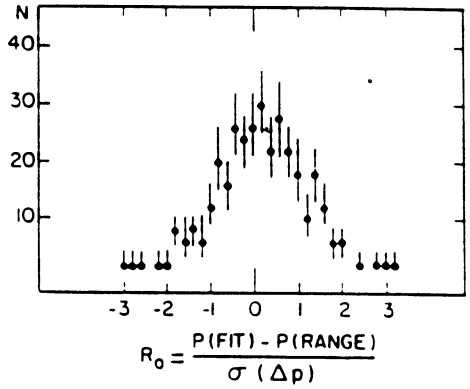

Figure 30: Observed difference of momentum determined by range and by magnetic deflection in units of the standard deviation, $R_0 = \{p(fit) - p(range)\}/\sigma(\Delta p)$. The mean value of R_0 is consistent with zero, the standard deviation of the R_0 values is about 1, as expected.

4. DATAHANDLING

4.1 INTRODUCTION

This chapter will describe the data flow. The events recorded on tape were sorted in classes of already known interaction types, to compare the rates with theoretical predictions and to search for new event types.
First incomplete or corrupted data had to be discarded, also bursts which showed too much beam loss were not used. After that a fast filter routine removed the events which were obviously caused by cosmic ray interactions during the burst gate, before the data was passed to the main event reconstruction program.

Events which could have been caused by a charged current muon neutrino interaction, i.e. events with a long enough track pointing to the shower vertex, were classified as (1μ)-event.
The remaining events were classified as (0μ)-event if a shower was present, otherwise as "cosmic", i.e. a possible cosmic ray event which passed the fast filter routine.
The event classification was performed separately for density one and density one-third data. Events without a clear signature were flagged by the program and were scanned later by eye. To determine the systematic error of the automatic event reconstruction, a random sample of 10 % of all events was also scanned by eye for a possible misclassification by the program.

Corrections had to be made for misclassifications of physical origin: some charged current muon neutrino events had an "unrecognizable" muon, hidden in the shower or leaving the detector at the side; decaying pions or kaons in the shower or "punch through" tracks sometimes faked a (1μ)-event; some cosmic ray interactions fulfilled the (1μ) or (0μ) criteria. The measured shower energy and muon momentum spectra had to be corrected for detector acceptance and smearing.

The (1μ)-sample was subdivided into ($1\mu^-$)- and ($1\mu^+$)-events according to the momentum sign of the track(s) as determined by the deflection in the magnetized parts of the detector, to separate CC ν_μ and $\bar{\nu}_\mu$ events respectively. A correction was necessary for (1μ) events for which the momentum fit failed.

In the (0μ) sample a search was made for charged current electron neutrino interactions. By using the ratio NC/CC measured in narrow-band neutrino beams the amount of NC ν_μ and ν_e events in the (0μ) sample could be estimated from the amount of CC events, where it was assumed that the NC/CC-ratio for both neutrino types were the same. In this way one obtaines an upper limit for the amount of CC ν_e-events.
The amount of CC ν_e events in the (0μ) sample could also be determined "directly" using the difference in pattern between electromagnetic and hadronic showers: for every (0μ) event a probability was determined for being a CC ν_e interaction. With the help of the NC/CC-ratio the total amount of (0μ) events caused by ν_μ and ν_e was estimated. The result is used in chapter 8 to set a limit on tau neutrino production and to test the e-μ universality.

The prompt event rates were obtained by extrapolation to infinite target density. Some additional corrections were necesarry: the density one-third target had a limited length and part of the hadrons "leaked" in a region with density one. Material upstream of the dump, like the vacuum window of the beam pipe, caused a small background independent of the target density.
In chapter 5 another method to determine the prompt rates is described. In that chapter the conventional background is calculated by Monte Carlo simulation of the hadronic cascade in the dump and subtracted from the density one rates. For electron neutrinos, with a much smaller conventional background, this last method gives a smaller error than the extrapolation to infinite target density.

4.2 DATA TAKING

Data were taken in two periods, one of 38 days and one of 66 days, with in-between 92 days during which the water cooled $\rho = 1$ dump was replaced by an air-cooled one (see section 3.2). Care was taken that the amount of protons on the full density target was about twice that on the one-third density target in order to optimize the statistical accuracy in the extrapolation method. Both targets were regularly exchanged to minimize systematic

effects. The polarity of frame and end-magnets was changed every few hours to create focussing conditions of equal time length for muon tracks of both signs to reduce the systematic error in the momentum determination. Special runs were made to calibrate the beam-loss monitors, to determine the cosmic background and to check the extrapolation method with the one-half density target (described in 3.1, 4.5.4 and appendix B, respectively). The physics-trigger was enabled for 33 μsec around the 23 μsec machine burst, as a compromise between the tolerance for jitter in the beam timing and cosmic ray background reduction. The trigger condition required during the burst gate in at least four scintillator planes at least one hit and no hits in the first two planes. This condition was fully efficient for showers of energy > 1.5 GeV and for muon tracks of E > 200 MeV. In fig.1 the range of a 1 GeV muon is indicated.

4.3 EXPOSURE

The number of protons on target (POT) collected in this experiment is given in table 3. A certain amount of the data had to be discarded from analysis due to defects, such as problems with the SPS data-links (1.7%), which caused (part of) the beam information to be missing, and malfunctioning of the detector or data acquisition systems (3.1%). In addition data was not used if beam steering equipment (see 3.1) was placed in the beam (4.2%) or if the beam-loss monitors showed beam scraping which could give a contribution to the prompt ν-rate of more than 1% of the expected rate (1.4%, see appendix D).

Because it took 15 μsec to read the event into the local memories after each trigger, during which no new events could be recorded, the effective amount of protons had to be corrected for this dead-time. The dead-time was calculated with the help of small scintillation counters, which registered the muon flux in the shield. The neutrino flux is proportional to this muon flux. One scaler counted all scintillator pulses, another one was blocked during the time that the detector was busy. The lifetime fraction was taken as the ratio (blocked scaler)/(unblocked scaler). Several checks were made on the dead-time calculation (see appendix D). The result was a dead-time of on average 13.6% for density one and 21.7% for density one-third.
The protons actually used for analysis were $13.26 \cdot 10^{17}$ for $\rho = 1$ and $6.35 \cdot 10^{17}$ for $\rho = 1/3$, which is 72% of the total number of protons incident on target.

4.4 EVENT RECONSTRUCTION AND CLASSIFICATION

From the remaining sample first the events unambiguously caused by a cosmic ray interaction were rejected. The amount of cosmic events was $\approx$ 20 % for $\rho = 1/3$ and $\approx$ 40% for $\rho = 1$. It was checked by applying the filter routine on data taken in the wide-band neutrino beam, with a much lower cosmic ray background, that no neutrino-induced events fulfilling the trigger conditions were rejected. After cosmic ray filtering the main event reconstruction was carried out. For every event the program tried to reconstruct:

1. The interaction point (vertex).

2. The shower energy and direction.

3. Single tracks, their momentum and sign. If a particle traversed a sufficient amount of magnetized iron in frame or end-magnets, its momentum and sign could be determined by the deflection in the magnetic field. Otherwise the momentum was determined by the range of the track and if the track left the detector, a lower energy limit was derived (see section 3.4.8.). In fig.31 the efficiencies for the finding of muon tracks and for the reconstruction of their momentum are given.

The events with shower energy > 1.5 GeV or a track with a range corresponding to at least 1 GeV were kept for further analysis.
Next the remaining events were put in the following three classes:

1. (1μ): events with at least one track with E > 1 GeV pointing towards the reconstructed shower vertex within a radius of 20 cm in the plane of the vertex and a visible range outside the shower of more than 3

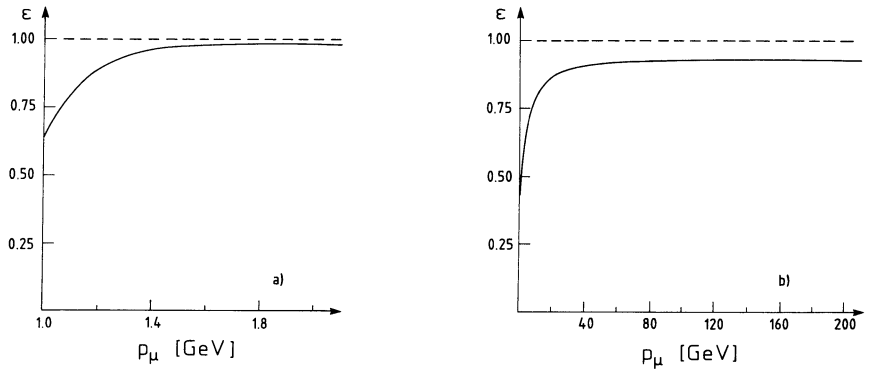

Figure 31: Efficiency for a) muon track finding, b) muon charge measurement.

absorption lengths, corresponding to 13 target plates or an energy of more than 0.67 GeV. This class covered most of the charged current (CC) muon neutrino interactions.

2. (0μ): events with shower energy > 1.5 GeV and no tracks fulfilling the (1μ) conditions. This class covered most of the neutral current (NC) ν_μ, ν_e and charged current ν_e interactions.

3. cosmics etc.: events with E_{shower} < 1.5 GeV and no track fulfilling the (1μ) conditions.

Only events were used for the analysis for which the vertex was located within a fiducial volume restricted longitudinally to plane 3 and 59 and laterally to a surface of 2.4 x 2.4 m^2 around the beam axis. Plane one and two were used to veto incident muons, plane 60 to 72 and the end-system served for shower measurements and event classification. The iron frames and outer 30 cm of the marble were used for shower measurements and to veto cosmic ray muons. The fiducial mass was 90.6 tons.

4.5 CORRECTIONS TO EVENT CLASSIFICATION

The number of events found with the reconstruction program in the (1μ) and (0μ) classes had to be translated into the physical classes of events with and without a primary muon, respectively.
The first step was to assure that the reconstruction program was operating correctly; this was checked with a scan by eye.
Other corrections were necessary to allow for the differences of the classification criteria and the distinction between the physical processes, i.e. some primary muons were not visible according to the classification rules and some tracks classified as primary muons had other origins.
A further correction was needed for backgrounds in the beam and for cosmic ray background.

4.5.1 SCAN

In order to check the software of the event selection the display of some events was printed on microfiche (see fig.32) and scanned by eye.
Two groups of events were scanned:

1. Events in which a scan flag was set by the reconstruction program and events with shower energy smaller than 5 GeV. This group contained 23 % of all events. A scan flag was set in case the features of the event were close to the class boundaries, e.g. the lateral difference between muon vertex and shower vertex was bigger than 20 cm and smaller than 60 cm or the event had a vertex in the neighbourhood of the fiducial volume border. Also in case of (1μ) events with shower energy smaller than 10 GeV, (0μ) events with a reconstructed track of momentum bigger than 1 GeV or in case of

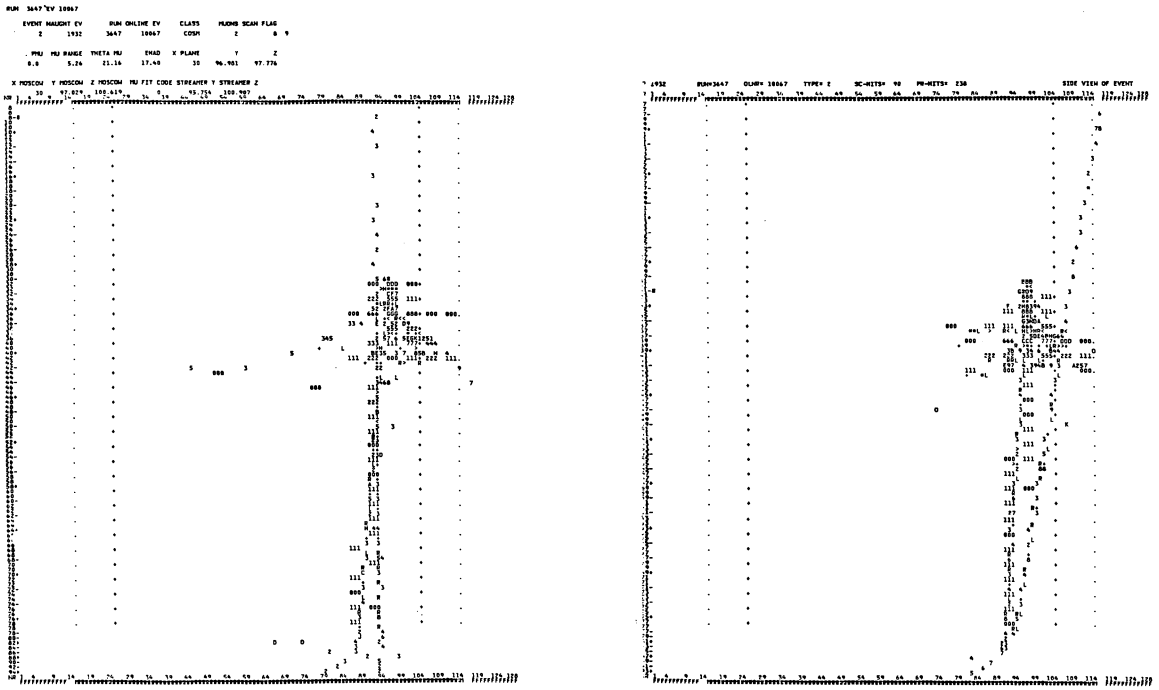

Figure 32: Event printout for the scan, top view (left) and side view (right) of the detector. The event is classified as cosmic event by the automatic pattern recognition and reclassified as charged current muon neutrino event by the scan. The reason of misclassification by the program was an overlaying cosmic track. The event got a scanflag from the program because the difference in postition between the start of the shower and the start of the muon was bigger than 3 planes.

ambiguities in the determination of the vertex position a scan flag was set. Events with low energetic showers were scanned because their vertex position was difficult to determine.

2. A random sample of 10% of all events, to determine the systematic error on the event classification.

Thus 31% of all events were scanned. The scanning was carried out twice by different scanners and judged by a third person. The result is shown in table 4 for all scanned events and for the 10 % sample as a separate class. The final result of the scanning was an increase by 2.1% of the (0μ)-sample and a decrease by 5.0% of the (1μ)-sample. The systematic error on classification can be represented by a standard deviation of $\sigma = \pm 0.3\%$ for each event class. The numbers of events for each class after scan correction are shown in table 45 and 46 of appendix G.

4.5.2 UNRECOGNIZED MUONS

Part of the charged current muon neutrino interactions contained an unrecognized muon because its energy was lower than 1 GeV or it left the detector at the side before creating a sufficiently long track. The amount of charged current muon neutrino events not classified as (1μ) for these reasons has been calculated with Monte Carlo methods using the measured x- and y-distributions for these interactions [72]. Misclassification also occurs if the track of the leading muon is (partly) hidden by the shower.
A correction was calculated by taking (1μ)-events, blanking out the leading muon and generating by Monte Carlo a new muon using the known x- and y-distributions. These events were passed again through the analysis program and scanned. The correction for unrecognized muons is given in fig.33 as function of energy for charged current neutrino and anti-neutrino interactions.

Table 4: Scanning results.

all scanned events = 7728 evts.

PROGRAM / SCAN	OCC	ONC	NC	CC	COSM
OCC	937	9	11	268	36
ONC	13	702	224	12	14
NC	8	81	1729	230	16
CC	224	1	29	2597	6
COSM	0	0	5	5	571

random sample, 10% of all = 2192 events

PROGRAM / SCAN	OCC	ONC	NC	CC	COSM
OCC	557	7	0	4	180
ONC	11	436	0	0	16
NC	0	1	168	3	3
CC	2	0	0	433	5
COSM	0	0	0	1	365

CC = (1μ)- event
NC = (0μ)- event
COSM = cosmic ray event
Oxx = outside fiducial volume

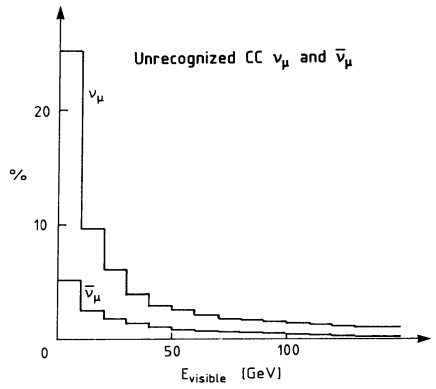

Figure 33: Probability for CC ν_μ events to be unrecognized as function of visible energy.

4.5.3 DECAY MUONS AND PUNCH-THROUGH TRACKS

Some events which are not caused by CC ν_μ interactions will be classified as (1μ) because the muon of a decaying π, K or a punch-through hadron created a track fulfilling the (1μ) conditions. A correction was determined by re-analyzing (1μ)-events from which the leading muon was removed. Events which were again classified as (1μ) were scanned and if the classification was found to be good, added to the correction. The correction was decreased by 0.5 % to take into account di-muon events caused by charm decay and is given in fig.34 as function of hadron shower energy.

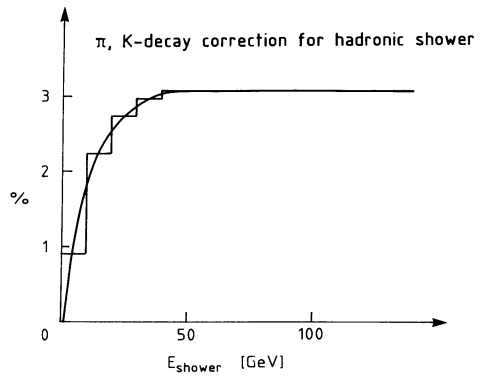

Figure 34: π, K decay correction for hadronic showers as function of shower energy.

4.5.4 COSMIC RAY BACKGROUND

Cosmic ray muons can fake (1μ) events if they stop inside the detector and they can fake (0μ) events if their track is very steep. In order to correct for cosmic ray events classified by the reconstruction program as (1μ) or (0μ) data were recorded with the beam off. The analysis was performed in the same way as for the neutrino data, including cosmic ray rejection, event classification and scanning. Accepted cosmic ray events were normalized to the effective lifetime of the experiment and subtracted. The cosmic ray correction is given for (1μ) and (0μ) in table 5.

Table 5: Cosmic ray background correction.

events caused by cosmic rays					
(1μ) ($p_\mu > 1$ GeV/c)		(1μ) ($p_\mu > 1$ GeV/c)		(0μ)	
E_{vis} [GeV]	ev/Ton/10^{18}p	E_{sh} [GeV]	ev/Ton/10^{18}p	E_{sh} [GeV]	ev/Ton/10^{18}p
> 1	0.247	–	0.247	> 1.5	0.222
> 5	0.055	> 2	0.030	> 2	0.111
> 10	0	> 5	0.018	> 5	0.046
		> 10	0	> 20	0.014
				> 40	0.006

E_{vis} = visible energy
E_{sh} = shower energy
$E_{vis} = E_{sh} + E_\mu$

4.5.5 NEUTRINOS NOT ORIGINATING FROM THE DUMP

Decaying pions and kaons produced in the residual gas of the decay tunnel or in the vacuum shield, SEM-grid just in front of the target or the air between tunnel and target created a small conventional neutrino-flux, independent of the target density. A list of material upstream of the dumps and the distance to the target is given in appendix F. A background was calculated of 0.6% of the conventional flux of the $\rho = 1$ target and with the same energy dependence.

The rate for (1μ)- and (0μ)-events corrected for unrecognized muons, decaying pions and kaons in the shower, cosmic background and upstream material are given in table 47 of appendix G as function of shower energy.

4.5.6 UNFOLDING OF EXPERIMENTAL RESOLUTIONS

The task of the unfolding is to reconstruct from the measured energy spectra the original neutrino energy spectra. The first are distorted by the energy resolution and acceptance of the detector. The following procedure was used to unfold the measured ($1\mu^{\pm}$)-spectra:

1. A folding matrix $M_f(E_g, E_o)$ was generated by Monte Carlo methods which gave for each generated energy E_g the spectrum of the observed energy E_o . The Monte Carlo program made use of the measured x- and y-distributions for charged current muon neutrino interactions [72].
   For hadronic showers the energy response and resolution was taken from measurements with the detector exposed to a pion test beam (see 3.4.8.).
   Muons of charged current muon neutrino interactions were tracked through the detector, taking into account the magnetic field in the different detector parts. The probability for a good momentum fit depended on the amount of magnetized iron traversed by the muon; the momentum resolution was better in the end-system than in the frame. Even in the case of a muon traversing all the PDT-planes of the end-system, the fit probability was smaller than unity ($\eta = 0.94$) because of bremsstrahlung, which could make a kink in the track and delta-ray-production, which could devaluate the drift time information. When a fit failure occurred the muon was assigned the energy of the visible range. The correction for unrecognized muons and for decaying pions and kaons in the shower were included in $M_f(E_g, E_o)$.

2. By an iterative procedure the spectrum was obtained that after folding with $M_f(E_g, E_o)$ reproduced the observed spectrum. This was done with the spectra of ($1\mu+$), ($1\mu-$), (1μ all) for both magnet polaritys (each with their proper $M_f(E_g, E_o)$), until consistency was reached, i.e. for all cases the same spectrum was acceptable ("1μ all" denotes $1\mu^- + 1\mu^+ +$ events with muon fitted by range).

3. With the spectra for $\rho = 1$ and $\rho = 1/3$ a standard acceptance calculation was performed: all events with visible energies above 20 GeV and measured muon momentum higher than 5 GeV/c were used to determine the charged current event rate with neutrino energies above 20 GeV. With these cuts the cosmic background was negligible, the correction for π/K decay was very small, and the fit efficiency for the muon momentum was much higher. The unfolded spectra were normalized with the event rate above 20 GeV from this acceptance calculation.

The unfolded spectra for charged current muon neutrinos and anti muon neutrinos of both target densities are given in table 48 of appendix G.

4.6 THE (0μ)-SAMPLE

One of the tasks of the analysis was to study the origin of events in the (0μ) sample. After correcting for ν_μ CC events, where the primary muon was not recognizable, this sample contained ν_μ NC interactions, ν_e NC and CC interactions, and could contain a number of events of unknown origin.
The number of ν_μ NC events can be predicted from the observed number of ν_μ CC events and these can be subtracted. This procedure is described in this section. The remaining sample contained all ν_e interactions and possibly interactions from unknown sources.
The analysis was continued along two pathes. The first was to assume that the ν_e interactions dominate this sample, and use this event sample as an upper limit for the contribution of ν_e events in the detector. The second path was to attempt to recognize CC ν_e interactions from their specific event topology. The direct search for CC ν_e interactions is described in section 4.6.2 .

4.6.1 CHARGED CURRENT ELECTRON-NEUTRINO RATE FROM UNFOLDING $(0\mu) - (NC/CC)\cdot(1\mu)$

The (0μ)-sample consists of NC $(\nu_\mu + \bar{\nu}_\mu)$-events, (CC + NC) $(\nu_e + \bar{\nu}_e)$-events and possibly events caused by yet undiscovered neutral penetrating particles. The NC ν_μ component can be removed by using the (1μ) shower energy spectrum and the measured NC/CC- ratio.
Thus

$$\text{NC-}\nu_\mu = R \times \text{CC-}\nu_\mu \tag{61}$$

where R is the NC/CC-ratio for muonneutrino and anti-muonneutrino, which is measured in narrow-band neutrino beams [73] and found to be:

$$R = \sigma^{NC}(\nu_\mu)/\sigma^{CC}(\nu_\mu) = 0.313 \pm 0.003 \tag{62}$$

$$\overline{R} = \sigma^{NC}(\bar{\nu}_\mu)/\sigma^{CC}(\bar{\nu}_\mu) = 0.395 \pm 0.014 \tag{63}$$

for shower energies greater than 2 GeV.
An average value of R was calculated by

$$<R> = [\, R \cdot N(\mu^+) + \overline{R} \cdot N(\mu^-)\,]/[\, N(\mu^-) + N(\mu^+)\,] \tag{64}$$

Within errors the same result for both densities was found:

$$<R> = 0.333 \pm 0.004 \tag{65}$$

The NC/CC-ratios (62) and (63) were measured in narrow-band beams of 160 GeV and 200 GeV, with a cut in hadron energy of 2 GeV. Thus the NC/CC-ratios were measured at $y \geq 0.0125$ and the difference with σ_{NC}/σ_{CC} is negligible.

Using equation (61) with R from (64), it is neglected that the y-distributions of ν_μ and $\bar{\nu}_\mu$ interactions on an isoscalar target are not the same for CC and NC, as explained in section 2.2.2 . The y-distributions for CC- and NC-interactions would be the same only in case of equal neutrino and anti-neutrino fluxes with the same energy distribution.
To investigate the effect of this neglect, a Monte Carlo simulation was made.
Input to the M.C. were the energyspectrum of conventional ν_μ and $\bar{\nu}_\mu$ events, the prompt energyspectrum for ν_μ and $\bar{\nu}_\mu$ (simulated with the $D\overline{D}$ model, see section 6.2.1.) as determined with the help of equation (61) and (64). Further inputs were the NC/CC ratios (62) and (63) and the y-distributions for CC ν_μ, $\bar{\nu}_\mu$ and NC ν_μ, $\bar{\nu}_\mu$, as given in respectively equation (41), (42), (45) and (47) of section 2.2.2 .
The result of this M.C. simulation was a correction factor on R from equation (64) of 0.99 for $E_{had} > 2$ GeV, 0.98 for $E_{had} > 20$ GeV and 0.95 for $E_{had} > 80$ GeV. If in the following the term " $(0\mu) - 0.33\cdot(1\mu)$ " is used, above corrections are applied.

The $(0\mu) - 0.33\cdot(1\mu)$ spectrum as function of shower energy was unfolded to get the spectrum of charged current electron neutrino events as function of neutrino energy, assuming only (CC + NC) ν_e-events contributed, the y-distributions and NC/CC-ratio were the same as for muon neutrinos [51] and the ν_e-flux was equal to the $\bar{\nu}_e$-flux.
The unfolding method was similar to the one used for the (1μ)-spectra, the energy response and resolution of the detector for electrons had been measured in an electron test beam (see 3.4.8.). The energy spectrum was determined that yielded the measured $(0\mu) - 0.33\cdot(1\mu)$ spectrum, after folding with the detector response. This spectrum consisted thus of CC + NC ν_e-events. With the help of the y-distributions of section 2.2.2., the CC component was derived. In table 7 the rates for charged current electron neutrino events are given for both target densities and three energy cuts. In fig.37 of section 6.2.1. the effect of the unfolding on the $(0\mu) - 0.33\cdot(1\mu)$ spectrum is given for target density one, together with the unfolded charged current ν_e spectrum, also given in table 49 of appendix G.

4.6.2 DIRECT SEARCH METHOD FOR CHARGED CURRENT ELECTRON-NEUTRINO EVENTS

As an alternative for the method described in the previous section, a more direct separation of electron-neutrino induced charged current events from all muonless events was performed by a special algorithm. The method is described extensively in [51], [69] and [70]. In the case of ν_e and $\bar{\nu}_e$ induced charged current events the shower detected in the calorimeter consists of two components, an electromagnetic part induced by the electron, and a hadronic part induced by the recoiling hadron system. In most cases these two components are not separated in space. To recognize an electron shower and to measure the energies of the electron and hadron showers separately, use has been made of the narrow width (2.5 cm FWHM) and the regular longitudinal development of electron showers, in contrast to the broader and irregular hadron showers (typically 20 cm FWHM).

Response and resolution of the algorithm were calibrated with data recorded in electron and pion test beams and with the help of measured charged current muon-neutrino events, from which the muon was replaced by an electromagnetic shower of the same energy and direction.

The search was applied to all (0μ) events of the beam dump data. The resulting y-distributions, where $y = (E_{total} - E_{electromagnetic})/E_{total}$, are composed of two parts, one from genuine CC ν_e and $\bar{\nu}_e$ events, and another one from the background of NC events, for which in general also an electromagnetic component is found, either due to a π^0 produced at the vertex or simply because a part of the hadronic shower fulfills the criteria. These y-distributions were determined in bins of shower energy for both target densities.

The two components were separated with a statistical analysis. The shape of the background distribution was determined by applying the method to NC events of the same energy distribution recorded in the wide-band beam using the same trigger conditions. Events obtained in the ν_μ and $\bar{\nu}_\mu$ beam were mixed to account for an equal flux of ν and $\bar{\nu}$. The wide-band beam contained a small contamination of ν_e and $\bar{\nu}_e$ of about 2.0% on average [44] [45], which is taken into account in the analysis. To determine the shape of the CC ($\nu_e + \bar{\nu}_e$) y-distribution a flux ratio of $\bar{\nu}_e/\nu_e = 1$ for prompt electron-neutrinos was assumed and the y-distribution was folded by Monte Carlo calculation with the experimentally determined shift and resolution function for $y_{measured}$. The relative amount of the two components, ($\nu_e + \bar{\nu}_e$) events and NC background, was then determined by a fit to the experimental distribution. The resulting y-distributions were found to agree well with the Monte Carlo predictions.

The energy dependence of the CC ($\nu_e + \bar{\nu}_e$) rates found by this method is given in table 6 for both target densities.

Comparison with the charged current electron neutrino events obtained by unfolding the $(0\mu) - 0.33 \cdot (1\mu)$ sample given in table 7 and table 49 of appendix G shows agreement. This is a proof that the (0μ) sample consists mainly of NC ν_μ and (NC + CC) ν_e events. This statement will be developed quantitatively in chapter 8.

4.7 THE EXTRAPOLATION METHOD

The prompt contribution can be calculated in two different ways. One is to use the data of both target densities and to perform an energybin-wise extrapolation to "infinite" target density as described in chapter one. The other method is to subtract from the density-one data the conventional contribution generated with a Monte Carlo method. This latter method will be described in chapter five.

In the extrapolation procedure a correction had to be made for the fact that the density 1/3 target had a longitudinal dimension of only 6.7 proton interaction lengths (1m of copper) and part of the hadrons leaked into the catcher, which had density one (see appendix B).
For the conventional flux produced in the first meter of the full density target, $C_{(\rho = 1, 1m\ of\ Cu)}$, one has:

$$C_{(\rho = 1, 1m\ of\ Cu)} = (R_{1/3} - R_1)/2$$

Table 6: Measured charged current conventional + prompt ($\nu_e + \bar{\nu}_e$) events per ton and 10^{20} POT from direct search.

E_ν [GeV]	$\rho = 1$	$\rho = {}^1/_3$
2 – 10	38.0 ± 19.5	48.7 ± 43.1
10 – 20	26.0 ± 16.4	72.8 ± 27.4
20 – 30	36.8 ± 9.9	65.9 ± 21.1
30 – 40	38.0 ± 8.4	54.7 ± 14.8
40 – 50	55.1 ± 8.5	71.6 ± 14.5
50 – 60	43.6 ± 10.6	79.9 ± 18.8
60 – 70	30.5 ± 7.8	47.1 ± 16.8
70 – 80	42.1 ± 11.7	23.6 ± 24.5
80 – 90	49.3 ± 11.2	41.8 ± 16.6
90 – 100	27.1 ± 8.8	46.2 ± 16.8
100 – 120	40.7 ± 9.0	37.1 ± 15.7
≥ 120	14.3 ± 12.7	4.9 ± 18.2
≥ 2	441.5 ± 40.6	594.1 ± 76.4
≥ 20	377.5 ± 31.6	472.7 ± 57.0
≥ 80	131.4 ± 21.1	130.0 ± 33.7

from equation (1), where R_ρ stands for the rate of target density ρ. The leakage, i.e. the conventional flux produced beyond the first meter of copper of the full density target can be expressed as a percentage of the conventional flux produced within the first meter of copper and as function of neutrino energy.
For the prompt signal one can write:

$$P = 3/2 \cdot R_1 - 1/2 \cdot R_{1/3} - \alpha(E_\nu) \cdot (R_{1/3} - R_1)/2 \qquad (66)$$

see equation (1), in which α = leakage calculated in section 5.1.1. and given in table 12 plus correction for upstream material, given in section 4.5.5 .

The extrapolated prompt rates for charged current muon neutrino and electron neutrino events are given in table 7 .

4.8 SYSTEMATIC ERRORS

The error sources, other than event statistics, taken into account in table 7 are:

1. Event classification, mainly due to uncertainties of the vertex position: from the scanning procedure an uncertainty of ±0.3% of the observed events was derived.

2. Shower energy calibration: the absolute calibration of the shower energy had an error of ±3% [70]. This caused a variation of ±0.4% in the number of events above an energy of 20 GeV.

3. Correction for cosmic ray background. The errors are given in table 5.

4. Correction for the decay of pions and kaons in the hadronic shower with a muon in the final state: the error is ±27% of the correction, mainly due to the statistics of the events available for the correction. The correction is shown in fig. 34.

Table 7: Corrected charged current event rates per ton and 10^{18} POT ±(stat. error) ±(syst. error).

Rates with a cut in neutrino energy			
	$E_\nu \geq 2$ GeV	$E_\nu \geq 20$ GeV	$E_\nu \geq 80$ GeV
ν_μ: $\rho = 1$	18.89±0.51±0.53	12.60±0.38±0.36	3.24±0.20±0.09
$\rho = {}^1/_3$	49.76±1.76±1.34	30.67±0.85±0.85	7.03±0.39±0.19
prompt extrapolated	2.61±1.22±0.44	3.25±0.72±0.29	1.29±0.36±0.07
prompt subtracted	3.12±0.51±1.65	3.48±0.38±1.00	1.14±0.20±0.31
$\bar{\nu}_\mu$: $\rho = 1$	6.58±0.32±0.18	3.69±0.21±0.11	0.70±0.09±0.02
$\rho = {}^1/_3$	16.21±0.70±0.43	7.76±0.41±0.21	1.22±0.16±0.03
prompt extrapolated	1.50±0.62±0.16	1.59±0.38±0.09	0.43±0.15±0.02
prompt subtracted	2.54±0.32±0.48	1.71±0.21±0.28	0.48±0.09±0.07
$\nu_\mu + \bar{\nu}_\mu$: $\rho = 1$	25.47±0.61±0.71	16.29±0.43±0.47	3.94±0.21±0.11
$\rho = {}^1/_3$	65.97±1.90±1.79	38.43±0.95±1.06	8.25±0.42±0.22
prompt extrapolated	4.11±1.37±0.60	4.83±0.82±0.38	1.72±0.39±0.09
prompt subtracted	5.66±0.61±1.92	5.19±0.43±1.10	1.63±0.21±0.33
$\nu_e + \bar{\nu}_e$: $\rho = 1$	4.64±0.28±0.17	3.80±0.22±0.11	1.21±0.11±0.02
$\rho = {}^1/_3$	6.12±0.57±0.44	5.46±0.43±0.23	1.64±0.19±0.03
prompt extrapolated	3.84±0.51±0.12	2.94±0.40±0.09	0.98±0.19±0.03
prompt subtracted	3.43±0.28±0.24	3.17±0.22±0.14	1.13±0.11±0.02

5. Correction for unrecognized muons: the error is ±10% of the correction, derived from variations of the input assumptions into the Monte Carlo calculation. The correction is shown in fig.33.

6. Correction for material upstream of the dump: the error is ±8% of the correction from an estimated uncertainty of material and its effect on neutrino production (see appendix F).

7. Normalization to protons on target (POT): the error is ±0.5% due to random fluctuations of BCT measurements, plus ±0.5% due to imperfections in proton accounting in the analysis program, plus ±0.8% due to errors in dead-time measurements (see appendix D). These errors are added in quadrature.

8. Corrections due to leakage of hadrons out of the $^1/_3$ density target. The errors are given in section 5.1.1..

9. Acceptance of muon-neutrino and muon anti-neutrino events as function of neutrino energy. From a variation of assumptions entering in the calculations an error of ±2.5% on the rates was estimated.

10. Error on the average ratio $<R>$ of NC/CC for muon-neutrino interactions. The error of ±1.3% is a combination of the errors on the measurement of R and $\bar{R}$ and the uncertainty on the relative neutrino to anti-neutrino flux in this experiment.

11. Uncertainty of the density of the dump targets: an uncertainty of ±0.5% on the knowledge of the density of the $\rho = {}^1/_3$ target was assumed, based on mechanical tolerances of 0.4% and muon flux measurements with three different target densities (see Appendix B.)

To treat the propagation of these systematic errors in the various steps of the analysis it was assumed that they can be represented by Gaussian distributions with standard deviations as given in the list above. A Monte Carlo program was used to evaluate the final systematic error on derived quantities. This program took into account all known correlations of errors.

5. MONTE CARLO SIMULATION OF CONVENTIONAL LEPTON FLUX

Another way of determining the prompt neutrino flux is to simulate the conventional background by Monte Carlo methods and to subtract it from the total data sample. This method has the advantage that it gives a smaller statistical error. On the other hand one introduces new systematic errors due to uncertainties in the Monte Carlo program.

The main reason for applying this second method is to have a consistency check on the extrapolated result. The Monte Carlo program can be tuned such that it reproduces the measured (see appendix B) conventional muon flux, which limits the systematic error on the conventional neutrino flux. Since the Monte Carlo program used here also produces hyperons, it is possible to make an estimate of the conventional electron neutrino flux.

A next step is to generate also the prompt di-muon flux from non-charmed resonance decay and other well-known sources, in order to check models explaining the remaining prompt neutrino and muon signals.

5.1 CONVENTIONAL CHARGED CURRENT MUON NEUTRINO EVENTS

With the help of the Monte Carlo program FLUKA (see [1] and appendix A) the hadronic shower induced by 400 GeV protons hitting a thick copper target have been simulated. This program used the technique of weighting: pions, kaons and hyperons decay into muons, electrons and their neutrinos with a weight P depending on their lifetime, branching ratio, velocity and mean free path length (see table 8). At the same time they continue to reinteract with a weight $1-P$.
The muons thus generated were tracked through the iron shield with the help of a Monte Carlo program, treating the energy loss by bremsstrahlung, pair production, ionization and nuclear interaction as a stochastic process [91] and thus introducing range straggling. The production Monte Carlo is normalized (see appendix A) with the measured muon flux in the iron shield (see appendix B).
With the Monte Carlo thus tuned, the neutrino flux was generated in the fiducial volume of the CHARM detector (Θ < 2.78 mrad), with a lower energy cut of 2 GeV. To calculate the amount of charged current events the cross-sections given in point 4 below have been used. The result is shown in table 9 and fig. 35. In fig.35 also the contributions from pions and kaons are given separately.
The conventional muon neutrino flux is closely related to the conventional muon flux. The following systematic errors were taken into account:

1. Uncertainty in normalization with measured muon flux: the Monte Carlo was normalized with the measured muon flux in pit 1, 2, 3, 4 and 5 of the iron shield (see fig.16). Uncertainties in this normalization are caused by the error of the muon flux measurements and an error in the energy loss of the generated muons in the iron shield. The last error is due to a limited knowledge of the density of the iron shield and uncertainties in the specific energy loss of muons in iron. These errors propagate as uncertainties in the generated neutrino flux. More details can be found in appendix A.

2. π/K-ratio:
from comparison of the Monte Carlo results with the measurements (see appendix A) it follows that an uncertainty of 10% in the π/K-ratio has to be allowed for. Taking this error into account in the muon and neutrino flux an error was found as given in table 10.

3. Dependence on transverse momentum (p_T): since the CHARM detector sees only the very forward produced neutrinos, a variation of the p_T-distribution of pions and kaons influences the neutrino flux in the detector. The Monte Carlo program used here has the advantage that it yields directly produced particles, so that a substantial part of the p_T-behaviour is governed by decay kinematics: even if the direct produced hadron would get $p_T = 0$, its decay products would have a non-zero p_T(see appendix A). Non-charmed resonances are given a p_T-distribution of the form:

$$\partial\sigma/\partial p_T \propto p_T \exp(-3.3 p_T^2)$$

Table 8: Sources of conventional leptons.

MUONS					
DECAY MODE	BRANCHING RATIO	MASS [GeV/c^2]	INT.ACTION LENGTH [cm]	LIFE TIME [sec.]	DECAY FACTOR* [GeV]
$\pi^{\pm} \rightarrow \mu^{\pm}\nu$	1.00	0.14	17.8	$0.26\ 10^{-7}$	$0.32\ 10^{-2}$
$K^{\pm} \rightarrow \mu^{\pm}\nu$	0.6551	0.494	21.5	$0.124\ 10^{-7}$	$0.19\ 10^{-1}$
$K^{\pm} \rightarrow \mu^{\pm}\nu\pi^0$	0.0318	0.494	21.5	$0.124\ 10^{-7}$	$0.91\ 10^{-3}$
$K_L^0 \rightarrow \pi^{\pm}\mu^{\pm}\nu$	0.271	0.498	21.5	$0.518\ 10^{-7}$	$0.19\ 10^{-2}$
$K_S^0 \rightarrow \pi^{\pm}\mu^{\pm}\nu$	$4.67\ 10^{-4}$	0.498	21.5	$0.89\ 10^{-10}$	$0.19\ 10^{-2}$
$\Lambda \rightarrow p\mu^-\nu$	$0.157\ 10^{-3}$	1.116	14.8	$0.263\ 10^{-9}$	$0.33\ 10^{-3}$
$\Sigma^- \rightarrow n\mu^-\nu$	$0.45\ 10^{-4}$	1.197	14.8	$0.148\ 10^{-9}$	$0.18\ 10^{-2}$
ELECTRONS					
DECAY MODE	BRANCHING RATIO	MASS [GeV/c^2]	INT.ACTION LENGTH [cm]	LIFE TIME [sec.]	DECAY FACTOR* [GeV]
$K^{\pm} \rightarrow e^{\pm}\nu\pi^0$	0.0482	0.494	21.5	$0.124\ 10^{-7}$	$0.14\ 10^{-2}$
$K_L^0 \rightarrow \pi^{\pm}e^{\pm}\nu$	0.387	0.498	21.5	$0.518\ 10^{-8}$	$0.27\ 10^{-2}$
$K_S^0 \rightarrow \pi^{\pm}e^{\pm}\nu$	$6.66\ 10^{-3}$	0.498	21.5	$0.892\ 10^{-10}$	$0.27\ 10^{-2}$
$\Lambda \rightarrow pe^-\nu$	$0.837\ 10^{-3}$	1.116	14.8	$0.263\ 10^{-9}$	$0.18\ 10^{-2}$
$\Sigma^+ \rightarrow \Lambda e^+\nu$	$0.20\ 10^{-4}$	1.189	14.8	$0.800\ 10^{-10}$	$0.15\ 10^{-3}$
$\Sigma^- \rightarrow ne^-\nu$	$0.10\ 10^{-2}$	1.197	14.8	$0.148\ 10^{-9}$	$0.40\ 10^{-2}$
* (decay factor)/energy → average decay probability per interaction					

where the error on the constant in the exponent is assumed to be 10% (see appendix A). This error gives an uncertainty on the neutrino flux in the CHARM detector as given in table 10

4. Neutrino-nucleon cross-section: a charged current cross-section for muon neutrinos of $(0.77 \pm 0.04) \cdot 10^{-38}$ cm^2/GeV for 2 GeV < E_ν < 10 GeV and of $(0.67 \pm 0.03) \times 10^{-38}$ cm^2/GeV for 10 GeV < E_ν < 400 GeV was used. For muon anti-neutrinos these numbers were $(0.31 \pm 0.01) \cdot 10^{-38}$ cm^2/GeV and $(0.32 \pm 0.01) \cdot 10^{-38}$ cm^2/GeV respectively. These figures are based on data given in [93] page 120. The influence of the errors on the neutrino flux is given in table 10.

5. Neutrino/anti-neutrino ratio: from appendix A it follows that there is a small discrepancy in the ratio (positive mesons)/(negative mesons) between Monte Carlo and measurements (ca 10% at $x_F = 0.2$). A correction for this was made (see Appendix A) and the full correction taken as error given in table 10 .

All errors were added quadratically and the final result is given in table 10 .
The predicted conventional flux from the M.C. is compared with the result from extrapolation in fig.35 (both event rates are for the first meter of copper only, see next section). The prompt charged muon neutrino event rate obtained by subtraction of the generated conventional fraction from the density one rate is given in table 7 and is in agreement with the result obtained from extrapolation to infinite target density.

Table 9: Rates of conventional CC ν_μ events for $\rho = 1$ target from Monte Carlo.

events per ton and 10^{20} protons on target		
E_ν [GeV]	ν_μ	$\bar{\nu}_\mu$
2 – 10	366.5	109.1
10 – 20	298.6	97.4
20 – 30	226.8	66.1
30 – 40	157.7	40.0
40 – 50	109.9	28.3
50 – 60	85.5	18.9
60 – 70	66.8	13.3
70 – 80	55.8	9.60
80 – 90	44.3	6.80
90 – 100	33.3	4.50
100 – 120	48.8	5.58
120 – 140	30.8	2.67
140 – 160	21.0	1.18
160 – 180	11.7	0.56
180 – 400	19.6	0.44

E_ν [GeV]	ν_μ	$\bar{\nu}_\mu$	$\nu_\mu + \bar{\nu}_\mu$
$\geq$ 2	1577±156	404±44	1981±178
$\geq$ 20	912±93	198±26	1110±99
$\geq$ 80	210±30	22±7	231±31

5.1.1 LEAKAGE OF DENSITY 1/3 TARGET

As is described in section 3.2 and appendix B, only the density of the first meter of copper was changed to 1/3 of solid copper. This meant that hadrons leaking out of the first meter gave rise to conventional neutrino flux seen as prompt in the extrapolation method. A correction was made for this by subtracting the flux induced by this leakage calculated by Monte Carlo. The Monte Carlo could be checked in producing the right neutrino leakage by comparing it with the measured muon leakage. The muon leakage was measured in special runs without the 3 m long copper block (called "catcher") behind the density 1/3 target (see appendix B). The leakage α is defined as the ratio of particles produced outside the first meter of copper over the particles produced inside the first meter. One has:

$$\alpha_N = [\Sigma_{(i=1,N)}\{(\lambda_i)^{N-1}\exp(-L/\lambda_i)\}]/[\Pi_{(j=1,N;j\neq i)}(\lambda_i - \lambda_j)] \qquad (67)$$

in which α_N is the leakage of the N^{th} generation in the production chain, λ_i the interaction length in copper for a particle of generation i and L is the length of solid copper in the density 1/3 target (in case of λ_is of the same value one can use the rule of de l'Hopital in (67)). In the catcher-out runs one only sees the first generation of muon leakage: the pions and kaons leaving the target have a 470 cm long decay path, so their muon yield is amplified with a factor 470/(interaction length) $\approx$ 26 ; they will re-interact in the iron, thus the reaction products will have the 'normal' mean free path length of one interaction length in iron $\approx$ 20 cm. For this restricted leakage one has with (67):

$$(\alpha_N)_{restricted} = \alpha_N - \alpha_{N-1}$$

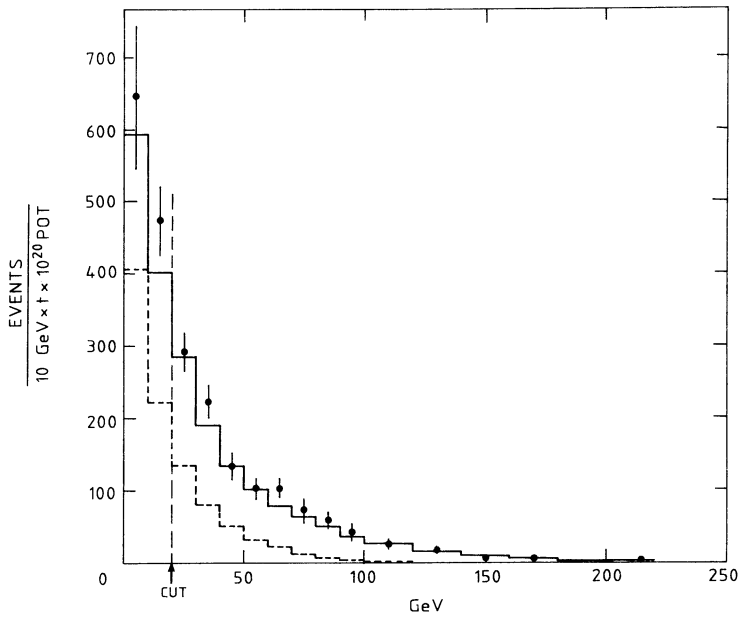

Figure 35: Measured conventional CC-ν_μ-events, using extrapolation to infinite target density. The Monte Carlo simulation is given as a histogram. The dashed part of the histogram gives the contribution not coming from K-decays.

In table 11 the measured leakage (see appendix B) is compared with the simulated first generation leakage. The good agreement is again an indication of the realistic behaviour of the Monte Carlo program. Also the total muon leakage is given in table 11, which will be used in section 5.3.5 .
The total leakage for the muon neutrinos generated by the Monte Carlo is given in table 12, the errors come from the uncertainties in hadron interaction lengths (see [50]).

5.2 CONVENTIONAL CHARGED CURRENT ELECTRON NEUTRINO EVENTS

The events in the CHARM detector coming from charged current interactions of electron neutrinos are given in table 13. They are generated by 3-body decay of kaons and hyperons (see table 8). It was assumed that the cross-section is equal to the muon neutrino charged current cross-section given in section 5.1 point 4. The neutrino energy spectra in the rest frames of the decaying kaons or hyperons were taken from [62].
In table 13 also the relative contributions of $K^\pm$, K^0 and hyperons to the electron neutrino flux are given. In table 14 the electron neutrino event rates due to leakage are given, calculated in a similar way as in the case of muon neutrinos.
Since the conventional ν_e flux is much smaller than the ν_μ flux, the effect of the leakage on the prompt rate is almost negligible. For the systematic error the uncertainty in muon flux normalization, π/K-ratio, p_T-distribution and an additional error on the production rate of hyperons (see appendix A) was taken into account. Also the fact has been used that the Monte Carlo reproduces rather well the conventional ν_μ event rate obtained by extrapolation, as is shown in fig.35. Most electron neutrinos come from kaon decay, the kaon contribution to the ν_μ events is indicated in fig.35 (99% of the conventional neutrino flux not coming from pion decay is due to kaon decay). The prompt charged current electron neutrino event rate obtained by subtraction of the conventional event rate generated by Monte Carlo is given in table 7 and is in agreement with the result obtained from extrapolation to infinite target density.

Table 10: Systematic errors on generated conventional CC muon neutrino event rate.

	muon neutrino event rate [evts./ton/10^{20} proton]		
	E_ν > 2 GeV	E_ν > 20 GeV	E_ν > 80 GeV
EVENT RATE	1577	912	210
normalization	4.7%	5.5%	8.3%
pit1	5.2%	3.3%	0.0%
π/K-ratio	0.7%	3.2%	8.6%
+/- ratio	2.8%	4.4%	6.0%
cross-section	5.0%	5.0%	5.0%
P_t-distribution	4.0%	2.8%	2.7%
TOTAL	9.9% (±156)	10.2% (±93)	14.5% (±30)
	muon anti-neutrino event rate [evts./ton/10^{20} proton]		
	E_ν > 2 GeV	E_ν > 20 GeV	E_ν > 80 GeV
EVENT RATE	404	198	22
normalization	4.9%	6.1%	9.7%
pit1	5.9%	4.0%	0.0%
π/K-ratio	1.2%	1.7%	7.6%
+/− ratio	5.5%	10.2%	28.0%
cross-section	3.0%	3.0%	3.0%
P_t-distribution	4.0%	2.8%	2.7%
TOTAL	10.8% (±44)	13.3% (±26)	31.0% (±7)
	total event rate [evts./ton/10^{20} proton]		
	E_ν > 2 GeV	E_ν > 20 GeV	E_ν > 80 GeV
EVENT RATE	1981	1110	231
normalization	4.7%	5.6%	8.5%
pit1	5.2%	3.3%	0.0%
π/K-ratio	0.3%	3.0%	8.5%
+/− ratio	1.1%	1.8%	2.7%
cross-section	4.0%	4.2%	4.5%
P_t-distribution	4.0%	2.8%	2.7%
TOTAL	9.0% (±178)	8.9% (±99)	13.4% (±31)

Table 11: Muon leakage.

PIT	measured 1st gen. %	M.C. 1st gen. %	M.C. all gen. %
2	3.0 ± 0.3	2.9	5.8
3	2.1 ± 0.3	2.3	4.4
4	1.7 ± 0.7	2.1	3.9
5	1.4 ± 0.7	1.8	3.5

Table 12: Muon neutrino leakage (α).

E_ν [GeV]	α %	E_ν [GeV]	α %
2 – 10	9.2 ± 1.2	80 – 90	3.8 ± 0.6
10 – 20	6.1 ± 0.8	90 – 100	3.3 ± 0.6
20 – 30	5.0 ± 0.7	100 – 120	3.3 ± 0.6
30 – 40	4.5 ± 0.7	120 – 140	3.2 ± 0.6
40 – 50	4.3 ± 0.6	140 – 160	3.1 ± 0.6
50 – 60	4.1 ± 0.6	160 – 180	3.0 ± 0.6
60 – 70	4.1 ± 0.6	180 – 200	3.0 ± 0.6
70 – 80	3.9 ± 0.6	> 200	3.0 ± 0.6
	> 2	5.6 ± 0.8	
	> 20	4.2 ± 0.6	
	> 80	3.3 ± 0.6	

5.3 PROMPT MUON FLUX FROM RESONANCE DECAY AND PAIR PRODUCTION BY PHOTONS

5.3.1 RESONANCE DECAY

Since the used Monte Carlo program features direct hadron production (see appendix A), i.e. hadron production before strong decay, an estimate can be made of the prompt muon flux coming from the di-muonic decay of non-charmed resonances. Because only 20 % of the pions and kaons are produced directly, most of the conventional μ-flux comes from resonances which have decayed into pions and kaons. This means that the production rate of the resonances is correlated with the conventional μ-flux. The raw M.C. is used as first estimation to give approximately the right resonance rate and is adjusted then (see appendix A) to yield the proper conventional μ-flux, after which the resonance production must be close to reality. In table 15 the decays of interest are given, with branching ratios and errors taken from [93].
In case of di-muon decay of ρ, ω and η' the branching ratio into e^+e^- was used, assuming e-μ universality and neglecting the difference in phase space. This was done because the $\mu^+\mu^-$ branching ratio had lower precision. The resonances were produced unpolarized (see [52]). In case of 3-body decay of η, ω, η' first a two-body decay was simulated into X, γ for η, η' and X, π^0 for ω. Thereafter the decay $X \rightarrow \mu^+\mu^-$ was simulated. The mass distribution of X was taken from measurements of Dzhelyadin et al. [53], [54], [55]. The resulting prompt flux is given in table 17 .

Table 13: Rates of conventional CC ν_e events for $\rho = 1$ target from Monte Carlo.

events per ton and 10^{20} protons on target		
E_ν [GeV]	ν_e	$\bar{\nu}_e$
2 – 10	20.7	8.4
10 – 20	18.8	9.9
20 – 30	11.7	7.7
30 – 40	8.3	4.8
40 – 50	6.5	3.1
50 – 60	4.5	1.9
60 – 70	3.11	1.21
70 – 80	2.39	0.75
80 – 90	1.73	0.48
90 – 100	1.24	0.35
100 – 120	1.65	0.40
120 – 140	0.75	0.20
140 – 160	0.35	0.10
160 – 180	0.18	0.03
180 – 400	0.09	0.02

E_ν [GeV]	ν_e	$\bar{\nu}_e$	$\nu_e + \bar{\nu}_e$
$\geq$ 2	82.0 ± 11.4	39.3 ± 6.2	121.3 ± 17.0
$\geq$ 20	42.5 ± 5.3	21.0 ± 3.3	63.5 ± 8.7
$\geq$ 80	6.03 ± 0.81	1.59 ± 0.24	7.62 ± 1.05

relative contributions to ν_e CC event rate above 2 GeV in %:		
source	ν_e	$\bar{\nu}_e$
K	52	28
K^0	43	38
Λ (50% error)	4	28
Σ (50% error)	0.5	7

5.3.2 MUON-PAIR PRODUCTION BY HIGHLY ENERGETIC PHOTONS

Another source of prompt muons is the Bethe-Heitler conversion of a photon into a $\mu^+\mu^-$ pair in the neighbourhood of a nucleus. For the probability of this process the ultra-relativistic limit was used:

$$P(\gamma \rightarrow \mu^+\mu^-)/P(\gamma \rightarrow e^+e^-) = (M_e/M_\mu)^2 = 2.34 \cdot 10^{-5}$$

as given in [62]. Sources of highly energetic photons taken into account are given in table 16.
Because of the absence of an helicity 0 state for the photon, the photon energy is not uniformly distributed over the muon pair:

$$\rho(x_1) \propto x_1^2 - x_1 + 3/4$$
$$x_2 = 1 - x_1$$

in which x_n = (energy muon n)/photon energy. The results are given in table 17 .

Table 14: Electron neutrino leakage (α).

E_ν [GeV]	α %	E_ν [GeV]	α %
2 – 10	10.3 ± 1.3	80 – 90	3.4 ± 0.6
10 – 20	6.6 ± 0.9	90 – 100	3.4 ± 0.6
20 – 30	5.3 ± 0.7	100 – 120	3.0 ± 0.6
30 – 40	4.8 ± 0.7	120 – 140	3.0 ± 0.5
40 – 50	4.0 ± 0.6	140 – 160	3.0 ± 0.5
50 – 60	3.9 ± 0.6	160 – 180	3.0 ± 0.5
60 – 70	3.8 ± 0.6	180 – 200	3.0 ± 0.5
70 – 80	3.7 ± 0.6	> 200	3.0 ± 0.5
		> 2	6.1 ± 0.9
		> 20	4.4 ± 0.6
		> 80	3.1 ± 0.6

Table 15: Branching ratios for di-muon decay of some resonances.

DECAY MODE	BRANCHING RATIO	
$\eta \to \mu\mu$	$(0.65 \pm 0.21) \cdot 10^{-5}$	
$\eta \to \mu\mu\gamma$	$(0.31 \pm 0.04) \cdot 10^{-3}$	
$\rho \to \mu\mu$	$(0.46 \pm 0.02) \cdot 10^{-4}$	*
$\omega \to \mu\mu$	$(0.67 \pm 0.04) \cdot 10^{-4}$	*
$\omega \to \mu\mu\pi^0$	$(0.10 \pm 0.02) \cdot 10^{-3}$	
$\eta' \to \mu\mu\gamma$	$(0.9 \pm 0.02) \cdot 10^{-4}$	
$\phi \to \mu\mu$	$(0.25 \pm 0.03) \cdot 10^{-3}$	*

* = e^+e^- value used

Table 16: Sources of highly energetic photons.

DECAY MODE	BRANCHING RATIO
$\pi^0 \to \gamma\gamma$	0.988
$\eta \to \gamma\gamma$	0.39
$\omega \to \pi^0\gamma$	0.087
$\eta' \to \rho^0\gamma$	0.30
$\to \omega\gamma$	0.028
$\to \gamma\gamma$	0.019

5.3.3 PRODUCTION OF MESONS WITH NON-ZERO ORBITAL ANGULAR MOMENTUM

So far only the production of pseudo-scalar and vector mesons was considered in the Monte Carlo. However from measurements given in appendix A it follows that a small amount of all mesons is produced with a non-zero orbital angular momentum. Since $L>0$ mesons are more heavy than the $L=0$ mesons, they are produced on average with a higher momentum than the latter. During decay this higher momentum is again distributed over $L=0$ mesons, which makes the negligence of $L>0$ mesons for the conventional μ- and ν-flux of small significance, even more so, since the total conventional μ-flux of the Monte Carlo is normalized with the measured one. Since the correlation between prompt and conventional μ-flux is not so strong as between conventional μ- and conventional ν-flux, a rough estimate has been made of the prompt μ-flux coming from $L=1$ mesons which decay in the resonances of table 15 . Unfortunately few measurements have been done on the production of $L=1$ mesons. Also their decay branching ratios are not always accurately known. One can fill in empty places in the data by applying symmetry rules, which gave here sufficient accuracy. From appendix A it follows that if $(20\pm 10)\%$ of $q\bar{q}$-pairs are classified as meson with $L=1$, all realistic rates are covered.
Only mesons with $L=1$ will be considered and it was assumed that the production rate of mesons with $L>1$ is negligible. The production rate is choosen proportional to $2J+1$, where $J=$ angular momentum quantum number. It was assumed that $f_0(1400)$, $f_1(1420)$, $f'_2(1525)$ are pure $s\bar{s}$-states with a negligible production rate. The considered $L=1$ mesons are given in appendix A.
In table 17 the prompt μ-flux caused by the decay of $L=1$ mesons is given, assuming that they account for 20% of all $q\bar{q}$-pairs. From table 17 it can be seen that the conventional μ-flux produced via $L=1$ meson decay differs not very much from the pseudo-scalar and vector meson contribution, as was expected. Also the prompt μ-flux does not show any radical changes. For this reason mesons with $L>1$, which are produced even more rarely, are neglected.

5.3.4 SYSTEMATIC ERROR ON PROMPT MUON FLUX

Since the conventional μ-flux is in most cases separated by one more decay step from the prompt μ-flux ($\rho\rightarrow\mu,\mu$; $\rho\rightarrow\pi,\pi\rightarrow\mu,\nu$), one can, for the determination of the systematic error, not rely only on the variation of some global parameters, as was done for the error on the conventional ν-flux, but one has to consider more details of the hadron production mechanism. Especially uncertainties in the classification of the quark anti-quark pairs created in the fragmentation process (see appendix A) are an important error source. Furthermore, the influence of the uncertainty in strange quark production and the error on the branching ratio of the resonances to di-muons will be treated.

PSEUDO-SCALAR MESON PRODUCTION

40 % of all quark anti-quark pairs created by the chain fragmentation mechanism (see appendix A) are classified as pseudo-scalar meson with $L = 0$ (the error on this rate will be discussed below).
If only one of the quarks is strange, unambiguously a K^+, K^0, K^- or anti-K^0 is created. In case of $u\bar{u}$, $d\bar{d}$ or $s\bar{s}$ pairs there is a choice between η, η' and π^0.
For the classification probability in case of a $u\bar{u}$ or $d\bar{d}$ pair it was assumed:

$$N(\eta, \eta') = N(\pi^0)$$

and

$$N(\eta) = N(\eta')$$

which was also used for $s\bar{s}$ pairs. (N(particle symbol) stands for the production rate of that particle). Since the mass difference between π^0 (0.136 GeV/c^2) on one side and η (0.549 GeV/c^2) and η' (0.958 GeV/c^2) on the other side is large, one can expect that η and η' are mixtures of $u\bar{u}$, $d\bar{d}$ and $s\bar{s}$. An equal production rate of η and η' was used, as suggested by SU(3)-symmetry [56], also used by [63] and [64]. But because of the large mass difference between the $I_Z=0$ particles η, η' and π^0, the first two could be more suppressed. From data given in [57] it follows that

$$\Delta N(\eta) = \pm 15\% \qquad \Delta N(\eta') = \pm 20\%$$

Table 17: Prompt and conventional μ-flux.

PROMPT μ-FLUX [$\mu/10^7$prot.]					
SOURCE		PIT 2	PIT 3	PIT 4	PIT 5
40% PSEUDO SCALAR	$\eta \to \mu\mu$	4.2	1.1	0.37	0.07
	$\eta \to \mu\mu\gamma$	79.9	15.6	3.28	0.37
	$\eta' \to \mu\mu\gamma$	27.9	8.1	2.62	0.57
	SUM	111.9	24.9	6.27	4.01
40% VECTOR	$\rho \to \mu\mu$	54.3	15.5	4.91	1.11
	$\omega \to \mu\mu$	69.2	19.8	6.00	1.28
	$\omega \to \mu\mu\pi^0$	34.8	7.0	1.33	0.15
	$\phi \to \mu\mu$	16.1	3.5	0.73	0.10
	SUM	174.4	45.8	12.9	2.6
20% L = 1	via η,η'	20.9	4.5	1.0	0.11
	via ρ,ω,ϕ	36.9	11.1	3.7	0.79
	SUM	57.8	15.6	4.6	0.90
BETHE HEITLER	$\pi^0 \to \gamma\gamma$	34.7	7.17	1.57	0.23
	$\eta(\eta') \to \gamma\gamma$	5.3	1.21	0.33	0.05
	$\omega \to \pi^0,\gamma$	0.9	0.20	0.05	0.007
	$\eta' \to \rho^0,\omega,\gamma$	0.3	0.03	0.004	0.000
	SUM	41.1	8.60	1.95	0.29
TOTAL		384.3	94.8	25.8	4.83
CONVENTIONAL μ-FLUX [$\mu/10^7$ prot]					
40% PS 40% Vector	non-strange	162.0	27.8	6.29	1.20
	strange	96.2	14.5	3.08	0.45
	SUM	258.2	42.3	9.37	1.65
20% L = 1	non-strange	55.5	9.8	2.06	0.29
	strange	26.9	4.5	0.87	0.12
	SUM	82.4	14.28	2.93	0.41
TOTAL		340.6	56.6	12.3	2.06

are safe errors on η, η' production. For the production of pions the program gives, because of the equal yield of u($\bar{u}$) and d($\bar{d}$) quarks:

$$N(\pi^0) = (N(\pi^+) + N(\pi^-))/2 \qquad (68)$$

where no additional suppression is expected as in the case of η and η' because of the almost equal mass of $\pi^{\pm}$ and π^0. Equation (68) is in agreement with data [58]. Application of the uncertainties mentioned above on the rates given in table 17 yields the errors given in table 18 .

VECTOR MESON PRODUCTION

40% of all quark anti-quark pairs are classified as vector meson. In case of only one s-(anti)quark there is again no ambiguity. For $u\bar{u}$, $d\bar{d}$ pairs

$$N(\omega) = N(\rho^0)$$

was taken and $s\bar{s}$-pairs were classified as ϕ only. Since the masses of ρ (0.770 GeV/c^2) and ω (0.783 GeV/c^2) are almost equal and the mass of ϕ (1.020 GeV/c^2) is clearly higher it was assumed that $\omega = (|u\bar{u}> + i|d\bar{d}>)/\sqrt{2}$ and ϕ is pure $s\bar{s}$. As in the case of pseudo-scalars the program yields:

$$N(\rho^0) = (N(\rho^+) + N(\rho^-))/2$$

see [59].

RATIO (VECTOR MESON)/(PSEUDO-SCALAR MESON)

It was assumed that:

$$N(\text{vector}) : N(\text{pseudo-scalar}) = 1 : 1$$

From simple quantum statistics one would expect a ratio proportional to $2J+1$, where J = angular momentum quantum number, but the production of vector mesons is suppressed, probably because of their higher mass [64]. From data given in [59] it follows that an error of 50% on the equal ratio of V/PS is a safe limit. The production Monte Carlo was re-runned with a ratio V/PS = 1.5 and renormalized to the measured conventional μ-flux. The difference in prompt μ-flux is given as an error in table 18 .

OTHER ERROR SOURCES

As discussed in 5.3.3 and appendix A, 20% of all quark anti-quark pairs were classified as mesons with $L > 0$. The prompt μ-flux was also generated with 10% and 30% $L > 0$ meson production. The difference is given as error in table 18 as "+ 50% $L = 1$".
In the chain-fragmentation process strange quark anti-quark pairs are created with a probability of 18.4%. In appendix A it is explained that the error on this probability is 10%. The effect of this uncertainty is given in table 18.
The errors taken into account for the branching ratios of the resonances decaying into di-muons are given in table 15 and the effect on the prompt μ-flux is given in table 18 .

5.3.5 COMPARISON OF MEASURED AND SIMULATED PROMPT MUON FLUX

Now that an estimate has been made of the prompt μ-flux caused by conventional processes, one can see how much space there is for other sources by subtracting the flux given in table 17 from the measured prompt μ-flux, given in table 37 of appendix B. As is described in 5.1.1, part of the extrapolated prompt μ-flux is caused by conventional μ-flux leaking out of the first meter of copper of the target and has to be subtracted. To this end table 11 is used. An error on the simulated prompt μ-flux not yet treated in 5.3.4. is the normalization error caused by the limited precision of the μ-flux measurements. The hadron production M.C. was normalized such that it yielded the measured conventional μ-flux. A change in the measured μ-flux will change the hadron production and thus change also the simulated prompt flux. This means that, since the error on the extrapolated conventional and prompt flux are positively correlated, the error on prompt extrapolated and

Table 18: Systematic errors on prompt μ-flux.

	PIT2	PIT3	PIT4	PIT5
μ-flux [$\mu/10^7$prot.]	384.3	94.8	25.8	4.83
15% η	4.1%	3.3%	2.6%	1.7%
20% η'	1.8%	2.1%	2.5%	2.9%
20% VECTOR	4.6%	5.5%	13.0%	19.5%
50% L = 1	−4.8%	−4.7%	−2.9%	−0.2%
10% s-quark	−4.2%	−3.9%	−3.8%	−3.5%
branching ratios	5.3%	5.2%	5.3%	6.5%
TOTAL ERROR	10.5%	10.5%	15.3%	21.0%

prompt generated flux are also positively correlated. This was taken into account in deriving the results of table 19 , where the difference of the measured prompt μ-flux and the above described M.C. – generated prompt μ-flux is given. The error on the leakage correction is also included in table 19 .

Table 19: Difference between measured and generated prompt μ-flux.

flux in $\mu/10^7$ protons on target				
	PIT2	PIT3	PIT4	PIT5
prompt generated	384±40	94.8±10.0	25.8±4.0	4.8±1.0
prompt extrapolated	476±13	110±17	28.7±1.1	5.5±0.3
leakage	19.8±2.0	2.5±0.4	0.5±0.2	0.07±0.03
difference	72±42	12.7±11.1	2.4±4.1	0.6±1.1

A non-zero difference could for instance be due to the semi-leptonic decay of charmed hadrons produced in the dump, as will be discussed in section 6.2.2 .

6. SIMULATION OF PROMPT LEPTONS FROM CHARM DECAY

A source of prompt leptons is the semi-leptonic decay of charmed hadrons, in which the charm quark decays weakly into a strange quark, a charged lepton and a neutrino:

$$c \rightarrow s\ l\ \nu_l$$

The lifetime of the lightest charmed hadrons is small enough ($< 10^{-12}$ sec) to cause a prompt signal, i.e. independent of target density. The centre of mass energy in 400 GeV p-Cu interactions ($\sqrt{s} = 27$ GeV) is high enough to produce the lightest charmed mesons like D and D_s and baryons like Λ_c. Purely leptonic decay of the lightest charmed hadrons is expected to be small (see section 2.4.1). Production of heavy flavours others than charm is negligible because of the insufficient centre of mass energy.
There exist several models for the production of charmed hadrons (see section 2.3), differing in longitudinal and transverse momentum distributions and cross-sections. The energy and A-dependence of the cross-sections are not very well established [74].
In order to study charm production a simulation by Monte Carlo was made and the parameters were adjusted to fit the data.

6.1 THE MONTE CARLO SIMULATION

For the Feynman-x (x_F) dependence of the cross-section the simple formula

$$\partial\sigma/\partial x_F \propto (1-x_F)^n \tag{69}$$

was used, suggested by quark counting rules at higher values of x_F (see section 2.3 and [80]). In the literature also the Lorentz invariant cross-section is used and parametrized as:

$$E\partial\sigma/\partial x_F \propto (1-x_F)^n \tag{70}$$

For comparison with other experiments the results will be given for both parametrizations.

ACCEPTANCE

For the angle Θ between the hadron and the neutrino created in the decay of that hadron one can write:

$$\Theta_{lab} = \arctan\{\sin\Theta_{cm}/(\gamma\cos\Theta_{cm}+\beta\gamma)\}$$

Therefore Θ is independent of the neutrino momentum in the rest frame of the hadron, and, since γ and β are determined by the velocity of the hadron and since the angle of acceptance of the CHARM detector for neutrinos produced in the target is known (2.78 mrad), the angular acceptance for neutrinos from hadron decays depends in first approximation only on x_F of the hadron. The relative probability for finding an event in the detector as function of x_F of the D-meson is given in fig.36, where an isotropic angular distribution for the neutrino in the D rest frame was assumed.
In the same figure also the cross-section parametrized according to equation (69) with $n=6$ is shown. From the product of the two curves one can see that for $n=6$ the mean accepted x_F is 0.33.
For the transverse momentum distribution of the charmed hadrons

$$\partial\sigma/\partial p_T \propto p_T e^{-bp_T} \tag{71}$$

was used, with mean value $\langle p_T \rangle = 2/b$.
From [75] (350GeV p-Fe)

$$b = (2.0 \pm 0.3)\ (\mathrm{GeV/c})^{-1}$$

was taken, which gives

$$\langle p_T \rangle = (1.0+0.18-0.13)\ \mathrm{GeV/c} \tag{72}$$

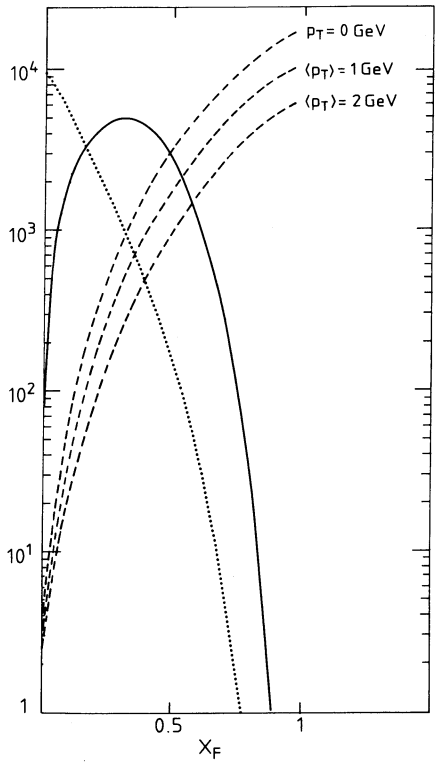

Figure 36: Dashed curves: acceptance for neutrinos from D- decay as a function of Feynman-x of the D for mean transverse momenta of 0, 1 and 2 GeV/c (dashed curves). Dotted curve: $(1-x_F)^6$ Full curve: product of dotted-curve with acceptance of mean p_T equals 1 GeV/c. The vertical scale is in arbitrary units.

Fig.36 also shows the acceptance for $p_T = 0$ and $< p_T > = 2$ GeV/c, where equation (71) is used. The influence of the p_T-parameter b on the shape of the neutrino spectrum is negligible and it is small (7%) on the cross-section, as can be seen from fig.36 and (72).
Since the acceptance is not very sensitive to p_T, no other form of parametrization has been tried; $b = 2$ was used for all fits and an error contribution of $\pm 7\%$ to the charm cross-section was calculated.
The alignment of the beam was better than 0.025 mrad and therefore does not affect the results.

CASCADE CONTRIBUTION

There was a contribution of charmed particles produced by secondaries in the hadronic cascade of the 400 GeV p-Cu interactions. This contribution is expected to be small because:

1. The angular acceptance decreases rapidly when going down in energy (see fig.36). E.g. at 200 GeV the acceptance is 0.15 times the acceptance at 400 GeV.

2. The cross-section decreases rapidly when going down in energy. A parametrization from Odorico [90] was used. At 200 GeV [90] predicts a cross-section 0.27 times the one at 400 GeV (see fig.8). The difference among the current charm production models on the prediction of this number is of the order of 20% (see section 2.3).

3. The neutrino cross-section is proportional with energy.

The cascade contribution was simulated using the secondaries generated with the M.C. described in appendix A. In case of a meson parent $n=2$ in (70) was used according to Ritchie et al. [76] (350 GeV π-Fe), in case of a baryon parent the same n as for the primary interaction was taken. In addition it was assumed that the average semileptonic branching ratio for the cascade particles was the same as for the ones produced by the primary protons. The cascade contribution in the M.C. was typically 15% of the total charm production.

FERMI MOTION

The Fermi motion of the target nuclei was taken into account by giving them an isotropically distributed momentum between 0 and 300 MeV/c:

$$\rho(p_f) \propto p_f^2$$

according to the Monte Carlo program of Ranft (see appendix A).
The effect of the Fermi motion on the final result is small compared to the total error.

DECAY KINEMATICS

For the energy spectrum of the neutrino in the rest frame of the decaying hadron the spectator model from Altarelli et al. [84] was used (see section 2.4.2). The parameters of the model were adjusted to the charged lepton spectrum in semi-leptonic D-decay (fig.13) as measured by the DELCO-collaboration [78]. The prediction of the model for the ν-spectrum was used. Assuming β-decay of the charm quark of purely $V-A$ character, an error of 4% in the mean neutrino energy was estimated from the uncertainties in the DELCO-data.

6.2 COMPARISON WITH DATA

6.2.1 PROMPT NEUTRINO FLUX

The simulated prompt neutrino-spectrum was compared with the prompt ν_e-CC spectrum obtained from the $(0\mu)-0.33\cdot(1\mu)$ data sample of the density one target, given in table 50 of appendix G. The conventional background generated with M.C. was subtracted (see section 5.2 table 13) and the energy cut was 20 GeV. Since the conventional background of ν_e is small (see fig.38), subtraction instead of extrapolation has been applied to eliminate this background. In fig.35 one can see that the M.C.-simulation can describe the conventional muon neutrino flux within an uncertainty of $\pm 10\%$. Most conventional electron neutrinos come from Ke_3-decays. The kaon contribution to the conventional muon neutrinos is indicated in fig.35. A 20% error in the background of conventional electron neutrinos was assumed.
The unfolding of the $(0\mu)-0.33\cdot(1\mu)$ spectrum to CC ν_e (see section 4.6.1) has little influence on the shape of the spectrum (see fig.37) and the total event rate depends only on the ratio neutrino/anti-neutrino for which 0.5 $\pm$ 0.1 was taken (see [81]).
A combined fit of D and Λ_c production was applied. For Λ_c decay the same ν-spectrum in the rest frame of the parent was used as for D decay. Eventually produced Σ_cs will have a similar decay spectrum as Λ_cs and are thus included in the Λ_c cross-section. Λ_c is produced with $n=1$ in (69) (see Gunion [80]). For $D\bar{D}$ production the n-parameter of equation (69) was left free, because theoretical predictions are not accurate (see section 2.3). The results of this 3 parameter fit are:

$$(\sigma \cdot BR)_{D\bar{D}} = 116+26-23(\text{stat.})\pm 14(\text{syst.})\ \mu\text{b/nucleus} \quad \text{for } A=63.5$$

For the exponent in the factor $(1-x)^n$ one gets:

$$n_{(D\bar{D})} = 7.1+1.4-1.2(\text{stat.})\pm 0.5(\text{syst.})$$

and for the production of Λ_c relative to D:

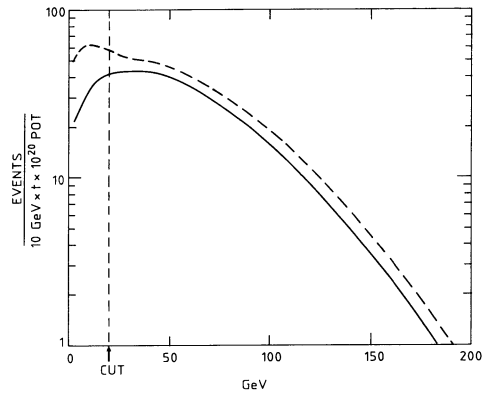

Figure 37: Charged-current electron-neutrino spectrum as a function of neutrino energy (full curve) derived from the $(0\mu) - 0.33 \cdot (1\mu)$ spectrum as a function of shower energy (dashed curve). Both spectra are Monte Carlo simulations.

$$\sigma(\Lambda_c\bar{D}) \cdot BR / \sigma(D\bar{D}) \cdot BR < 0.045 \text{ at } 90\ \% \text{ C.L.} \quad \text{for } A = 63.5 \tag{73}$$

The χ^2 of the fit was 11.2 for 10 degrees of freedom. The systematic errors are given in table 20.

Table 20: Errors in $(1 - x_F)$ exponent (n) and cross-section (σ) for $D\bar{D}$-model.

	n	σ
conventional background	4%	8%
$< E_\nu >$ in D rest frame	5%	
$< P_t >$ of D		7%.
ν cross-section		5%
event statistics		4%
TOTAL ERROR	6.4%	12.4%

The fit was made for $E_\nu > 20$ GeV. No significant changes were seen with energy cuts ranging from 10 to 40 GeV in neutrino energy. Also other experiments [75] [82] have shown that $\sigma \cdot BR$ for Λ_c is small compared to $\sigma \cdot BR$ for D-mesons. From [82] it follows that Λ_c and $\bar{\Lambda}_c$ are produced with equal probability and with n bigger than 1, which means that the limit (73) is conservative.
If forward Λ_c production is neglected completely the results become:

$$(\sigma \cdot BR)_{D\bar{D}} = 105 + 15 - 19(\text{stat.}) \pm 13(\text{syst.})\ \mu\text{b/nucleus} \quad \text{for } A = 63.5 \tag{74}$$

$$n_{D\bar{D}} = 6.2 + 0.4 - 0.5(\text{stat.}) \pm 0.4(\text{syst.})$$

For the two-parameter fit the error on n is much smaller. The χ^2 of the fit was 11.8 for 11 degrees of freedom. This result is shown in fig.38, together with the $n = 1$ curve and the conventional background that was subtracted.
A mean value of $x_F = 0.33$ was found for accepted events with $n = 6.2$. (For $n = 5$ and $n = 7$ the mean value of x_F was 0.37 and 0.31 resp.)
If the Lorentz invariant cross-section (equation (70)) is used one gets:

$$(\sigma \cdot BR)_{D\bar{D}} = 122 \pm 15(\text{stat.}) \pm 15(\text{syst.})\ \mu\text{b/nucleus} \quad \text{for } A = 63.5 \tag{75}$$

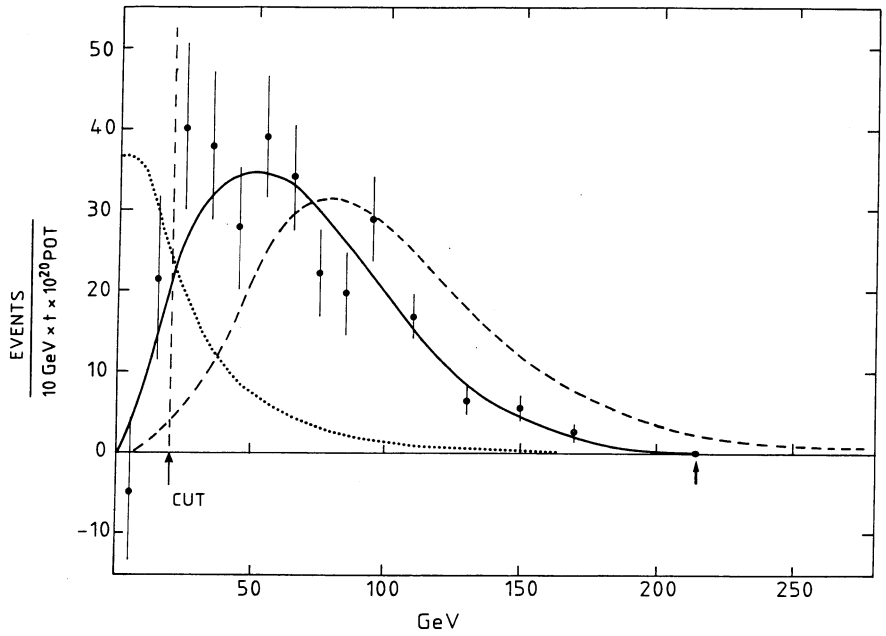

Figure 38: The data points give the prompt CC ν_e spectrum. Full curve is the M.C.-spectrum for n = 6.2 in (69), best fit. Dotted curve is the subtracted conventional background. Dashed curve is the M.C.-spectrum for n = 1 in (69), normalized to # of events.

$$n_{D\overline{D}} = 4.8 + 0.2 - 0.3(\text{stat.}) \pm 0.3(\text{syst.})$$

with $\chi^2 = 10.0$ for 11 degrees of freedom. These values will be compared with results from other experiments in section 10.2 .

6.2.2 PROMPT MUON FLUX FROM SEMI-LEPTONIC CHARM DECAY

Parametrization (70), which gave the lowest χ^2, has been used to generate the energy spectrum of the charmed hadrons. The μ-spectrum in the rest frame of the decaying hadron is taken from Altarelli et al. [84], (section 2.4.2). The tracking of the muons through the iron muon shield is described in appendix B. The muon flux thus generated is given in table 21 for the different gaps in the shield as a function of the $(1-x_F)$ exponent. The numbers in table 21 have to be multiplied with the cross-section times branching ratio of charmed hadron production to obtain the μ-rate in the pits. The p_T – parameter in (71) was set to b = 2, variation of ± 1 gave a negligible change in the muon flux. The cascade contribution is small, as can be seen from this table.

Table 21: Prompt muon contribution from charmed hadrons.

	muons/10^7proton/(μb · branching ratio)			
$(1-x_F)$ exponent	PIT2	PIT3	PIT4	PIT5
n = 1	2.2	0.57	0.12	0.016
n = 4	1.1	0.17	0.025	0.0021
n = 5	0.87	0.11	0.013	0.0009
n = 6	0.70	0.08	0.008	0.0004
cascade contribution	16%	12%	9%	6%

From the prompt charged current electron neutrino event rate of table 50 the cross-section times branching ratio and the $(1-x_F)$ exponent of D-meson production have been determined in the previous section (75). This result can be used to predict the prompt muon flux due to D-mesons, if an equal electron and muon semi-leptonic branching ratio for the D-meson is assumed. The result is shown in table 22 and fits reasonably with the expected value of table 19 , where it was already anticipated that the difference between the generated and measured prompt muon flux could be attributed to charm decays.
Thus no evidence for an excess of prompt μ-pairs at low energies, as measured by [52], could be found down to x_F-values of 0.1 . The prompt muon flux in pit 1 was left out of the analysis, because of the dominating conventional background in pit 1 (see table 37).
The creation of Drell-Yan muon pairs has been neglected.

Table 22: Muon flux predicted by D-meson model and CC ν_e-event rate.

$\mu/10^7$ proton
pit2: 112 ± 21
pit3: 14.6 ± 3.5
pit4: 1.8 ± 0.6
pit5: 0.13 ± 0.05

7. COMPARISON OF PROMPT ELECTRON NEUTRINO AND MUON NEUTRINO EVENT RATES

As explained in section 2.4.1. one expects an equal flux of prompt electron neutrinos and muon neutrinos from the decay of charmed mesons. An eventual asymmetry between ν_e and ν_μ, which would be an indication of non-standard physics, is best expressed like:

$$A = (\nu_\mu - \nu_e)/(\nu_\mu + \nu_e) \tag{76}$$

Often the ratio $R = \nu_e/\nu_\mu$ is used, which has the disadvantage of having a non-Gaussian error distribution, if the error in the denominator gets large. For comparison with other experiments both values will be given. The standard expectation is $A = 0$ and $R = 1$.

The prompt charged current muon neutrino events, obtained by extrapolation to infinite target density are given in table 7.
Because the conventional background for electron neutrinos is much smaller than for muon neutrinos (17% vs 68% for $\rho = 1$ target and $E_\nu > 20$GeV), the error in the prompt charged current electron neutrino rate is smaller if the correction for this background is performed by subtraction rather than extrapolation, even though the conventional background simulated by Monte Carlo has a large systematic error. Thus, for the prompt CC ν_e-rates the subtracted value of table 7 is used. The values for asymmetry and ratio are given in table 23 for neutrino energies > 2 GeV, > 20 GeV and > 80 GeV. Systematic error sources are listed in section 4.8 , error propagation was done by a Monte Carlo program, which took into account all correlations between the different errors.

In table 23 also the result is given for the case where for ν_μ the conventional background generated by Monte Carlo was subtracted from the density one rate. The systematic error is now much larger, but the statistical error is reduced considerably.
The values of table 23 indicate an approximate two σ deviation from the expected value of $A = 0$.

Table 23: Asymmetry and ratio using unfolded CC prompt spectra.

The asymmetry is defined as $((1\mu)-(1e))/((1\mu)+(1e))$ and the ratio as $(1e)/(1\mu)$ muon neutrinos extrapolated, electron neutrinos subtracted			
	$E_\nu \geq 2$ GeV	$E_\nu \geq 20$ GeV	$E_\nu \geq 80$ GeV
Asymmetry	$0.09 \pm 0.17 \pm 0.08$	$0.21 \pm 0.09 \pm 0.04$	$0.21 \pm 0.12 \pm 0.03$
Ratio	$0.84\ ^{+0.34+0.15}_{-0.25-0.13}$	$0.66\ ^{+0.13+0.06}_{-0.11-0.06}$	$0.66\ ^{+0.18+0.04}_{-0.15-0.04}$
muon neutrinos subtracted, electron neutrinos subtracted			
	$E_\nu \geq 2$ GeV	$E_\nu \geq 20$ GeV	$E_\nu \geq 80$ GeV
Asymmetry	$0.25 \pm 0.06 \pm 0.14$	$0.24 \pm 0.05 \pm 0.08$	$0.18 \pm 0.08 \pm 0.10$
Ratio	$0.61\ ^{+0.08+0.20}_{-0.07-0.16}$	$0.61\ ^{+0.07+0.12}_{-0.06-0.10}$	$0.70\ ^{+0.12+0.15}_{-0.11-0.13}$

Part of the error in the values of table 23 are due to the unfolding procedure, which corrects for detector acceptance and energy resolution, as described in 4.5.6 .
Especially in the case of muon neutrinos the unfolding error is big because of the large statistical errors in the prompt rate, due to the dominating conventional background. So far no pre-knowledge of the shape of the prompt spectrum has been used (except $\Phi(\nu_e)/\Phi(\bar{\nu}_e) = 1$ in the unfolding of $(0\mu) - 0.33 \cdot (1\mu)$ to CC ν_e).

7.1 ALTERNATIVE ACCEPTANCE CORRECTION

In chapter 6 it was found that the electron-spectrum could be well described by the assumption of D-production with an x_F-dependence like $(1-x_F)^{4.8 \pm 0,4}$ and subsequent semi-leptonic decay.
Also other experiments find that this model fits their data (see section 10.2). In the following section an analysis will be described, in which this model is used as an assumption in the acceptance calculation.

From the acceptance curves in fig.36 one can see that any reasonable charm production spectrum will give, in the case of 400 GeV p-N interactions, a neutrino spectrum with practically no events below 20 GeV, a broad maximum between 40 and 90 GeV and a continuous decrease towards higher energies.
Important error sources, introduced by the unfolding, concerning the difference between ν_μ and ν_e rates, are the energy resolution of the detector, the correction for unrecognized muons and the correction for fake (1μ)-events by π/K-decay. The energy resolution improves rapidly with energy (see 3.4.8.). The correction for unrecognized muons is only large at low energies, the correction for π/K-decay is almost constant above 20 GeV, see sections 4.5.2, 4.5.3, fig.33 and 34. Looking at the spectrum predicted by semi-leptonic D-decay (fig.38), one sees that the contribution at low energies is very small, thus the a priori assumption of the D-spectrum reduces the above mentioned errors.

Since the energy resolutions at low energies for (1e) and (1μ) events are of the same order of magnitude, the π/K-decay correction negligible but the unrecognized muon correction large, this method will underestimate the (1μ)-rate when there are events at low energies, in contradiction with the D-spectrum. Thus it will give a lower limit for the $(\mu - e)/(\mu + e)$ asymmetry in case of low energy cuts and the same result for energy cuts $> \approx$ 20 GeV.

In this section an energy spectrum for neutrino events caused by semi-leptonic D-meson decay will be assumed for the calculation of the detector acceptance, with the Ds produced according to (70) and (71) of section 6.1. (see fig.38), to check the for this model predicted vanishing e-μ asymmetry.
A central value of 5 will be used for the $(1-x_F)$ exponent, with a variation of ± 1 in the calculation of the systematic error.
The same energy spectrum for electron neutrinos and muon neutrinos is used with an equal flux ratio of neutrinos and anti-neutrinos. This energy spectrum was smeared with the energy response and resolution for hadrons, electrons and muons to get the correction factors (generated events)/(observed events) for the different event types and energy cuts. In case of the $(0\mu) - 0.33 \cdot (1\mu)$ event sample the ratio (generated CC events)/(observed events) was determined, assuming the same NC/CC-ratio and y-distributions for ν_e- and ν_μ-events. The observed event rates were multiplied with the acceptance factors to obtain the event rates for an ideal detector with infinitely small energy resolutions.
The above described procedure is the method also applied by other experiments ([33], [34], [35]). The main difference with the method described in section 4.5.6. is the acceptance calculation for CC-ν_μ. Since the conventional background is removed by extrapolation, no care is taken here for its acceptance, with as result a reduction in systematic error.

To generate the correct hadronic energy, electron energy and muon energy fraction of the total neutrino energy, with the propper angular distributions of the muon and electron momenta for charged current neutrino and anti-neutrino events, the same Monte Carlo program was used as for the unfolding, described in section 4.5.6.; x- and y-distributions for muon and electron neutrinos are taken to be the same and are given in [72].
Also the same parametrization for detector response and resolution of hadron, electron and muon energy as for the unfolding were used.

The corrections applied for hadrons leaking out of the density 1/3 target, cosmic ray background, unrecognized muons, faked (1μ) by decay of π/K were already given in table 12, table 5, fig.33 and fig.34, respectively. For the correction for material upstream of the dump the leakage factor α in equation (66) was increased by 0.6%, as described in section 4.7 .
As before, for muon neutrinos the prompt signal was obtained by extrapolation, for the electron neutrinos the conventional background, generated by Monte Carlo, was subtracted.

In fig.39 the generated (CC + NC) ν_e spectrum (prompt + conventional) is shown, together with the measured $(0\mu) - 0.33 \cdot (1\mu)$ spectrum. Also the conventional (CC + NC) background is indicated in fig.39.

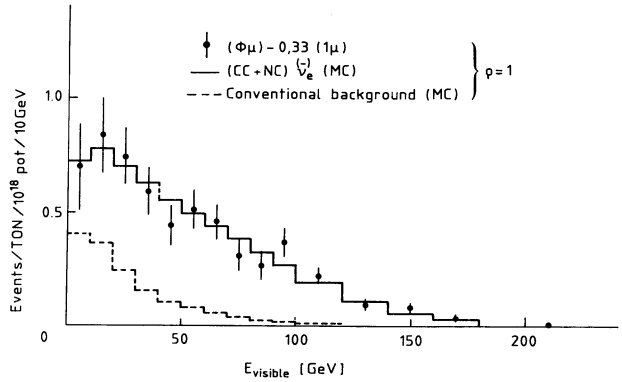

Figure 39: Events not coming from CC or NC ν_μ interactions, recorded with the $\rho = 1$ target. The histogram gives the prediction of the $D\bar{D}$-production model with $(1 - x_F)$ exponent of five plus the conventional background, calculated by MC and indicated separately.

In fig.40 the CC muon neutrino events, generated according to the new acceptance correction, are shown together with the prompt data (from extrapolation). Also the input CC ν_μ spectrum is given.

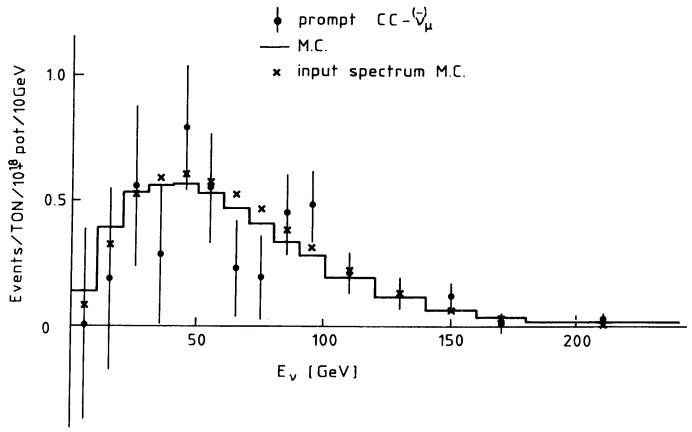

Figure 40: Prompt charged current muon neutrino spectra. The points with error bar give the measured data from extrapolation. The histogram gives the prediction of the $D\bar{D}$-production model with $(1 - x_F)$ exponent of five. The crosses give the input spectrum of the Monte Carlo.

The observed energy spectrum is softer than the input spectrum mainly because of muons for which the momentum fit failed. These muons got only the energy determined by their range in the detector. The fraction of unfitted muons at E > 2 GeV was (19 ± 6) % for the extrapolated data, the Monte Carlo simulation predicted 15.4 % . The acceptance for CC ν_μ-events was 0.97 for E > 2 GeV, 0.94 for E > 20 GeV and 0.97 for E > 80 GeV. The increase in acceptance at 80 GeV is caused by the fact that a fit is made to $1/p_\mu$, which shifts the average of p_μ to higher values for large muon momenta and the negative slope of the spectrum at that energy, which compensates for the loss of events due to unfitted muons.

The prompt charged current rates for ν_μ and ν_e, determined with the alternative acceptance calculation, are given in table 24. For $E_\nu > 20$ GeV the result is the same as for the model-independent unfolding given in table 7. For muon neutrinos there is a difference below 20 GeV where the corrections are big and above 80 GeV where the statistics get poor, though within the errors due to unfolding.
Also the asymmetry is given in table 24. The systematic errors are given in table 25.

Table 24: Rates, asymmetry and ratio from alternative acceptance method.

prompt charged current ν_μ and ν_e rates in evts/ton/10^{18}prot.			
	$E_\nu \geq 2$ GeV	$E_\nu \geq 20$ GeV	$E_\nu \geq 80$ GeV
CC ν_μ	$4.92 \pm 0.86 \pm 0.35$	$4.86 \pm 0.71 \pm 0.21$	$2.07 \pm 0.35 \pm 0.07$
CC ν_e	$3.42 \pm 0.28 \pm 0.26$	$3.16 \pm 0.22 \pm 0.14$	$1.19 \pm 0.11 \pm 0.04$
Asymmetry and Ratio The asymmetry is defined as $((1\mu)-(1e))/((1\mu)+(1e))$ and the ratio as $(1e)/(1\mu)$			
	$E_\nu \geq 2$ GeV	$E_\nu \geq 20$ GeV	$E_\nu \geq 80$ GeV
Asymmetry	$0.18 \pm 0.10 \pm 0.05$	$0.21 \pm 0.08 \pm 0.03$	$0.27 \pm 0.09 \pm 0.01$
Ratio	$0.70\ ^{+0.16+0.07}_{-0.14-0.07}$	$0.65\ ^{+0.12+0.04}_{-0.10-0.03}$	$0.57\ ^{+0.12+0.01}_{-0.11-0.02}$

Table 25: Systematic errors in alternative acceptance method for $E_\nu > 20$ GeV.

errors in %			
source	prompt CC ν_μ rate	prompt CC ν_e rate	asymmetry $(\mu-e)/(\mu+e)$
unrecognized muons	0.4	1.6	4.5
pi/K-decay in shower	0.4	2.5	6.7
M.C.-parameters*	0.8	1.0	0.5
proton accounting	3.7	1.6	4.6
density $\pm 0.5\%$	1.9		4.2
leakage + upstr.mat.	0.9		1.9
conv.backgr.		2.8	6.2
cosm.backgr.$(0\mu)\%$		0.05	0.1
ratio NC/CC		0.9	1.9
TOTAL	4.3	4.6	12.3

* $(1-x)$ exponent 5 ± 1, energy response of the detector, muon momentum resolution and muon fit probability

One sees that the significance of the asymmetry between electron and muon neutrinos has slightly increased because of the assumption of the $D\bar{D}$-model. In fig.42 the difference between prompt muon neutrino and electron neutrino event rate is shown, the error bars represent only the statistical error. In this figure the conventional muon neutrino background is indicated, with integral equal to the difference between ν_μ and ν_e rate above 20 GeV. Conclusions are given in section 10.1.3 .

At the end of section 6.2.2. a comparison was made between the neutrino and muon flux caused by semi-leptonic decay of charmed hadrons. Using the prompt CC muon neutrino event rate above 20 GeV in the CHARM detector, given in table 24, instead of the prompt CC electron neutrino rate to determine the charm cross-section and assuming an $(1-x_F)$ exponent of five, one would find:

$$(\sigma \cdot BR)_{D\bar{D}} = 188 \pm 36 \ \mu\text{barn/nucleus} \quad \text{for } A = 63.5 \tag{77}$$

This cross-section is higher than measured in other experiments (see section 10.2).
If one uses equation (77) to calculate the muon flux from semi-leptonic D-decay for $n = 5$ with the help of table 21 one finds the values given in table 26.

Table 26: Muon flux predicted by D-meson model and CC ν_μ-event rate.

$\mu/10^7$ proton
pit2: 172 ± 35
pit3: 22.6 ± 5.6
pit4: 2.8 ± 0.9
pit5: 0.21 ± 0.09

The agreement of the results of table 26 with the predicted muon flux, given in table 19, are less good than in the case that cross-section (75) was used, see table 22. In pit 2 cross-section (77) would give a 1.8 σ deviation from the predicted value. For conclusions see section 10.1 .

8. SEARCH FOR TAU NEUTRINOS

A search for tau-neutrino induced events has been performed using the reaction:

$$\nu_\tau + N \rightarrow \tau + X \quad \hookrightarrow \nu_\tau + \bar{\nu}_\mu + \mu \tag{78}$$

This reaction would give (1μ)-events with unbalanced transverse momentum (p_T), since the two neutrinos cannot be seen [42].
The angular resolution for hadronic showers of the CHARM detector is not good enough to recognize missing transverse momentum on an event by event basis, so the search was limited to events with X = π + "recoil of N" in (78) and where the pion left a clearly visible track before reinteraction.
The p_T-unbalance was defined as:

$$|\Delta p_T| = |p_T(\mu) - p_T(\pi)|$$

A $\Delta p_T \neq 0$ could be caused by the unseen recoil of the nucleon or by Fermi-motion. This background was estimated by applying the search algorithm to wide-band beam (WBB) data, in which the relative ν_τ-flux is expected to be lower by a factor $\approx 10^3$.

The selection criteria for the ν_τ – candidates were:

1. Hadronic energy $\leq$ 6 GeV
2. The ionization deposited in the first four planes $\leq$ 20 MIPS
3. Two tracks traversing at least 10 planes without interaction should be present
4. After passing through 10 planes one track should show visible interaction at the end point ($\geq$ 3 MIPS)
5. $|\Delta p_T| > 0.6$ GeV/c and $\sigma(p_T) < 30$ %

Out of 2600 (1μ)-events with hadronic energy < 6 GeV from $\rho = 1$ and $\rho = 1/3$ data, four candidates were found, three with $\mu^+\pi$ and one with $\mu^-\pi$.
From the WBB data a background was estimated of 5.2 ± 2.5 events. Thus no significant ν_τ-signal was found.

The above described method has an efficiency of less than $\approx$ 1% of all ν_τ-events. An indirect way to determine interactions of ν_τs, unknown other neutrinos or neutral penetrating particles is to compare the (0μ)-sample with the charged current electron neutrino events, found by direct recognition of an electromagnetic shower inside a hadronic shower (see section 4.6.2).

For the amount of (0μ)-events not caused by NC ν_μ-interactions or NC + CC ν_e-interactions, here called $N(\nu_X)$, one has:

$$N(\nu_X) = N(0\mu) - \langle R \rangle \cdot N(1\mu) - (1 + \alpha R^e) \cdot N(1e) \tag{79}$$

where $R^e = 0.340$ is the ratio NC to CC interactions for the assumption of equal fluxes of neutrinos and anti-neutrinos [73] and α is the ratio $N[(1e), E_{hadron} > 2GeV]/N[(1e), E_{shower} > 2GeV]$. This last factor was found to be 0.865 ± 0.025 by Monte Carlo calculation [51]. It is further assumed here that interactions of the type $\nu_X \rightarrow \mu + X, e + X$ will not end up in the (1μ) or (1e) sample.
Using the events with $E_{shower} > 2$ GeV from both target densities (tables 6, 47) the rate for ν_X was found to be

$$R(\nu_X) = 27 \pm 84 \text{ events/ton}/10^{20}\text{protons}$$

which means that $R(\nu_X) < 12\%$ of the total prompt (1μ) + (0μ) event rate or < 21% of the prompt (0μ) event rate with shower energy larger than 2 GeV at 90% C.L. .

In translating the limit on ν_x to ν_τ one has to take into account that a part of the CC ν_τ-events looks like (1e)- or (1μ)-events, because of the decay $\tau \rightarrow e\bar{\nu}\nu, \mu\bar{\nu}\nu$ with a branching ratio of 17.5 % per channel.
In addition, the CC ν_τ reactions are suppressed relative to the CC ν_e and ν_μ reactions because of the high mass of the tau. A suppression factor $CC(\nu_\tau)/CC(\nu_e,\nu_\mu) = 0.8$ was used, derived by Monte Carlo, assuming D_s production according to equation (70) of section 6.1. with an $(1-x)$ exponent of 3 and decay of $D_s \rightarrow \nu_\tau + \tau$, $\tau \rightarrow \nu_\tau + X$.
Assuming all events of the channel $\tau \rightarrow e,\mu + X$ were classified as (1μ) or (1e) the amount of charged current tau neutrino events with $E_\nu > 2$ GeV becomes:

$$N(CC)_{\nu_\tau} = 28 \pm 87 \text{ evts/ton/}10^{20}\text{pot}$$

and the ν_τ flux:

$$\Phi(\nu_\tau + \bar{\nu}_\tau) < 21\ \% \text{ (90\% C.L.) of the total prompt flux above 2GeV}$$

8.1 TEST OF ELECTRON-MUON UNIVERSALITY

Equation (79) can be used for comparing the weak neutral coupling strength to the electron and muon. The Standard Model predicts an equal coupling of $W^\pm$ and Z^0 to e, μ and τ [49].
From precise measurements of the ratio of the decays $\pi \rightarrow e\,\nu_e$ and $\pi \rightarrow \mu\,\nu_\mu$ [43] one has found

$$g_{e\nu_e}/g_{\mu\nu_\mu} = 0.9939 \pm 0.0057$$

From measurements of muon neutrino scattering on electrons [45], [46] and from the forward-backward asymmetry in the reaction $e^+e^- \rightarrow \mu^+\mu^-$ [47] the relative coupling strength of the electron and the muon to the weak neutral current have been derived, with

$$g_{ee}/g_{\mu\mu} = 0.96 \pm 0.11$$

A value for the relative coupling strength of ν_e and ν_μ to the weak neutral current can be obtained using:

$$g_{\nu_e\bar{\nu}_e}/g_{\nu_\mu\bar{\nu}_\mu} = (R^e/R^\mu)^{1/2} \qquad (80)$$

where

$$R^e = \sigma(\nu_e N \rightarrow \nu_e X)/\sigma(\nu_e N \rightarrow eX)$$

and

$$R^\mu = \sigma(\nu_\mu N \rightarrow \nu_\mu X)/\sigma(\nu_\mu N \rightarrow \mu X)$$

and assuming $g_{e\nu_e}/g_{\mu\nu_\mu} = 1$.

The values of R^μ for neutrino and anti-neutrino are taken from [48], see also section 4.6.1. For equal prompt fluxes of neutrinos and anti-neutrinos one gets:

$$R^\mu = 0.34 \pm 0.005\ ,\ E_{shower} > 2 \text{ GeV}.$$

If one sets in equation (79) $N(\nu_x) = 0$, a value for R^e can be derived. Using the events of both target densities with $E_{shower} > 2$ GeV from table 6 and 47 one gets:

$$R^e = 0.406 + 0.145 - 0.135$$

substitution in (80) gives:

$$g_{\nu_e\bar{\nu}_e}/g_{\nu_\mu\bar{\nu}_\mu} = 1.09 + 0.18 - 0.20$$

where it is assumed that only ν_e and ν_μ contribute to the events in the detector.

9. LIMIT ON THE BRANCHING RATIO $\pi^0 \rightarrow \nu\bar{\nu}$

The decay $\pi^0 \rightarrow \nu\bar{\nu}$ is not possible in the Standard Model with only one Higgs doublet and massless neutrinos. For neutrinos of mass around 55 MeV the branching ratio would be $\approx 2.8 \times 10^{-9}$ [65], caused by Z^0-exchange. If more than one Higgs-doublet exists, with coupling constants proportional to some large fermion masses, even for massless neutrinos the branching ratio could be become as high as the present limit of $\Sigma(\pi^0 \rightarrow \nu\bar{\nu}) < 2.4 \cdot 10^{-5}$ [65].

It was tried here to improve this limit by making use of the Monte Carlo calculation of the amount of π^0s in the target. The π^0-yield is strongly correlated with that of $\pi^{\pm}$. One expects for the π^0 rate: $\pi^0 \approx (\pi^+ + \pi^-)/2$ (see appendix A). The neutrinos from $\pi^{\pm}$-decay produced by the Monte Carlo agree within $\approx 10\%$ with the measured conventional neutrino rate (see fig.35).

If the branching ratio of $\pi^0 \rightarrow \nu\bar{\nu}$ is one, a CC ν event rate from M.C. is expected of $(4.3 \pm 0.8) \cdot 10^7$ events/ton/10^{20} prot. with $E_\nu > 2$ GeV and of $(3.8 \pm 0.8) \cdot 10^7$ events/ton/10^{20} prot. with $E_\nu > 20$ GeV. The error is a combination of the uncertainty in conventional neutrino production from $\pi^{\pm}$-decay and the $\pi^0/(\pi^+ + \pi^-)$ ratio of the hadron production model used.

To estimate the neutrino event rate from $\pi^0 \rightarrow \nu\bar{\nu}$, the expected neutrino rates from charm decay, measured by Ritchie et al. [75] in a 350 GeV p-Fe experiment, were subtracted from the prompt neutrino rates calculated in this experiment. The charm cross-section in that experiment was measured by looking at the prompt single muon rate, so it is not sensitive to a contribution from π^0-decay as in the neutrino case. Scaled with 1.20 ± 0.06 for the difference between 350 and 400 GeV and with 1.11 ± 0.03 for the difference in A between iron and copper one expects 324.5 ± 43.9 prompt CC events/ton/10^{20} prot. for $E_\nu > 20$ GeV in the fiducial volume of the CHARM detector from the result of Ritchie et al. (see also chapter 10.2). It was assumed that the branching ratio for semi-leptonic decay of charmed particles to electrons is the same as to muons. Only part of the systematic error in the result of Ritchie et al. caused by the uncertainty in the $(1 - x_F)$ exponent was taken into account, because both experiments have similar acceptances.

Subtracting from the measured prompt rates, table 7, one gets:

$$\pi^0 \rightarrow \nu_e\bar{\nu}_e = -9.6 \pm 51 \text{ CC events/ton/}10^{20} \text{ prot.}$$
$$\pi^0 \rightarrow \nu_\mu\bar{\nu}_\mu = 159 \pm 100 \text{ CC events/ton/}10^{20} \text{ prot.}$$

From these numbers, together with the result for ν_τ from the previous chapter (multiplied by 1/0.8 to correct for the kinematical suppression of CC ν_τ-events, see chapter 8), one gets, with BR($\pi^0 \rightarrow \nu\bar{\nu}$) = (# of events found)/(# of events expected for BR = 1):

$$BR(\pi^0 \rightarrow \nu_e\bar{\nu}_e) = (-.25 \pm 1.34) \cdot 10^{-6}$$
$$BR(\pi^0 \rightarrow \nu_\mu\bar{\nu}_\mu) = (4.18 \pm 2.78) \cdot 10^{-6}$$
$$BR(\pi^0 \rightarrow \nu_\tau\bar{\nu}_\tau) = (0.81 \pm 2.54) \cdot 10^{-6}$$

Which leads to the following 90% C.L. limits:

$$BR(\pi^0 \rightarrow \nu_e\bar{\nu}_e) < 1.73 \cdot 10^{-6}$$
$$BR(\pi^0 \rightarrow \nu_\mu\bar{\nu}_\mu) < 7.77 \cdot 10^{-6}$$
$$BR(\pi^0 \rightarrow \nu_\tau\bar{\nu}_\tau) < 4.09 \cdot 10^{-6}$$

and for the sum:

$$\Sigma_{e,\mu,\tau} BR(\pi^0 \rightarrow \nu\bar{\nu}) < 9.9 \cdot 10^{-6}$$

Which is an improvement of the existing limit as will be discussed in section 10.5 .

10. DISCUSSIONS AND CONCLUSIONS

In fig.41 the inelasticity distributions, $y = E_{hadron}/E_\nu$, are shown separately for events with a μ^- and a μ^+ from the $\rho = 1$ target and are compared with distributions calculated from the smoothed unfolded spectra expected for CC ν_μ and $\bar{\nu}_\mu$ interactions (see section 2.2.2).

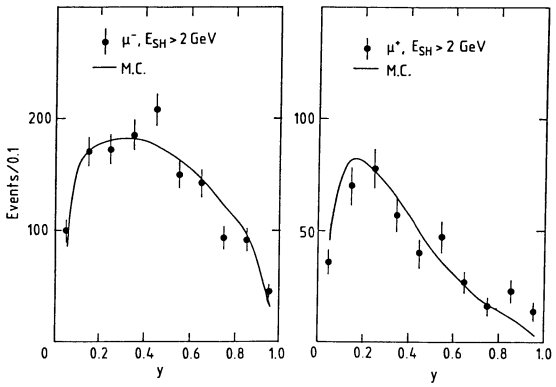

Figure 41: Distribution of the inelasticity $y = E_h/E_\nu$ of (1μ) events recorded with the $\rho = 1$ target. The curve shows the prediction for charged-current ν_μ and $\bar{\nu}_\mu$ events.

There is agreement between the data and the expectation which supports the conclusion that all events with a muon are induced by CC ν_μ and $\bar{\nu}_\mu$ interactions.
The result for the ratio of prompt $\bar{\nu}_\mu$ to ν_μ events is $0.49 + 0.24 - 0.12(\text{stat.}) \pm 0.03(\text{syst.})$ for neutrino energies above 20 GeV (see table 7); using the $\bar{\nu}_\mu/\nu_\mu$ total cross-section ratio $\sigma_{\bar{\nu}}/\sigma_\nu = 0.507$ [93], a flux ratio of $0.96 + 0.47 - 0.24(\text{stat.}) \pm 0.05(\text{syst.})$ is obtained. Expressed in terms of a flux asymmetry:

$$(\nu_\mu - \bar{\nu}_\mu)/(\nu_\mu + \bar{\nu}_\mu) = (2 \pm 16 \pm 2)\%$$

In table 27 the results of other experiments for this ratio are given. Also the result for the prompt μ^+ μ^- rates from a 350 GeV p-Fe experiment [75] is given.
Except for the BEBC electron neutrino results all values seem to be compatible with equal fluxes of prompt anti-neutrino and neutrino or μ^+ and μ^-, as expected from heavy flavour production and decay. The BEBC results are discussed in the next section.

In fig.39 the $(0\mu) - 0.33 \cdot (1\mu)$-spectrum is shown, together with the (CC + NC) ν_e-signal as expected from $D\bar{D}$-production (n = 5) plus conventional background, smeared with the detector acceptance. The used conventional ν_e-background from Monte Carlo (dotted line) is also indicated separately. As can be seen from this figure there is good agreement between data and the $D\bar{D}$-model, so an excess of (0μ)-events at low energies, not explainable by this model and seen in the CHARM 1979 beam dump data [4], is not confirmed by this experiment.

10.1 ELECTRON-MUON UNIVERSALITY

The results of chapter seven, table 23, 24 and 26, point in the direction of an excess of muon neutrinos over electron neutrinos, possibly not accompanied by muons. Assuming $D\bar{D}$-production and semi-leptonic decay leads to a contradiction. What could be the cause of such an excess? First possible experimental errors will be discussed, to assess the significance of any possible inconsistency.

The most likely explanation for the obtained asymmetry is an error in the determination of the conventional background: the conventional background for muon neutrino events is large (i.e. prompt/conventional = 0.68 for $\rho = 1$, $E_\nu > 20$ GeV) and a small error in the determination of the number of protons on target, deadtime calculation or dump density has a large effect on the derived prompt signal.

Table 27: Comparison of prompt ν, $\bar{\nu}$ and μ^-, μ^+ rates above 20 GeV.

Muon neutrinos derived from CC events		
experiment	asymmetry $(\nu_\mu - \bar{\nu}_\mu)/(\nu_\mu + \bar{\nu}_\mu)$	ratio $\bar{\nu}_\mu/\nu_\mu$
BEBC [33]	-0.09 ± 0.11	$1.20\ ^{+0.30}_{-0.24}$
CDHS [34]	$0.13 \pm 0.12 \pm 0.04$	$0.79 \pm 0.19 \pm 0.04$
CHARM	$0.02 \pm 0.16 \pm 0.02$	$0.96\ ^{+0.37}_{-0.27} \pm 0.04$
FMOW [35]	$-0.06 \pm 0.11 \pm 0.08$	$1.12 \pm 0.24 \pm 0.17$
Electron neutrinos derived from CC events		
experiment	asymmetry $(\nu_e - \bar{\nu}_e)/(\nu_e + \bar{\nu}_e)$	ratio $\bar{\nu}_e/\nu_e$
BEBC [33]	0.38 ± 0.14	$0.45\ ^{+0.16}_{-0.13}$
Prompt muons from single tracks		
experiment	asymmetry $(\mu^+ - \mu^-)/(\mu^+ + \mu^-)$	ratio μ^-/μ^+
CCFRS [75]	-0.06 ± 0.09	1.13 ± 0.20

However, the counting of the amount of protons has been done with great care (see appendix D) and the protons were registered simultaneously by three independent beam current transformers, all three agreed within 0.2%.

The deadtime measurement was carried out by three independent circuits, the obtained deadtime agreed with a Monte Carlo simulation of the deadtime generating signals. The three methods of deadtime calculation agreed within the systematic error quoted (see appendix D).

The dumps were machined with a precision of 0.1 mm and checked before and after exposure. No deviation > 0.4% from the nominal dimensions could be found.

Changes in target density caused by temperature rise of the dumps were checked by monitoring the muon flux in the muon shield during several hours after switching to the $\rho = 1$ dump which had cooled down to ambient temperature. No changes in muon flux of any significance could be observed.

It was suggested that the target densities could also change due to shock waves, caused by the high local amount of energy per time deposited in the metal. A comparison of the muonflux per incident proton during high and low intensity beam showed that this effect must have been negligibly small.

A systematic error of 0.5% was assigned to the density of the $\rho = 1/3$ target to take into account the above mentioned effects.

An underestimation of the "leakage" of the density 1/3 target would also result in a too high muon neutrino signal. The leakage correction is described in section 4.7, 5.1.1 and appendix B.

Interactions of the beam with the vacuum pipe or other material upstream of the dump (scraping) would give a large wide-band beam background of muon neutrinos, again resulting in an asymmetry with the electron neutrinos. As described in section 3.1 great care has been taken to avoid beam scraping and 26 ionization chambers were mounted along the beamline to detect the effect. A subtraction of 0.6% of the conventional background of the density one target was made to the prompt signal to correct for the small amount of unavoidable material upstream of the dump (residual gas in vacuum tube, vacuum flanges and SEM-grid, see appendix F).

All the above described effects would give rise to a contamination of the prompt charged current muon neutrino energy spectrum with the conventional spectrum.
In fig.42 the spectrum is given of prompt CC ν_μ events minus the prompt CC ν_e events. In this figure are also given, as a histogram, the energy spectrum of conventional CC ν_μ and the expected prompt CC ν_μ energy spectrum from D-meson decay, produced according to equation (70) with $n = 5$. The two Monte Carlo spectra are normalized to the excess of CC ν_μ events above 20 GeV. The conventional spectrum given in fig.42 amounts to 16% of the total for the density one target.
As one can see in fig.42, the excess of CC ν_μ events is not compatible with the conventional background.
The conclusion is that above mentioned errors are unlikely.

Another obvious error would be an underestimation of the correction for fake CC ν_μ events due to decay of a pion or kaon of sufficiently high energy in the hadronic shower of a (0μ)-event. The π/K-decay correction is described in section 4.5.3 and displayed in fig.34 as function of shower energy. The maximal correction is 3.0 ± 0.5 % for shower energy above 20 GeV. The effect of this systematic error on the e-μ asymmetry is given in table 25. An independent analysis of this correction for another experiment with the same detector and with much higher event statistics [32] gave a compatible result (In that experiment the maximal correction is 6% of the (0μ) events, but an event was considered to be a (1μ) event if a muon track pointed to a circle with radius of 30 cm instead of 20 cm around the vertex. Because the distribution of the distance to the vertex in the vertex plane for decay muons is flat, one derives from [32] a correction for $E_{shower} > 20$ GeV of $\approx 0.06 \cdot (20/30)^2 \cdot 2/1.7 = 3.14\%$ (the last factor is a correction for a small difference in (1μ)-event definition)). The underestimation of faked (1μ)-events by π/K-decay in the shower would give rise to fake (1μ)-events with high inelasticity $y = E_{hadronic}/E_{tot}$. From fig.34 one can see that the effect is practically absent at low shower energies. Since the probability for a pion or kaon to decay is inversely proportional to its energy the fake (1μ)-events will have a y-value close to one.
In fig.43 the distribution of $y_{observed} = (E_h/E_\nu)_{observed}$ for extrapolated (1μ)-events is shown, where the only correction applied on the used event sample was the scan (see section 4.5.1.). In this figure the expected $(E_h/E_{tot})_{observed}$ distribution from Monte Carlo simulation is given as a histogram. For this simulation the D-production model of equation (70) of section 6.1 was used, with an $(1-x)$ exponent of five and the measured detector resolution and acceptance as described in section 4.5.6 .
Varying the $(1-x)$ exponent between four and six gave the same result.
Some excess events at high y can be caused by (1μ)-events with a muon traversing not enough magnetized iron to measure the momentum (unfitted muons). It is shown in chapter 7 that the Monte Carlo used predicts the right amount of unfitted muons. In fig.43 are indicated the cosmic background correction at $y = 0$, described in section 4.5.4 and the π/K-decay correction at $y = 1$.
If the excess of (1μ)-events would have been caused by π/K-decay inside hadronic showers of (0μ)-events, one would expect the highest y-bin to lie, as indicated by a cross in fig.43, at 3.4 σ out of the measured value, thus this error is unlikely.

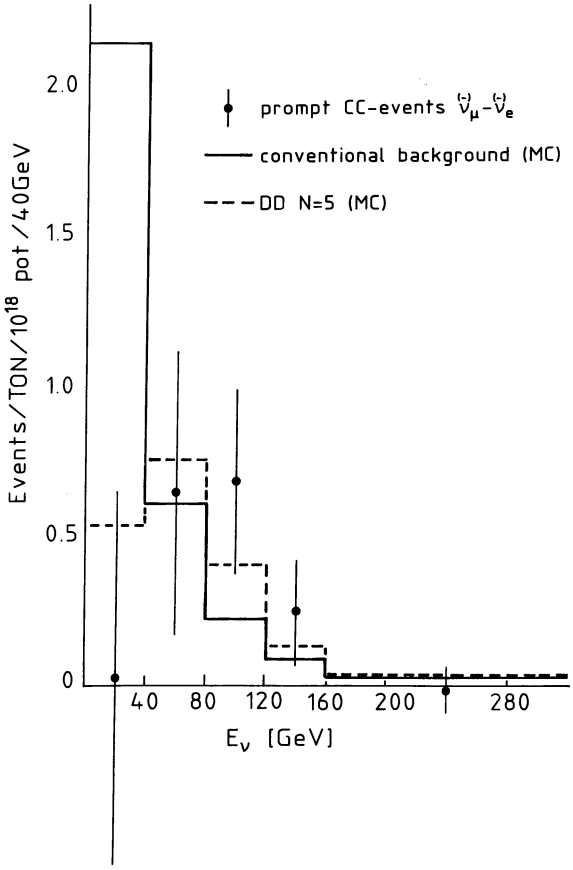

Figure 42: Prompt CC ν_μ events minus prompt CC ν_e events. The full histogram is the Monte Carlo prediction of the conventional background, normalized to the excess of CC ν_μ events above 20 GeV. The dotted histogram gives the $D\bar{D}$-prediction for n = 5 and is normalized in the same way as the full histogram.

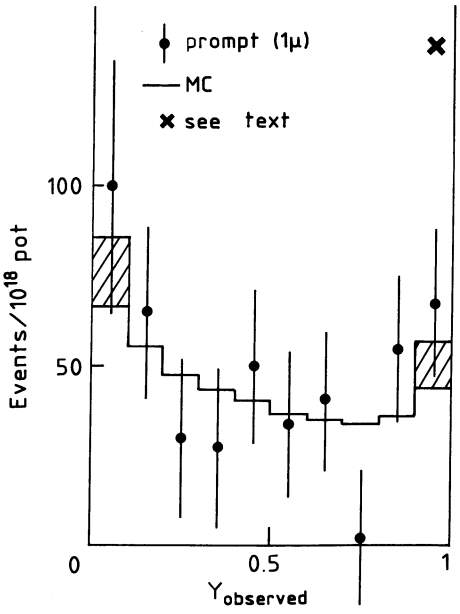

Figure 43: y-distribution for raw, extrapolated (1μ)-events. y is defined as $E_{hadron}/E_{neutrino}$. The histogram gives the Monte Carlo prediction, the hatched parts at y = 0 and y = 1 are the corrections for respectively cosmic-ray background and π/K-decay.

Other possible experimental errors are a wrong energy calibration or determination of resolution and acceptance of the detector. These errors would be of little significance for the results with a cut in neutrino energy of 20 GeV, because there are very few prompt events around that energy.

Moreover, the prompt ν_μ and ν_e events have the same distribution of hadronic energy and only an error in muon or electron energy calibration would contribute to the measured asymmetry. The muon and electron energy calibration are described in section 3.4.8, the effect of their systematic error on the asymmetry is given in table 25.
The amount of CC ν_e-events derived from the $(0\mu) - 0.33 \cdot (1\mu)$ spectrum agrees with the "direct search" method, as described in section 4.6.2 .

An error due to overestimation of the simulated conventional electron neutrino background is unlikely, because this background is small (17% of total ν_e events above 20 GeV for $\rho = 1$ target). The conventional electron neutrinos are mainly produced by K_{e3}-decay and the Monte Carlo program used reproduces the correct conventional ν_μ-spectrum from $K_{\mu 2}$-decay (see section 5.1.). In addition, the simulated conventional ν_e background is compatible with the extrapolated result (see table 7).
In conclusion, it seems that the errors are assigned correctly.

10.1.1 THEORIES ABOUT PROMPT ELECTRON-MUON ASYMMETRY

In this section some possible physical explanations will be given for the occurence of a prompt e-μ asymmetry.
A well-known case for the conventional neutrino flux is the purely leptonic decay of the lightest charged scalars: due to helicity suppression the branching ratio for $\pi \to e\nu_e$ is only $1.2\ 10^{-4}$ against a branching ratio for $\pi \to \mu\nu_\mu$ of almost 100%. For kaons these numbers are $1.5\ 10^{-5}$ and 0.64 respectively.
This decay mode is too slow for the prompt decaying charmed equivalent of pion and kaon, i.e. D and D_s, as explained in section 2.4.1 , where an upper limit was derived of $D \to \mu\nu_\mu \leq 0.1\%$ and $D_s \to \mu\nu_\mu \leq 0.2\%$. In the same section it is explained that the branching ratio of $D_s \to \tau\nu_\tau$ can be around 2 %, but ν_τ events would not lead to an excess of 1μ events (see also chapter 8).

Another possibility is that the semi-leptonic branching ratio of charmed quarks is not equal for the channels $c \to s\mu\nu_\mu$ and $c \to se\nu_e$. A mechanism, where the charm decay is mediated by a charged Higgs boson, $c \to sH^+$, $H^+ \to \mu^+\nu_\mu$, is given by Barger et al. [109].

A summary of semi-leptonic branching ratios for charmed quarks as measured in $e^+\ e^-$ collisions is given by Bartel et al. [110]. Some of the electron semi-leptonic branching ratios in this summary are measured at $\sqrt{s} = 3.77$ GeV, the J/ψ mass. Since it is not clear whether the $D^\pm$, D^0 mixture is the same at this energy, only the energies > 10 GeV were taken to calculate the weighted average of:

$$c \to se\nu_e = (10.38 \pm 0.78)\% \quad c \to s\mu\nu_\mu = (8.62 \pm 0.85)\% \tag{81}$$

Due to the large energy cuts made in the experiments given in the summary of [110], part of the charmed hadron spectrum had to be guessed with the help of heavy quark fragmentation functions, which explains the large errors in (81). The values of (81) seem not to indicate a higher semi-leptonic branching ratio for muons although cannot exclude it.

It was suggested [77] that the production of a light neutral scalar with mass below 1 MeV/c^2 could give an excess of ν_μ, assuming neutrinos are massive and the muon neutrino is much heavier than the electron neutrino. Such a particle would than preferably decay into $\nu_\mu \bar{\nu}_\mu$. Also the π^0 can be considered as a candidate, as is discussed in chapter 9. No experimental evidence for the existence of exotic scalars has been reported so far [24].

The asymmetry between electron and muon neutrinos could be caused by neutrino oscillations [111]. Oscillations of $\nu_e \to \nu_x$, where ν_x is considered to be sterile, could lead to a depletion of electron neutrino events. Experimental limits on $\nu_e \leftrightarrow \nu_x$ exist from nuclear reactor experiments [111], which can be applied here.

To generate the ν_e spectrum, the $D\bar{D}$ model was used as described in chapter 6, with an $(1-x)$ exponent of five. Contributions of the hadronic cascade in the dump target were taken into account. The generated CC ν_e spectrum for different values of the mass difference Δm between ν_e and ν_x and mixing angle ϕ was compared with the measured CC ν_e spectrum obtained by the direct search method described in section 4.6.2. .
It was found with 95% confidence level that mass difference and mixing angle should lie in a region with $\Delta m^2 > 100\ (eV/c^2)^2$ and $\sin^2(2\phi) > 0.35$. This region is excluded by reactor experiments, see [111]. In case of $\nu_x = \nu_\tau$ these limits do not change, due to the fact that CC ν_τ events are suppressed because of the high τ mass (see chapter 8) and the branching ratio of $\tau \to e\nu_e\nu_\tau$ is only 17%.
Oscillations of $\nu_x \leftrightarrow \nu_\mu$ can not be excluded.

It could be that for some reason the neutrino-nucleon cross-section is higher for ν_μ than for ν_e . Precise measurements of the ν_e cross-section are not available.

10.1.2 COMPARISON WITH OTHER EXPERIMENTS

The ν_e-ν_μ asymmetry in a proton beam dump experiment has been measured by three other experiments. The results are listed in table 28.

Table 28: Asymmetry in electron neutrino and muon neutrino rates for $E_\nu > 20$ GeV.

asymmetry $= (\nu_\mu - \nu_e)/(\nu_\mu + \nu_e)$ ratio $= \nu_e/\nu_\mu$		
Experiment	Asymmetry	Ratio
BEBC [33] "throughgoing muons" used	-0.07 ± 0.08	$1.14\ ^{+0.19}_{-0.16}$
BEBC [33] only event rates used	$0.48\ ^{+0.24}_{-0.35}$	$2.9\ ^{+7.9}_{-1.2}$
CDHS [34]	$0.078 \pm 0.071 \pm 0.038$	$0.86 \pm 0.12 \pm 0.05$
CHARM	$0.21 \pm 0.08 \pm 0.03$	$0.65\ ^{+0.12+0.04}_{-0.10-0.03}$
FMOW [35]	$0.027 \pm 0.064 \pm 0.040$	$0.95 \pm 0.12 \pm 0.08$

Two of them, BEBC [33] and CDHS [34], were taking data in the same beam as this experiment, one was an independent experiment performed at Fermilab by the FMOW collaboration [35]. All of them used two target densities and the extrapolation method to correct for the conventional background. The proton energy was 400 GeV for the experiments listed in table 28 . Some features of these experiments are listed in table 30.

CDHS and FMOW used sampling calorimeters with electronic detection elements like this experiment, BEBC was a bubble chamber, surrounded by walls of MWPCs.
BEBC was the only experiment able to measure ν_e and $\bar{\nu}_e$ separately, CHARM and FMOW have developed statistical methods to separate the CC $(\nu_e + \bar{\nu}_e)$ events using the difference between hadronic and electromagnetic showers (see [33], [35], section 4.6.2 and [51]).

An important aspect for determining the rate of prompt electron neutrino and muon neutrino events for all these experiments is the difference in detector acceptance for the various types of events (CC ν_μ, CC ν_e, NC). Below a certain energy the trigger efficiency decreases, the reconstruction of the vertex position becomes difficult and the energy resolution gets poor: a lower-cut in shower energy is necessary. The reconstruction of charged current muon neutrino events can give problems because the muon can be unrecognizable if it is hidden inside the hadronic shower or leaves the detector at the side. For the momentum measurement of the muon a magnetic spectrometer is necessary, whose resolution depends on the momentum of the muon: a lower-cut in muon momentum is necessary. Since one wants to compare the different event rates at the same incident neutrino energy, acceptance corrections have to be applied. These corrections and their influence on the systematic error become bigger as the acceptance for a certain type of event decreases. All four experiments have a higher acceptance for CC ν_e events than for CC ν_μ events, the NC acceptance is the smallest. To calculate the acceptance for CC ν_e events one needs the y-distribution and the detector response to electromagnetic showers. The y-distributions are well known [72], the detector response to electrons is measurable in a test beam.
For the calculation of the CC ν_μ-acceptance one needs in addition the x-distribution, to determine the angular distribution of the muons. Since the x-distribution of CC neutrino interactions are not so well known (they depend on the nuclear structure of the target [36]) it is advantageous to have a detector with a high acceptance for CC ν_μ-events.
It is further important to have all energy and momentum cuts as low as possible in order to make the detector acceptance less depending on the shape of the measured energy spectrum.
In the following sections the other experiments will be discussed in some detail.

BEBC

BEBC (Big European Bubble Chamber [33]) was a bubble chamber filled with a mixture of neon (74 mole%) and hydrogen. Its fiducial volume of 16.6 m^3 and 11.5 ton had approximately the shape of a cylinder with diameter of 3.60 m and height of 1.66 m. A large superconducting magnet provided a uniform field of 3.7 Tesla. The pressure vessel was surrounded by proportional tubes to detect charged particles crossing the walls and to give timing signals to be able to separate different events on the same photograph.
On the downstream side two walls of MWPCs were placed, separated by the iron return yoke for the magnetic field, to detect reaction products escaping the liquid and called External Muon Identifier (EMI). This system mainly served to distinguish muons from hadrons, because the latter would interact in the iron between the two walls.
On the upstream side a wall of MWPCs was used as veto against incoming charged particles. More details can be found in table 30 .

In BEBC the momentum of the primary interaction products was measured by the curvature of their tracks in the magnetic field. A correction of 20% in hadronic energy had to be made to take into account unseen neutral particles.

The main problem for BEBC in this beam dump experiment was the low event rate due to the relatively small fiducial mass. Especially for the extrapolation to infinite target density of the CC ν_μ events with a high conventional background this was a big handicap.
One has tried to improve the event statistics by using so called "throughgoing muons" [33], which are muons from CC ν_μ-events produced in the material upstream of BEBC, traversing the MWPCs of veto wall and EMI. How it is possible to distinguish between muons from upstream produced CC ν_μ-events and muons produced in the dump that reach the detector is hard to understand: because of multiple scattering the latter will have a broad distribution both in angle and lateral position. Also there will be a large contribution from muons which travelled outside the shielding and were scattered back to the detector region in material surrounding the fiducial volume. These muons can be of conventional as well as of prompt origin. In addition, the effect of the different amount of shielding for the density one and one third target (= 2 m of solid copper) on the endpoint of the muon energy spectrum is very hard to calculate. Already without this contamination the method is tricky, because for none of the "throughgoing muon" events the hadronic energy is known, so to derive the proper prompt/conventional-ratio one fully relied on the neutrino energy spectrum and x,y distributions put in a Monte Carlo simulation.

In addition, a correction was applied on the ratio prompt/conventional from the "throughgoing muons" of -20% for ν_μ and -30% for $\bar{\nu}_\mu$ to take into account the difference in angular distribution of prompt and conventional flux, since the "throughgoing muons" cover a much larger solid angle than the events originating in the fiducial volume.
This correction depends heavily on Monte Carlo simulations and especially on charm production models. It is dangerous to use in the extrapolation method.

The reliability of the normalization with "throughgoing muons" seems doubtful. It is surprising that in the BEBC beam dump publication [33] this normalization, which is essential for the e-μ asymmetry, is explained only briefly and that for further details a reference is made to a CERN internal report which has so far (1989) not appeared.

The BEBC results without the "throughgoing muon" normalization are also given in table 28 and have a much reduced significance.

Also the BEBC collaboration has tried to simulate the conventional muon neutrino flux by Monte Carlo methods using the conventional muon flux measured in the iron shield as reference. No direct calibration of the μ-flux detectors was applied, as was done in this work (see appendix C), but a comparison of muon flux and neutrino flux from WBB exposures was used. Thus the BEBC simulation of the conventional muon neutrino flux involves an additional Monte Carlo step to simulate the horn-focussed WBB. The fact that the BEBC systematic error on the simulated conventional muon neutrino flux is smaller than the one quoted in this work (6% vs 9% for $E_\nu > 20$ GeV), while it contains more uncertainties in the input, makes one inclined to believe that it is underestimated. No details of the simulation are given in [33].

Electrons are distinguished from other charged particles in the following way: an electron candidate had to have at least two identifiers:

1. An abrupt change in curvature in the track without any newly created visible tracks at the same place, which can be caused by emission of an energetic bremsstrahlung photon.

2. An $e^+ e^-$ pair pointing tangentially to the track caused by pair production of a bremsstralung photon.

3. An $e^+ e^-$ pair lying on the track and carrying more than 10% of the track energy, caused by direct pair production.

Monte Carlo based corrections were necessary: real electron tracks might not show any of the above mentioned identifiers, some e^+e^- pairs created by other energetic γs from e.g. π^0-decay point accidentaly to a track tangent and pion or kaon tracks will occasionally show also the above mentioned identifiers.
An electron can loose a considerable amount of its energy by bremsstrahlung which causes an additional systematic error in the energy determination.

The BEBC collaboration found a remarkable asymmetry in the flux of ν_e and $\bar{\nu}_e$:

$$(\nu_e - \bar{\nu}_e)/(\nu_e + \bar{\nu}_e) = 0.38 \pm 0.14 \qquad (82)$$

i.e. a 2.7 σ effect. More ν_e were found than $\bar{\nu}_e$, though the latter are easier to distinguish because of the lower mean y of $\bar{\nu}_e$-events and the fact that the probability of energetic bremsstrahlung and pair production increases rapidly with incident electron energy.
The conventional background for electron neutrinos is much lower than for muon neutrinos so that, unless a mistake in the calculation of the number of protons on target for density one or density one-third was made, the extrapolation method can not be the cause of the found asymmetry.

Result (82) would justify a detailed description of the analysis and error calculation enough for a separate paper, because if significant, it would require new physics.

Again the briefness with which the subject is treated in [33] is unfortunate, the result is not mentioned in the abstract of the paper.

FMOW

The FMOW-collaboration performed a neutrino beam dump experiment in 1981 and 1982 at Fermilab [35]. As detector a sampling calorimeter was used similar to CDHS and CHARM (see table 30). The detector target consisted of 30 modules of 1.5·3 m^2 each, with 12 lead plates submerged in liquid scintillator, amounting to 14.4 radiation lengths and 0.5 absorption lengths. Every module was followed by two orthogonal planes of proportional drift tubes of type similar as described in section 3.4.3. The beam axis was not centered in the middle of the detector but was displaced by 80 cm over the longest side. At the downstream side a muon spectrometer was built, consisting of iron toroidal magnets and MWPCs. A veto plane in front of the detector tagged incoming charged particles.
The Fermilab beam dump differed from the CERN experiments mainly at two points:

1. The distance between detector and dump was only ca. 56 m against ca. 450 m in the CERN case. Magnetized muon shielding was used to bend away muons from the direction of the detector. The covered solid angle was $80 \cdot 10^{-5}$ sr against e.g. $2.4 \cdot 10^{-5}$ sr for CHARM.
   The advantage of a large solid angle was a higher prompt/conventional ratio for neutrino-induced events, because the prompt neutrino flux from charm decay has a broader angular distribution than the conventional neutrino flux.
   The disadvantage was a low signal to noise ratio ($\approx$ 1/300), because the shielding magnets could not bend away all muons sufficiently well and the very high muon flux, striking material close to the detector, gave additional background.

2. The tungsten "dumps" were too small: The $\rho = 1$ target and $\rho = 1/3$ target were only respectively 4.5 λ_{proton} (43.2 cm of W) and 3.5 λ_{proton} (33.2 cm of W) long, their diameter was 2.5 cm. This means that a large part of the hadronic cascade leaked out of the dump into copper, iron and air.

Already in this experiment, where only in the case of the $\rho = 1/3$ target small corrections had to be made, much effort was spent to control the effect of the leakage (see section 5.1.1. and appendix B). In table 29 the percentage of longitudinal leakage as function of the generation in the hadron cascade of the produced particles and the sequence of the particles in the cascade is given for the Fermilab and CERN targets, using equation (67) of section 5.1.1..

Table 29: Longitudinal leakage as function of parent generation.

longitudinal leakage = (particles produced outside target)/(particles produced inside target)			
generation	$\rho = 1/3$ FMOW $3.3\lambda_p$	$\rho = 1$ FMOW $4.3\lambda_p$	$\rho = 1/3$ CHARM $6.7\lambda_p$
2: 1p 1π	19%	9%	1.5%
3: 2p 1π	38%	22%	5%
3: 1p 2π	43%	26%	6%
4: 3p 1π	59%	39%	11%
4: 2p 2π	63%	43%	13%

As one can see from this table, the longitudinal leakage in the Fermilab case is large and increases rapidly with the generation number. Because the higher generations have a lower average energy the neutrino leakage will be energy dependent.

The Fermilab experiment, with its large angle of acceptance, was more sensitive than our experiment to the leakage, which had a broader angular distribution than the events coming from parents produced inside the targets. In addition to this there was the lateral leakage.

The FMOW collaboration has corrected for the small size of its dumps by assigning an effective density for each target of 0.93 and 0.38 for $\rho = 1$ and $\rho = 1/3$ respectively. Clearly one expects the total effective density to be strongly energy dependent. The fact that FMOW used a fixed effective density is remarkable.
One must conclude that the FMOW results rely heavily on Monte Carlo simulation of the longitudinal and lateral shower profiles and that the effect of the systematic error of the target densities on the e/μ-ratio is estimated optimistically. It is surprising that no details are given in [35] of the Monte Carlo methods used to calculate the effective target density.

How one can find a reliable $(1-x_F)$ exponent for charm production (see section 10.2) with an energy independent leakage correction is not understandable.

Because of the asymmetric position of the FMOW detector axis relative to the beam axis (see table 30), the rectangular fiducial volume (2.6 x 1 m^2) and the absence of a magnetic field or surrounding magnetized frame, the probability was high that a muon produced in a CC ν_μ event would leave the detector before it could traverse a sufficient number of calorimeter cells or magnetized iron of the muon spectrometer for proper reconstruction of its energy and momentum. The average acceptance for CC ν_μ events with $E_\nu > 20$ GeV was 60%, which means that 40% of the CC ν_μ-events are created by Monte Carlo. Structure functions given in [38] were used in this Monte Carlo. These structure functions were measured in an iron target, while applied for a lead target [36].

CDHS

The CDHS detector [37] consisted of 21 modules of toroidal iron magnets with diameter of 3.75 m. Between these modules drift chambers were placed to determine the energy and momentum of muons. One module consisted of a number of iron disks surrounded by a coil and interspersed with planes of scintillators. Three different types of modules were used: the most upstream ten modules had 20 discs of 2.5 cm thickness, the next five modules had 15 discs of 5 cm thickness and the last six five discs of 15 cm thickness. The first ten modules had scintillators of 15 cm width in both projections, the other modules had only horizontal scintillators of 45 cm width.
The fiducial mass was around 450 ton, the highest of the experiments described here.

The distance between the wire chambers was 50 cm of iron for the first ten modules and 75 cm of iron for the others. Therefore it was difficult to recognize a muon, because the spatial resolution of the scintillators was much worse than that of the drift chambers. For the proper reconstruction of the energy and momentum of a muon from a charged current muon neutrino event a cut of 9 GeV/c in muon momentum and a cut of 20 GeV in neutrino energy was necessary. This made the acceptance for CC ν_μ events poor. The toroidal field could only focus muons of one sign at the time and since the full detector was magnetized this meant that the acceptance for unfocused muons was much worse than for focussed muons. For this reason the field polarity was regularly changed to have data with 50 % of the time focussing conditions and 50 % of the time non focussing conditions for each muon sign. The acceptance for neutrino energy above 20 GeV averaged over both field conditions was 81% for μ^- and 90% for μ^+ for prompt CC ν_μ [34].
For the acceptance correction structure functions were used as measured in a narrow-band neutrino beam [38].

The analysis of muonless events was performed independently from the 1μ analysis. Since low energetic muons could not be distinguished with the drift chambers because of the large amount of iron in-between them, one had to use the scintillator signal to separate the (0μ)-events from the (1μ)-events.
Since the spatial resolution of the scintillators was poor, i.e. minimal 15 cm , (1μ) and (0μ)-events could not be separated on an event by event basis but one had to use a statistical analysis based on the total event length: events longer than a certain shower-energy dependent length were supposed to be CC ν_μ-events, the rest NC ν_μ or ν_e. A Monte Carlo based correction was necessary for short CC ν_μ events of 20% of the total amount of short events [34]. Again narrow-band neutrino beam measurements [38] were used for the x and y distributions.

Table 30: Some features of neutrino beam dump experiments.

	BEBC	CDHS	CHARM	FMOW
detector type	bubble chamber	sampling calorimeter	sampling calorimeter	sampling calorimeter
detector target material	Ne-H_2 mixture 74 mole % Ne	iron	marble ($CaCO_3$)	lead
detector shape	cylinder diam. 3.6m height 1.7m on axis	cross-section circle 3.6m diam. 0.45m off axis	cross-section square 3x3 m^2 of marble 0.5m iron frame on axis	cross-section rectangle 1.5x3. m^2 0.8m off axis at longest side
fiducial mass	11.5 ton	ca.450 ton	90.6 ton	ca.50 ton
sampling width	$\lambda_\pi = 140$ cm $X_r = 43$ cm	min. 0.3 λ_π min. 2.6 X_r	0.2 λ_π 1 X_r	0.5 λ_π 14.4 X_r for one module of 12 Pb plates
active elements		scintillators drift chambers	scintillators prop. drift tubes streamer tubes	liquid scint. prop. drift tubes drift chambers
μ – spectrometer	EMI see text	whole detector magnetized	magnetized frame + end spectrom.	end spectrom.
dump dimensions	cross-section 31x31 cm^2 $\rho = 1$: 20 λ_p $\rho = 1/3$: 6.7 λ_p			diam. 2.5 cm $\rho = 1$: 4.5 λ_p $\rho = 1/3$: 3.5 λ_p
correction upstr. material [% of non-prompt $\rho = 1$]	0.6%	0.6%	0.6%	ca. 6%
distance to dump	406 m	465 m	487 m	60 m
angular acceptance	$\leq$ 4.4mrad	$\leq$ 4.4mrad	$\leq$ 3.4 mrad	$\Theta \geq -10$ mrad $\Theta \leq 40$ mrad
protons on target [10^{18}]	2.7	1.2	2.0	0.20
typical dead-time		8-15%	14-22%	30%
P_μ cut,CC ν_μ analysis [GeV/c]	3	9	1	3.5
E_{sh}-cut (0μ)-analysis [GeV]	10	5	2	10

10.1.3 CONCLUSION ON PROMPT ELECTRON-MUON ASYMMETRY

1. The BEBC and FMOW results are unreliable where they concern the e-μ universality: too much use has been made of Monte Carlo techniques at crucial places, the systematic errors are underestimated and badly documented.

2. The CHARM result has the smallest systematic error because of the large acceptance this detector has for CC ν_μ-events. Unfortunately the statistical error is large because of too few protons on target (half of the amount asked for, see [39] and table 3). The CDHS result has the smallest statistical error.

   Comparing the prompt CC ν_e and ν_μ rates above 20 GeV of CDHS, 2.81 ± 0.22 ± 0.10 evts/ton/10^{18} POT and 3.28 ± 0.39 ± 0.22 evts/ton/10^{18} POT respectively ([34] corrected by $(R(CDHS)/R(CHARM))^2 = 0.912$), and CHARM (table 24) one sees that the largest difference is in the CC ν_μ-rate. The CHARM detector is superior in recognizing CC ν_μ events.
   It makes no sense to compare the event rates for the two target densities of both experiments since the difference in acceptance between the CDHS and CHARM detector for conventional CC ν_μ events, with a much lower average energy than the prompt events, was large.

3. The CHARM result on the ν_e-ν_μ asymmetry is just over two standard deviations away from zero, the so far (1989) unpublished CDHS result one standard deviation, both in the same direction. Combination of the CDHS and CHARM results gives:

   $$A = 0.144 \pm 0.053 \pm 0.024$$

   where the errors are added in quadrature.
   This value is 2.5 standard deviations away from the prediction A = 0 of standard physics, which is an intriguing result.

4. The indication of a non-zero asymmetry between prompt electron neutrinos and muon neutrinos from earlier beam dump experiments [2], [3], [4], and of an earlier analysis of the data from this experiment [51], could not be eliminated, and thus more experimental data is necessary. An experiment, in the state of data taking at the time of writing of this thesis, which could give more clarity is the NA34 experiment at CERN, performed by the HELIOS collaboration [40]. This experiment is dedicated to measure single charged leptons (e, μ) and pairs (ee, $\mu\mu$, μe) produced in 450 GeV pN collisions at the CERN SPS. Unfortunately the prospects for results on the e-μ universality are not so good, due to a disappointing e, μ recognition capability.

   A proposal for a new proton beam dump experiment at the 3 Tev UNK accelerator in Serpuchov has been made [67.] The main goal will be the search for tau neutrinos. With some extensions to the proposed detector the e-μ asymmetry could be studied also.

   At CERN the CHARM-II neutrino detector [66], dedicated to detection of ν_μe scattering, which has been build at the place of the old CDHS and CHARM detectors, could be used to bring more clarity to the e-μ (a)symmetry. The target facilities used for the experiment described in this thesis still exist, except for the dumps.
   The CHARM-II detector consists of 420 glass plates of 400 x 400 x 5 cm^3, with streamer tubes and scintillators as active elements in-between, followed by a muon spectrometer of iron toroids with MWPCs and scintillators. It has a mass of ≈ 600 tons, i.e. 6 times more than the detector of this experiment. In addition the CHARM-II detector has a 2 times finer granularity, so it has an excellent capability of separating charged current muon neutrino events from other events.
   A disadvantage is the absence of a surrounding magnetized frame, so the momentum of a muon can only be determined where it traverses the end-system or stops inside the detector.
   With the high event statistics possible and the above mentioned capability of recognizing CC ν_μ-events this handicap can be easily overcome by using Monte Carlo techniques.

10.1.4 SOME SUGGESTIONS FOR FUTURE EXPERIMENTS

The main problems encountered in this experiment were the relatively high conventional background ($\approx$ 2 x prompt for $\rho = 1$ and E > 20 GeV), the low event rate and, as a technical problem, the cooling of the targets.

The conventional background could be reduced by using more dense target material. In table 31 the interaction lengths of some materials are given.

Table 31: Properties of some materials suitable for a beam dump.

MATERIAL	A	Z	ρ [g·cm^{-3}]	λ [g·cm^{-2}]	λ [cm]
Fe	55.85	26	7.87	131.9	16.76
Cu	63.55	29	8.96	134.9	15.06
W	183.85	74	19.3	185	9.59
Pt	195.08	78	21.45	189.7	8.84
Pb	207.19	82	11.35	194	17.09
U	238.03	92	18.95	199	10.50

Tungsten, uranium and platinum clearly have a higher density than copper. Platinum is too expensive, uranium too dangerous to use. Only tungsten seems to be feasible as target material, though it is brittle, hard to machine and has a poor heat conductivity. One could think of using tungsten discs of 10 mm thickness and about 300 mm diameter. For the target of highest density one can use, for example, a spacing of 1 mm between the discs for cooling purposes, filled up with copper plates or tubes with coolant. The density one-third target gets then a spacing of 23 mm. With this configuration a reduction of the conventional background of about 30 % would be possible.

In order to increase the event rate one has to place the detector closer to the target, which means that more effective shielding is necessary. A possibility is to use uranium instead of iron [67]. ^{238}U is a waste product of the nuclear industry and available in large quantities. In table 32 the dE/dx for muons in Fe and U are compared at different P_μ

Table 32: Comparison of dE/dx for Fe and U at different P_μ

P_μ	Fe		U	
[GeV/c]	[GeV g^{-1} cm^2]	[GeV m^{-1}]	[GeV g^{-1} cm^2]	[GeV m^{-1}]
10	0.20 10^{-2}	1.42	0.16 10^{-2}	3.07
50	0.24 10^{-2}	1.71	0.23 10^{-2}	4.45
200	0.35 10^{-2}	2.54	0.51 10^{-2}	9.61
400	0.50 10^{-2}	3.65	0.89 10^{-2}	16.90
data from [91], density of cast-iron used = 7.25 g cm^{-3}				

As one can see a reduction in shield length of more than a factor two is achievable. The use of a uranium shield and positioning of the detector directly behind the shield would have given for this experiment a factor $\approx$ 15 more events/proton.

Since the prompt neutrino flux from charm decay has an on average wider angular distribution than the conventional neutrino flux (see chapter 6), a shorter distance between dump and detector will also increase the prompt/conventional-ratio.

10.2 CHARM PRODUCTION

To determine the charm cross-section the prompt charged current electron neutrino signal was used because it had a smaller error than the muon neutrino signal. The absence of lepton number changing mechanisms such as neutrino oscillations was assumed.

The charm cross-section was measured for x_F values centered around $x_F = 0.33$, as can be seen from fig.36. The result seems to be in favour of the quark- and gluon-fusion model (see section 2.3): A $(1-x_F)$ exponent around 6 in equation (69), a cross-section around 15 μbarn/nucleon at $\sqrt{s} = 27$ GeV and no evidence for forward Λ_c-production.

However, since the semi-leptonic branching ratio of Λ_c might be very small [75], [82] this result does not completely exclude flavour excitation or other models of forward charm production.

The difference in the total cross-section using parametrization (69) or (70) in the fit can be explained by the very low acceptance around $x_F = 0$. The cross-section for $D\bar{D}$-production in p-p interactions, as measured at low x_F by the EHS-collaboration [81], can be well described with the parametrization of equation (69). However, an additional systematic error of 20% should be attributed to the absolute cross-section due to the model dependence. This additional error is left out of consideration in the following comparison with experiments which used the same model.

If one assumes a semi-leptonic branching ratio for the D-meson decay of 0.114 ± 0.013, [86], a total $D\bar{D}$-production cross-section of

$$\sigma_{D\bar{D}} = 921 \begin{matrix} +132 \\ -167 \end{matrix} \pm 149 \ \mu\text{barn/nucleus} \quad \text{for } A = 63.5$$

is found. Using the 400 GeV p-p data of the LEBC/EHS-collaboration, $\sigma_{D\bar{D}} = (30.2 \pm 3.3)\ \mu$b [81], and assuming a cross-section dependence $\propto A^\alpha$ one finds a value of $\alpha = 0.82 + 0.05 - 0.07$. Compared to the value for the exponent in (69) of $n = 4.9 \pm 0.5$ from LEBC/EHS [81] our value (74) is higher. This may indicate that α depends on x_F and decreases with x_F as seen in hadro-production of lighter flavours [87], caused by nuclear effects, which are then also responsible for the deviation of α from the expected value of one for the quark-gluon model, since the cross-section is measured around $x_F = 0.33$. The LEBC/EHS-experiment also finds a very low rate of leading Λ_cs and agreement with the quark- and gluon-fusion model after introduction of a k-factor with a value of around two.

The CCFRS-collaboration [75] has studied charm production in a 360 GeV p-Fe experiment, measuring the production of prompt single muons from semi-leptonic charm decay. Their results are, scaling to 400 GeV by a factor of 1.20 ± 0.06 and by a factor 1.11 ± 0.03 for the difference in A: $\sigma_{D\bar{D}} \cdot BR = 134.5 \pm 12.5 \pm 23$ μbarn (A = 63.5) and $n = 5.0 \pm 0.8$, where they have used parametrization (70). Together with the result (75) from the ν_e-channel one finds for the asymmetry of semi-leptonic D-decay in ν_μ or ν_e : $(\mu - e)/(\mu + e) = 5 \pm 10$ % [94], which is compatible with an equal semi-leptonic branching ratio for the D into both channels.

The ACCMOR collaboration [18] finds in 200 GeV proton-silicon interactions a D production with $n = 5.5 + 2.1 - 1.8$, $b = 1.4 + 0.6 - 0.4$ for the p_T distribution (71) and a total cross-section of $1.5 \pm 0.7 \pm 0.1$ μb/nucleon. The cross-section was parametrized like $d^2\sigma/dx_F d^2p_T \propto (1-x_F)^n e^{-bp_T^2}$. In addition a low production rate for Λ_c is found. These results are compatible with the results of this experiment, taking into account a $\approx$ 5 times lower charm production cross-section, due to the difference in C.M. energy (see fig.8).

A 400 GeV proton beam dump experiment performed at FNAL with Be, Cu and W targets [88] yielded a value of $\alpha = 0.75 \pm 0.05$, which agrees with the result of this experiment. The charm cross-section from the same experiment for 400 GeV p-W collisions [89] scaled to Cu with $\alpha = 0.82$ is $\sigma_{D\bar{D}} \cdot BR = 120.3 \pm 6.0 \pm 17.9$

μbarn/nucleus (A = 63.5) which agrees with (75). However the value of $n = 3.2 \pm 0.2$ for the exponent in (70) is incompatible with our result (75). The difference can be explained partly by the assumption of a softer energy spectrum for the neutrino in the rest frame of the D, used by [89]. Using the same spectrum would cause a change of -0.5 in the exponent [79]. The n-value of Duffy et al. [89] excludes an x_F-dependence of α as discussed above.

10.3 LIMIT ON TAU NEUTRINO PRODUCTION

In chapter 8 a rate for charged current tau neutrino events with $E_\nu > 2$ GeV was found of:

$$N(CC)_{\nu_\tau} = 28 \pm 87 \text{ evts/ton}/10^{20}\text{POT}$$

and a limit for the ν_τ flux of:

$$\Phi(\nu_\tau + \bar{\nu}_\tau) < 21\ \%\ (90\%\ \text{C.L.})$$

of the total prompt flux with neutrino energy above 2 GeV.
The BEBC collaboration found in the same beam [41]:

$$N(CC)_{\nu_\tau} = -14 \pm 12 \text{ events}$$

for 11.5 ton of fiducial mass and $1.91 \cdot 10^{18}$ POT, and

$$\Phi(\nu_\tau + \bar{\nu}_\tau) < 13\ \%\ (90\%\ \text{C.L.})\ \text{of the total prompt flux}$$

Both results are for neutrino energies above 20 GeV.

10.4 TEST OF ELECTRON-MUON UNIVERSALITY

In chapter 8 also a value was derived for the relative coupling strengths of ν_e and ν_μ to the weak neutral current:

$$g_{\nu_e \bar{\nu}_e} / g_{\nu_\mu \bar{\nu}_\mu} = 1.09 + 0.18 - 0.20$$

Combination of this value with a result obtained from an exposure of the CHARM detector to a 160 GeV narrow-band beam [32], gives:

$$g_{\nu_e \bar{\nu}_e} / g_{\nu_\mu \bar{\nu}_\mu} = 1.05 + 0.15 - 0.18,$$

consistent with universality of $\nu_e \bar{\nu}_e$ and $\nu_\mu \bar{\nu}_\mu$ coupling

10.5 LIMIT ON BRANCHING RATIO $\pi^0 \rightarrow \nu\bar{\nu}$

With the help of the BEBC tau neutrino rate mentioned in the previous section, the limit on the decay $\pi^0 \rightarrow \nu\bar{\nu}$ can be improved. The BEBC result for CC ν_τ events, without kinematical suppression caused by the high tau mass, is [41]:

$$N(CC)_{\nu_\tau} = -25 \pm 21 \text{ events} \qquad E_\nu > 20 \text{ GeV}$$

for 11.5 ton of fiducial mass and $1.91 \cdot 10^{18}$ POT on $\rho = 1$. In the CHARM detector this would give:

$$N(CC)_{\nu_\tau} = -78 \pm 66 \text{ evts/ton}/10^{20} \text{ POT } E_\nu > 20 \text{ GeV}$$

where a factor of 1.45 has been used to correct for the difference in solid angle between BEBC and CHARM.

Together with the muon flux measurements described here, this leads to:

$$BR(\pi^0 \to \nu_\tau \bar{\nu}_\tau) = (-2.05 \pm 1.79) \cdot 10^{-6}$$

or

$$BR(\pi^0 \to \nu_\tau \bar{\nu}_\tau) < 2.31 \cdot 10^{-6} \quad 90\% \text{ C.L.}$$

and for the sum:

$$\Sigma_{e,\mu,\tau} BR(\pi^0 \to \nu\bar{\nu}) < 6.5 \cdot 10^{-6} \quad 90\% \text{ C.L.}$$

This is an improvement over the existing limit ($2.4\ 10^{-5}$ [65]) but does not probe values realistically expected.

REFERENCES

[1] P. A. Aarnio, A. Fasso, H. J. Moehring, J. Ranft and G. R. Stevenson, Fluka86 users guide, CERN TIS-RP/168 (1986)

[2] P.Fritze et al. (ABCLOS Collab.): Phys. Lett. B96 (1980) 427

[3] H. Abramowicz et al. (CDHS Collab.): Z. Phys. C13 (1982) 179

[4] M. Jonker et al. (CHARM Collab.): Phys. Lett. B96 (1980) 435

[5] L. B. Okun, leptons and quarks, North Holland 1982

[6] G. t' Hooft, Nucl. Phys. B35 (1971) 167

[7] I. J. R. Aitchison and A. J. G. Hey, gauge theories in particle physics, A. Hilger 1982

[8] P. D. B. Collins and A. D. Martin, hadron interactions, A. Hilger 1984

[9] G. Giacomelli and M. Jacob, Physics at the CERN ISR, Phys. Reports 55 (1979) 1

[10] B. L. Combridge, Nucl. Phys. B151 (1979) 429

[11] F. Halzen, 21eme conference internationale de physique des hautes energies, Paris 1982

[12] D. W. Duke and J. F. Owens, Phys. Rev. D30 (1984) 49
E. Eichten et al., Rev. Mod. Phys. 56 (1984) 667

[13] R. Ammar et al., Phys. Lett. B 183 (1987) 110

[14] G. Anzivino et al., Nucl. Phys. B (Proc. Suppl.) 1B (1988) 55

[15] P. Chauvat et al., Phys. Lett. B 199 (1987) 304

[16] P. Coteus et al., Phys. Rev. Lett. 59 (1987) 1530

[17] A. N. Aleev et al., Z. Phys. C 37 (1988) 243

[18] S. Barlag et al., ACCMOR Coll., Z. Phys. C 39 (1988) 451

[19] J. R. Cudell, F. Halzen and K. Hikasa, Phys. Lett. 175B (1986) 227

[20] S. J. Brodsky et al., Phys. Rev. D23 (1981) 2745

[21] T. D. Lee, particle physics and introduction to field theory, Harwood 1981

[22] H. Albrecht et al., DESY report 87-079 1987 on $B^0 \rightarrow D^{*+} l^+ \nu$

[23] H. H. M. Heijne, Muon flux measurement with silicon detectors in the CERN neutrino beams, CERN 83-06

[24] F. Bergsma et al. (CHARM Collab.): Phys. Lett. B157 (1985) 458

[25] A.N. Diddens et al. (CHARM Collab.): Nucl. Instr. Meth. 176 (1980) 189

[26] S. Cittolin, B. G. Taylor, CAVIAR manuel, CERN DD/OC/GA/80-2

[27] M. Jonker et al., Nucl. Instr. and Meth. 215 (1983) 361

[28] M. Atac, A. V. Tollestrup and D. Potter, Nucl. Instr. and Meth. 200 (1982) 345

[29] J. B. Lindsay et al., Nucl. Instr. and Meth. 156 (1978) 329

[30] ESONE commitee, EURATOM EUR 4100D (1969)

[31] M. Regler, Acta Phys. Austr. 4 (1978); R. Fruhwirth, CERN-DD/77/23 (1977)

[32] J.V. Allaby et al. (CHARM Collab.): Phys. Lett. B179 (1986) 301

[33] H. Grassler et al.: Nucl. Phys. B273 (1986) 253

[34] P. Debu, Results from the CDHS beam dump experiment, seminar given at CERN 11 march 1986.

[35] R.C. Ball et al.: Phys. Rev. Lett. 51 (1983) 743; M.E. Duffy et al.: Phys. Rev. Lett. 52 (1984) 1865; 55 (1985) 1816; 57 (1986) 1522

[36] R. Voss, charged lepton interactions, proc. Lepton and Photon interactions '87 Hamburg 581

[37] M. Holder et al., Nucl. Instr. Meth. 148 (1978) 235

[38] J.G.H. de Groot et al., Z. Phys. C1, 143 (1979); M. Heagy et al., Phys. Rev. D 23, 1045 (1981).

[39] J. V. Allaby et al., (CHARM Collab.), proposal of future studies of prompt neutrino production in 400 GeV proton nucleus collisions, CERN/SPSC/80-31

[40] Proposal to the SPSC Lepton Production CERN-SPSC/83 51 (1983)

[41] M. Talebzadeh et al.: Nucl. Phys. B291 (1987) 503

[42] C.H.Albright and R.E.Shrock, Signals for tau neutrino interactions in a beam dump experiment, Fermilab-Pub-78/97-THY

[43] E. di Capua et al.:Phys. Rev. B133 (1964) 1333; D.A. Bryman et al.: Phys. Rev. D11 (1975) 1337; Phys. Rev. Lett. 50 (1983) 7

[44] M. Jonker et al.: (CHARM Collab.): Phys. Lett. B107 (1981) 241

[45] F.Bergsma et al.: (CHARM Collab.): Phys.Lett. B147 (1984) 481

[46] L.A.Ahrens et al.:Phys.Rev.Lett. 55 (1985) 1814

[47] B.Naroska: proceedings of the international symposium on lepton and photon interactions at high energies, Ithaca, 1983. D.G.Cassel, L.Kreinick (eds.), p.96. Cornell Univ.,Ithaca NY,1983.

[48] M.Jonker et al.(CHARM Collab.): Phys. Lett B99 (1981) 265; J.V.Allaby et al.(CHARM Collab.): Phys. Lett. B177 (1986) 446; Z. Phys. C-Particles and fields 36 (1987) 611

[49] J.D. Bjorken, S. Weinberg: Phys. Rev. Lett. 38 (1977) 622

[50] H. J. Mohring, Hadron-nucleus inelastic cross-sections for use in hadron-cascade calculations at high energies, CERN/TIS-RP 116 (1983)

[51] C. H. M. Nieuwenhuis, A study of the interactions of high energy electron-neutrinos, Ph.D-thesis, University of Amsterdam 1986

[52] G. G. Henry, Measurement of inclusive low mass muon pair production by 225 GeV/c proton and charged pion beams with a large acceptance spectrometer, Ph.D-thesis, University of Chicago 1978

[53] V.A. Viktorov, Sov. Journ. of Nucl. Phys. 32 (1980) 520

[54] R.I. Dzhelyadin et al., Phys. Lett 94B (1980) 548

[55] R.I. Dzhelyadin et al., Phys. Lett 102B (1981) 296

[56] J.J.J. Kokkedee, The quark model, New York, Benjamin 1969

[57] M. Diakonou et al. Phys. Lett. 89B (1980) 432; T. Akesson et al. Z. Phys. C18 (1983) 5; G. J. Donaldson et al. Phys. Rev. Lett. 40 (1978) 684; C. Kourkoumelis et al. Phys. Lett. 84B (1979) 271, 277

[58] F. W. Busser et al. Phys. Lett. 55B (1975) 232, NPB106 (1976) 1; B. Alper et al. Nucl. Phys. B100 (1975) 237; A. L. S. Angelis et al. Phys. Lett. 79B (1978) 505

[59] J. Bartke et al. Nucl. Phys. B118 (1977) 360; T. Akesson et al. Nucl. Phys. B203 (1982) 27; K. Bockmann et al. Nucl. Phys. B140 (1978) 235

[60] G. J. Bobbink et al. Nucl. Phys. B217 (1983) 11; H. Kichimi et al. Phys. Rev. D20 (1979) 37; D. Drijard et al. Z. Phys. C9 (1981) 293

[61] A. Breakstone et al. Z. Phys. C21 (1984) 321

[62] Marshak, Riazuddin, Ryan, theory of weak interaction in particle physics, New York Wiley-interscience 1969

[63] R.D. Field and R.P. Feynman, Nucl. Phys. B136 (1978) 1

[64] B. Anderson and G. Gustafson, preprint LU TP 82-5 (Lund)

[65] P. Herczeg, C.M. Hoffman, Phys. Lett. B100 (1981) 347

[66] K. de Winter, CHARMII Coll.,Nucl. Instr. Meth. A278 (1989) 670

[67] CHARMII Collab., ITEP, Berlin-Zeuthen, Detection of the tau neutrino at the UNK, letter of intent (1989)

[68] A.N.Diddens et al.,CHARM Coll., Nucl. Instr. Methods 178 (1980) 27

[69] M.Jonker et al., Nucl. Instr. Methods 215 (1983) 361

[70] J.Dorenbosch et al.(CHARM Collab.), Nucl. Instr. Meth. A253 (1987) 203

[71] J.Dorenbosch et al.(CHARM Collab.), Z.F.Phys. C 40 (1988) 497

[72] M.Jonker et al. (CHARM Collab.), Phys. Lett. 102B (1981) 67 and Phys. Lett. 109B (1982) 133.

[73] F.Bergsma et al. (CHARM Collab.), Phys. Letters 99B (1981) 265, J.V.Allaby et al. (CHARM Collab.), Phys. Lett. 177B (1986) 446

[74] P. Weilhammer, Review of recent experimental results on hadroproduction of heavy quarks, XVIII International Symposium on Multiparticle Dynamics, Tashkent, 8-12 September 1987

[75] J. L. Ritchie et al., Phys. Letters 126B (1983) 499

[76] J. L. Ritchie et al., Phys. Letters 138B (1984) 213

[77] R. E. Shrock and M. Suzuki, PRE 25461

[78] W.Bacino et al., Phys. Rev. Letters 43 (1979) 1073

[79] The ν-spectrum in the D-rest frame , calculated by Altarelli et al. [84], can be parametrized as: $1/\Gamma_{tot}\partial\Gamma/\partial x = 21.24x^{2.3}(1-1.13x)$ for $0<x<0.885$ and $=0$ for $0.885<x<1$, where $x=2E_\nu/M_D$. This gives a mean x–value of 0.551 and a maximum at $x=0.617$. Duffy et al. [89] use: $1/\Gamma_{tot}\partial\Gamma/\partial x = 229.6x^{3,4}(1-0.943x)^{3.6}$ with a mean x of 0.519 and maximum at 0.515, which is the spectrum of the charged lepton [78]. However due to the V–A character of the weak interaction, the neutrino-spectrum is harder than the charged lepton spectrum in the β-decay of the c-quark.

[80] J.F.Gunion, Phys. Letters 88B (1979) 150

[81] M.Aguilar-Benitez et al., Phys. Lett. B 189 (1987) 476

[82] M.Aguilar-Benitez et al., Phys. Lett. B 199 (1987) 462

[83] M.Aguilar-Benitez et al., Z. Phys. C 31 (1986) 491

[84] G.Altarelli, N.Cabibbo, G.Corbo, L.Maiani and G.Martinelli, Nucl. Phys. B208 (1982) 365
[85] J. V. Allaby et al. (CHARM coll.), Phys. Lett. B 231 (1989) 317
[86] This number is calculated by taking the $D^{\pm}/D^{0}$-rates from [81] and the semi-leptonic branching-ratios for $D^{\pm}$ and D^{0} from [93].
[87] D.S.Barton et al., Phys.Rev. D27 (1983) 2580
[88] M.E.Duffy et al., Phys. Rev. Letters 55 (1985) 1816
[89] M.E.Duffy et al., Phys. Rev. Letters 57 (1986) 1522
[90] R.Odorico, Nucl. Phys. B209 (1982) 77
[91] W. Lohmann, R. Kopp and R. Voss, Energy loss of muons in the energy range 1-10000 GeV, CERN 85-03. R. Kopp, Messung des energieverlustes hochenergetischer muonen und vergleich mit vorhersagen einer simulationsrechnung, Ph. D.-thesis, University of Munchen 1985
[92] E.L.Berger, L.Clavelli and N.R.Wright, ANL-HEP-PR-82-32 (1982)
[93] Particle Data Group, Rev. of Part. Prop., Phys.Lett. 204B (1988)
[94] The systematic error in the result of Ritchie et al. coming from the extrapolation of the cross-section to $x_f = 0$ was not taken into account, because the experiment decribed here is also insensitive for Ds of $x_f < 0.1$.
[95] J. Ranft and S. Ritter, Z. Phys. C20 (1983) 347
[96] J. Ranft and S. Ritter, CERN internal report TIS-RP/IR/83-23 (1983)
[97] S. Ritter, Comp. Phys. Comm. 31 (1984) 393
[98] J. Ranft and S. Ritter, Z. Phys. C27 (1985) 569
[99] J. Ranft, Phys. Rev. D37 (1988) 1842
[100] A. Cappella and J. Tran Thanh Van, Phys. Lett. 93B (1980) 146
[101] H. Kirk et al.: Nucl. Phys. B128 (1977) 397
[102] J. Wetzig, K. Hanssgen, R. Kirschner, J. Ranft and S. Ritter, Leipzig preprint KMU – HEP 79-14 (1979); Comp. Phys. Comm. 31 (1984) 411
[103] A. E. Brenner et al., Phys. Rev. D26 (1982) 1497
[104] G. Jarlskog, L. Jonnsen, Monte-Carlo generation of multiple scattering, subroutine MLR, CERN computer centre program library.
[105] J. H. Dieperink, electronics for SEM beam monitors, CERN/SPS 24/9/73 internal report
[106] RTE – IVB programmers reference manuel HP 21MX, Hewlett Packard
[107] V. Goldansky, A. Kutsenko, M. Podgoretsky: Statistics of nuclear particle counting, Moscow: Physics-Mathematics Publishing 1959
[108] A. G. Frodesen, O. Skjeggestad, H. Tofte: Probability and statistics in particle physics, Bergen: Universitetsforlaget 1979
[109] V. Barger et al., Phys. Lett. 116B (1982) 357
[110] Bartel et al., Z. Phys. C33 (1987) 339
[111] G. Zacek et al., Phys. Rev. D 34 (1986) 2621

APPENDIX A

DESCRIPTION OF THE HADRON PRODUCTION MONTE CARLO

The Monte Carlo program applied in this experiment for the simulation of hadron production in 400 GeV p-Cu interactions is constructed around the routine NUCEVT written by J. Ranft and S. Ritter from the university of Leipzig [95], [96]. It uses a multi-chain fragmentation model, based on the Dual Topological Unitarization scheme [100].
The code NUCEVT is implemented in the general purpose program FLUKA [1], which also carries out the transport of the created particles through user-defined matter.

Here follows a short description of the hadron production mechanism, for more details see the publications of Ranft and Ritter.

1. A target nucleon is chosen according to the p,n contents of the target material. The target nucleon gets a Fermi-momentum between zero and $0.4 \cdot (N/A)^{1/3}$, distributed proportional to p_F^2, in which A = atomic weight and N = Z (atomic number) in case of a proton and N = A − Z in case of a neutron. A Lorentz transformation is made into the C.M. system of projectile and target particle.

2. The valence quarks of the two hadrons are split randomly in a quark and a di-quark in case of a baryon, and in a quark and an anti-quark in case of a meson. The momentum fraction of the single quark is selected according to the distributions $(1-x)^{5/2}/x^{1/2}$ in case of a baryon and $(1-x)^{1/2}/x^{1/2}$ in case of a meson. The di-quark of the baryon or the not-selected quark of the meson gets the remaining momentum fraction $1-x$. The quarks are assumed here to be massless.
Two colourless two-jet systems are formed (see fig.44).

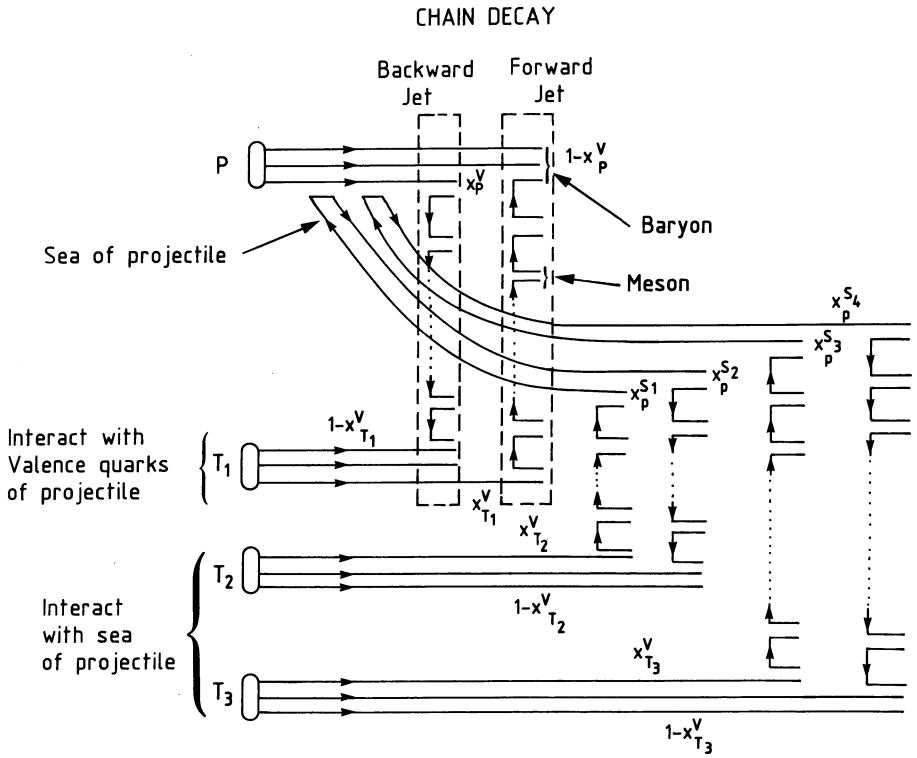

Figure 44: DTU mechanism in a baryon nucleus interaction. P represents the incoming baryon and T_1, T_2 and T_3 are three target nucleons taking part in the interaction. x^v and x^{Si} are valence- and sea-quark momentum fractions.

In case of baryon baryon interactions one two-jet system contains the di-quark of the projectile and the single quark of the target baryon (forward jet), the other one contains the di-quark of the target baryon and the single quark of the projectile (backward jet).
In case of meson baryon interactions one has: forward jet = single anti-quark from meson + single quark from baryon and backward jet = di-quark from baryon + single quark from meson.
Since the momentum fractions of quarks and di-quarks are selected, the invariant masses of the two-jet systems are exactly determined. A Lorentz-transformation is made in the C.M. frame of the two-jet system.

3. The quarks or di-quarks at the ends of the two-jet system create a colour field of increasing energy content as they move apart. When the field energy becomes high enough, a quark anti-quark pair can be created (see fig.44). One of the created quarks forms with the original quark or diquark a colourless hadron, the other one continues the chain-decay process. A small possibility of making a di-quark anti-di-quark pair exists, resulting in the creation of anti-baryons. Each jet gets one half of the total invariant mass. The chain-decay is carried out according to the following steps with the code BAMJET [97]:

   a. If the energy of the jet gets below a certain cutoff, the chain-decay is stopped, continue with point g

   b. A decision is made whether a quark anti-quark pair, or a di-quark anti-di-quark pair should be created. The probability for the latter is 4%.

   c. The flavours of the quarks to be created are chosen. For a quark anti-quark pair the probability for a $u\bar{u}$ or $d\bar{d}$ pair is $\approx$ 0.43, for an $s\bar{s}$ pair $\approx$ 0.14 (the creation of charmed quarks, which is foreseen in the original program, was switched off in order to make a more explicit study of charm production (see chapter 6)).

   d. The hadron formed by the incoming (di)quark and one of the created (di)quarks is classified as a member of an SU(3)-multiplet. A meson with $L=0$ is classified for 50% as pseudo-scalar and for 50% as vector, thus not proportional to $2j+1$, which would give 25% PS and 75% V, as suggested by quantum statistics and used in the original code. The reasons for this can be found in [63] and [64], data can be found in [59]. An attempt has been made to include also production of mesons with $L>0$, see below. In case of a $q\bar{q}$ meson a problem arises how to classify η and η'. It was assumed here that $\eta+\eta'=\pi^0$ and $\eta:\eta'=1:1$ (see 5.3.4. and [56]). Thus for mesons produced in the chain-decay the program gave: $\eta,\eta'=\pi^0=(\pi^+ + \pi^-)/2$ and $\omega=\rho^0=(\rho^+ + \rho^-)/2$, in agreement with data [59], [58].
   All baryons got assigned a spin 1/2, in contradiction with the original version of the program, because of the low production rate of Δ^{++} in p-p interactions [61].

   e. The momentum fraction $(1-\eta)$, taken away by the created hadron is sampled according to: $\rho(\eta)=1-a+2\cdot a\cdot\eta$ for mesons and $\rho(\eta)=\exp(-b\ \eta)$ for baryons, with $a=0.88$ [63] and $b = -3$.

   f. The transverse momentum distribution of the created particles was:

$$\rho(p_T)\propto p_T\cdot e^{-\alpha p_T^2}$$

   with $\alpha=3.3\pm.3$, taken from Kirk et al. [101].
   Back to point a.

   g. The remaining quarks undergo a two-body decay, the momenta and flavours of the decay products are chosen such that, together with the produced particles in the forward and the backward jets, one has an overall conservation of energy, momentum and flavour.
   A Lorentz transformation is made back to the C.M. frame of the total system.

4. For the strong decay of the produced unstable resonances like η, η', ρ, ω, K^* etc. the code DECAY [102] is used, which uses decay rates of [93] or, if no accurate data available, symmetry rules. In three body decays uniform occupation of phasespace is assumed. A Lorentz transformation is made back to the lab system.

5. Hadron nucleus reaction are simulated as follows: before a hadron−hadron interaction is started with one of the nucleons and the projectile according to the preceding points, a small part of the energy of the projectile is used to create collisions of $q\bar{q}$-pairs out of the sea of the projectile with nucleons of the target, see fig.44. The average amount of collisions inside the nucleus $\bar{\nu}$ is given by: $\bar{\nu} = A \cdot \sigma_{inel}(h-h)/\sigma_{inel}(h-A)$ and the x distribution of the sea is taken as $\rho_{sea}(x) \propto (1-x)^4/x$. As flavours for the sea only u and d are used. This model makes hadron nucleus reactions look similar to hadron−hadron interactions with reduced x-scale, except at very low x-values. This seems to agree with data [87] and is explained by the fact that the fragmentation happens mainly outside the nucleus, because this is a low Q^2 process, which takes place on a relatively long time scale.
In this experiment the contribution of the low energetic secondary chains to the neutrino flux will not be seen, the only important thing is the amount of energy taken from the projectile. This amount will be adjusted to equalize the generated conventional muon flux with the measured one (see below).

The inelastic cross-sections for hadron nucleus interactions are taken from [50].
An attempt was made to include production of mesons with $L > 0$, to study the effect on the prompt muon flux (see section 5.3.3.). From measurements [60] it follows that the amount of $L > 0$ mesons could be as high as 20 % off all directly produced mesons. Only the production of $L = 1$ mesons are taken into account and it was assumed that the amount of mesons with $L > 1$ can be neglected. The considered $L = 1$ mesons are given in table 33.

Table 33: $L = 1$ mesons used in Monte Carlo simulation of prompt muon flux.

$2S+1L_J$	J^{PC}	I = 1	I = 0	I = 1/2
$^1P_1$	1^{+-}	$b_1(1235)$	$h_1(1170)$	$K_1(1270)$
$^3P_0$	0^{++}	$a_0(980)$	$f_0(975)$	$K_0^*(1430)$
$^3P_1$	1^{++}	$a_1(1260)$	$f_1(1285)$	$K_1(1400)$
$^3P_2$	2^{++}	$a_2(1320)$	$f_2(1270)$	$K_2^*(1430)$

The decay channels and branching ratios have been taken from [93], if measured, or otherwise symmetry rules were used. The production rate was taken proportional to $2J+1$. It was assumed that $f_0(1400)$, $f_1(1420)$ and $f_2'(1525)$ are pure $s\bar{s}$ states with a low production probability and they were neglected.

With the above described scheme one gets the following general features of the program:

1. Conservation of energy and momentum

2. Conservation of quantum numbers

3. Direct production of hadrons before strong decay, all knowledge on resonance decay included, transverse momentum generated before decay.

4. Pion to kaon ratio governed by only one parameter, good agreement with measurements (see below).

5. For direct production rates: $\pi^0 \approx (\pi^+ + \pi^-)/2$ and $K^0 \approx (K^+ + K^-)/2$.

A.1 COMPARISON WITH DATA

For comparison of this Monte Carlo program with measurements see [95], [98], [99]. The conclusion is that agreement with data is good, especially in the region of $x_f \leq 0.4$.
For this experiment it is important that the pion to kaon ratio is correct and, to a lesser extent, that the ratio of opposite charges for pions and kaons is in agreement with data.
These properties have been tested by comparison with 175 GeV hadron-hydrogen data from the Fermilab Single Arm Spectrometer [103] covering a kinematic range of $0.12 < x < 1$ and $0 < p_T < 1.25$ GeV/c. These data have been selected because of the large p_T range covered, which made it possible to integrate over p_T. In table 34 the K/π-ratio of experiment and Monte Carlo are given.

Table 34: Comparison of π/K-ratio from Monte Carlo with data.

Monte Carlo simulation			
	K^+/π^+	K^-/π^-	$(K^- + K^+)/(\pi^- + \pi^+)$
all	0.098	0.085	0.108
$x_F \geq 0.08$	0.130	0.117	0.124
$x_F \geq 0.12$	0.131	0.114	0.125
$x_F \geq 0.20$	0.132	0.097	0.119
Data 175 GeV p-p [103]			
	K^+/π^+	K^-/π^-	$(K^- + K^+)/(\pi^- + \pi^+)$
$x_F \geq 0.12$	0.122±0.19		0.118±0.015
$x_F \geq 0.20$	0.150±0.011	0.104±0.014	0.134±0.009

An error of 10% on the strange quark production rate is assumed.
The π^+/π^--ratio as function of x_F for the Monte Carlo was $R = 1.06 + 2.31 \cdot x_F$, whereas the data gave $R = 1 + 3.0 \cdot x_F$. For kaons these ratios were resp. $R = 1.25 \cdot (1 - x_f)^{-1.73}$ and $R = 1.25 \cdot (1 - x_f)^{-2.62}$. A correction as function of x_F was applied on the final produced pions and kaons to make the Monte Carlo +/− ratio in agreement with the data.

A.2 ADJUSTMENT TO MUON FLUX

The "raw" Monte Carlo generated a conventional muon flux already close to the measured one. To get complete agreement between generated muon flux and measured muon flux an adjustment was carried out in two steps:

1. The amount of energy taken from each hadron to simulate the intra-nuclear cascade (see above) was adjusted to get the right muon flux in pit 2. Pit 2 can be reached by muons with energy above ≈ 40 GeV, which are the most significant for the associated neutrino flux in the CHARM detector. On average 7.3 % of energy from a baryon and 4.9 % from a meson had to be taken to reduce the generated muon flux in pit 2 by 16 %.

2. After this adjustment the generated muon flux in pit 3,4 and 5 was still to high by resp. 5 %, 10 % and 25 %, and too low by a factor 1.3 in pit 1. This last disagreement was eliminated by correcting the weight of each generated muon by a factor which depended on the energy of its parent. This correction factor, as function of parent energy, is shown in fig.45.

Above corrections were also applied in generating the neutrino flux.

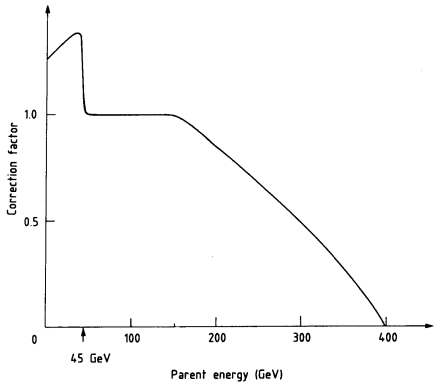

Figure 45: Correction factor applied to muon-parent energy.

Whereas the first step has some theoretical justification, the second step is just brute force. However, the large correction at $x_F < 0.1$ affects the neutrino flux in the CHARM detector only below 20 GeV by 20%, the correction at high x_F decreases the neutrino flux above 80 GeV by only 3 %. The shape of the correction curve in fig.45 probably indicates that the nuclear effects, described above, are underestimated by the program.

APPENDIX B

MUON FLUX MEASUREMENTS

The muon flux measurements in the gaps of the iron shield behind the target were used for:

1. Fine adjustment of conventional neutrino flux Monte Carlo.
2. Determination of the leakage of the density 1/3 target
3. Tests on the extrapolation method
4. Comparison of prompt muon flux with the charm production model

The layout of the muon shield is given in fig.16 and table 35.

Table 35: Longitudinal dimensions of muon shield, numbers taken from Heijne [23].

OBJECT	LOCATION [m]	MATERIAL
target	0	3.025 m copper $\rho = 8.96$ gr/cm^3
airgap	3.025	
catcher	3.050	3.025 m copper $\rho = 8.96$ gr/cm^3
airgap	6.075	
shield	7.72	4.02 m iron $\rho = 7.3$ gr/cm^3
pit1	11.74	
SSD plate	13.89	
shield	14.39	20.52 m iron $\rho = 7.3$ gr/cm^3
pit2	34.91	
SSD plate	35.39	
shield	35.89	20.15 m iron $\rho = 7.3$ gr/cm^3
pit3	56.04	
SSD plate	56.59	
shield	57.09	20.57 m iron $\rho = 7.3$ gr/cm^3
pit4	77.66	
SSD plate	78.09	
shield	78.59	24.23 m iron $\rho = 7.3$
pit5	102.82	
SSD plate	103.22	
magnet	104.84	10.0 m iron $\rho = 7.8$ gr/cm^3
airgap	114.84	
shield	119.94	8.45 m iron $\rho = 7.3$ gr/cm^3
pit6	128.39	
SSD plate	128.99	
remaining shield	129.49	91.06 m iron $\rho = 7.3$ gr/cm^3 $\approx$ 150 m of earth
total 199 m of iron and $\approx$ 150 m of earth		

The minimum momentum a muon should have to reach pit 1, 2, 3, 4 or 5 was respectively about 10, 37, 67, 103 and 143 GeV/c. The probability for a muon to reach pit 2 as function of its momentum is shown in fig.46. For the other pits this figure looks similar, but the slope becomes less steep as the pit number increases.

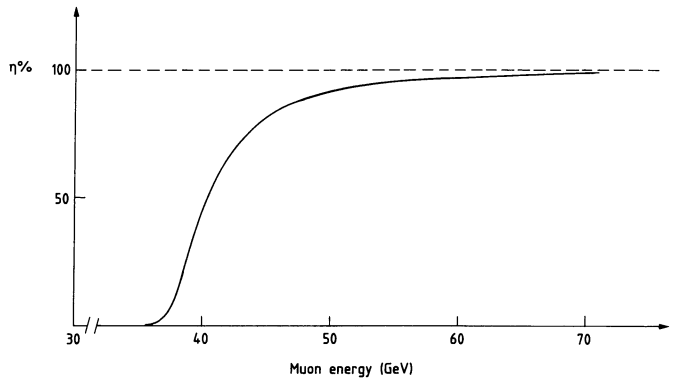

Figure 46: Probability for a muon to reach pit 2.

The muon flux was measured every machine burst by solid state detectors (SSD). These detectors were mounted on a plate, shown in fig.47, which was centered on the beam axis.

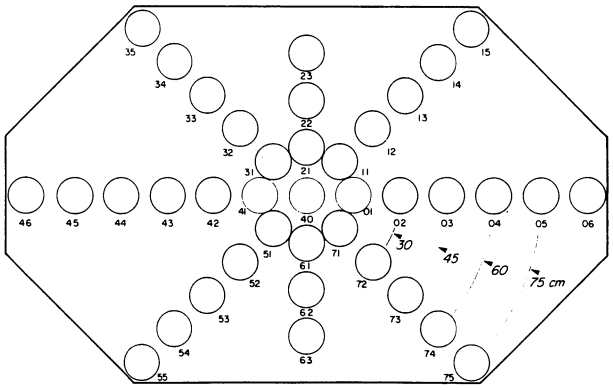

Figure 47: SSD plate.

Not all places were occupied in the outer rings. Normally the center position and rings at 15 and 30 cm were filled, plus one radius until 60 cm. In each gap a calibration box, mounted on a lift, with five SSDs of different sensitivity could be moved laterally to the beam axis to any position with $r \leq 90$ cm. These boxes were used to make a relative calibration of the sensitivity of the SSDs in a pit and to make continuous scans of the muon flux profile. One special calibration box, which could be mounted in front of the permanent calibration boxes, was moved from pit to pit in order to intercalibrate the SSDs in different pits. Absolute calibration was obtained by track counting in photographic emulsion [23] and, for this experiment, by scintillation telescopes (see app. C).

The information of the fixed detectors and movable calibration boxes have been used to reconstruct the lateral profile of the muon flux in each pit. The profile could be well described by the function:

$$\Phi_\mu(r) = \exp(A_1 - (A_2 + A_3 \cdot r^2)^{1/2}) \tag{83}$$

where A_n are constants and r = distance from beam axis. Equation (83) implies that the flux profile asymptotically goes as the exponential $A \cdot \exp(-A_3^{1/2} \cdot r)$. The shape (83) could be reproduced by Monte Carlo simulation, using the program described in appendix A for the production of muons, a program of Kopp et al. [91] for the energy loss of muons in matter and the routine MLR [104] for the multiple scattering of muons based on the theory of Moliere. The total μ-flux was obtained by integrating over the reconstructed profile. For example, the μ-flux in pit 2 was measured up to a radius of 60 cm, which covered 76% of the total flux, the remaining 24% relied on the profile shape generated by Monte Carlo for which a systematic error of 1.1% of the total was taken into account.

For pit 2, 4 and 5 the absolute calibration of the SSDs was performed with the help of scintillation counters (see appendix C). In pit 1 and 3 the absolute calibration relied on track counting in nuclear emulsion, which had a higher systematic error, because of uncertainties inherent to this method (see [23]). For pit 3 the error on the absolute calibration was set to 15 %. In pit 1 the emulsion calibration had an error of only 10% because of a lower background of delta-rays in the emulsion. This lower background was due to the 2.15 m free space between the iron shield and the SSDs in pit 1, whereas in pit 3 the free space was only 55 cm.

Before calculating prompt and conventional μ-flux in a certain pit by extrapolation with the help of data from the density one and density one-third target, a correction had to be made for the different amount of absorber for the two targets. As described in section 3.2 , the density one and density one half target had respectively 2 m and 1 m of copper more than the density one-third target. The correction was calculated with the help of μ-flux data recorded during special runs with the 3 m long catcher (see fig.15), also made of copper, moved out of the beam. Before extrapolation, the density one flux was multiplied by a factor $R_{io}^{2/3}$, where R_{io} stands for the ratio (flux with catcher out)/(flux with catcher in) and the exponent of 2/3 is there because one has to correct for a difference of only 2 m of copper (see fig.50). In table 36 the integrated μ-flux in pit 1 to 5 is given for the three target densities, together with the catcher out/in ratios.

Table 36: Measured muon flux.

flux in $\mu/10^7$ proton					
density	PIT1 ±10.3%	PIT2 ±2.4%	PIT3 ±15.4%	PIT4 ±3.7%	PIT5 ±5.2%
ρ = 1	8.20 10^3	655	137	33.1	6.10
ρ = 1/2	16.5 10^3	1026	202	47.4	8.66
ρ = 1/3	29.1 10^3	1498	280	65.6	11.6
catcher out/in-ratios					
density	PIT1 ±2%	PIT2 ±1%	PIT3 ±1%	PIT4 ±2%	PIT5 ±2%
ρ = 1	1.96	1.39	1.34	1.31	1.31
ρ = 1/2	2.37	1.43	1.37	1.35	1.35
ρ = 1/3	4.12	1.69	1.53	1.47	1.44

In table 37 the extrapolated conventional and prompt μ-flux for each pit is given, calculated for the equivalent amount of absorber of the density one-third target. Error sources taken in account are: absolute calibration, integration over flux profile, catcher out/in ratio.

Table 37: Prompt and conventional muon flux from extrapolation.

flux in $\mu/10^7$ proton					
	PIT1	PIT2	PIT3	PIT4	PIT5
prompt	$(3.4\pm0.7)10^3$	476±13	110±17	28.7±1.1	5.5±0.3
conventional	$(8.8\pm1.1)10^3$	341±9	57±9	12.3±0.6	2.1±0.1

In fig.48 the measured muon flux in the gaps of the iron shield is given as function of threshold energy.

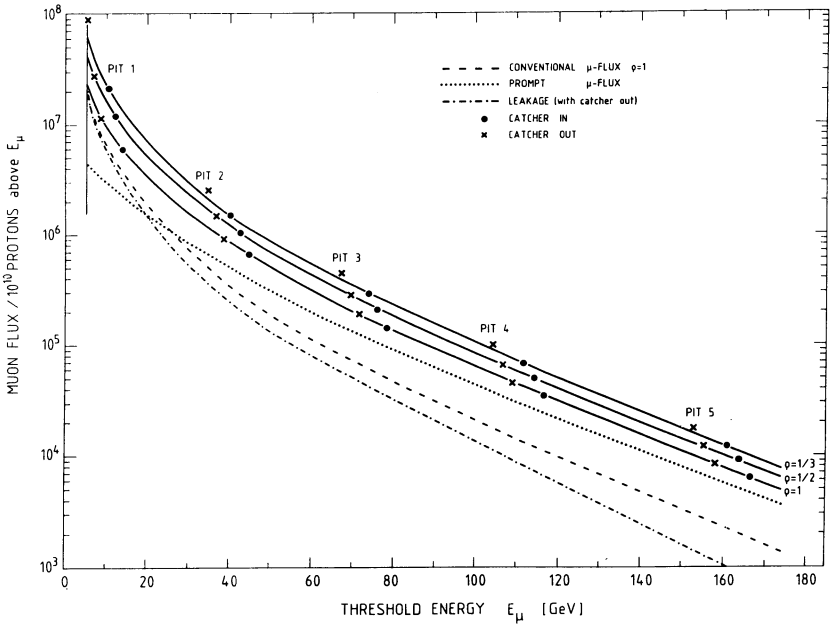

Figure 48: Measured muon flux as function of muon range in iron for pit 1-5.

To test the extrapolation method, in fig.49 the μ-flux for all three target densities is plotted as function of (density)$^{-1}$, normalized to the density one-third rate and corrected for the same amount of absorber.

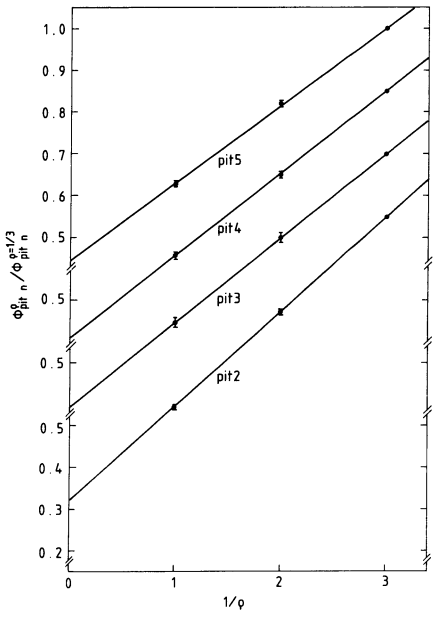

Figure 49: Test on extrapolation method using three target densities (for explanation see text).

From a straight line fit through the three points for all pits it is concluded that the uncertainty in the density-one target is less than 0.5 %.

The density one-third target had a length of about six proton interaction lengths. Thus, part of the hadrons will leak into the catcher with density one. As a result the conventional flux given in table 37 is created by the decay of hadrons, produced in the first meter of copper and the "prompt" flux of table 37 still contains a small fraction of conventional flux, created by decaying hadrons leaking out of the first meter of copper. The amount of leakage is defined by the ratio α = (conventional flux produced by hadrons outside the first meter of copper)/(conventional flux produced by hadrons within the first meter of copper). The factor α could be determined by using the data of the special runs with target density one-third and the catcher moved out of the beam line (see fig.15). The hadrons leaking out of the density one-third target have in that case a 470 cm free decay path, which will amplify their μ-flux yield by a factor $470/\lambda_{hadron}$. Thus one has (see fig.50):

$$\alpha' = \lambda/470 \cdot 2[R(1/3) - R(1/2)]/[R(1/2) - R(1)^{5/3} \cdot \Phi(1)/\Phi(1/3)] \qquad (84)$$

in which $R(1/n)$ = catcher out/in ratio for target density $1/n$; $\Phi(1/n)$ = flux for target density $1/n$; λ = average interaction length of hadrons $\approx$ 18 cm. The density one-half catcher out/in-ratio is used to estimate the density one-third point without leakage. In equation (84) α-prime is used, because it is the leakage only for the hadrons created in the first meter of copper, not for the ones which are produced after one meter by a leaking hadron. The total leakage was determined by Monte Carlo, which was forced to yield the proper restricted leakage α' (see section 5.1.1.).

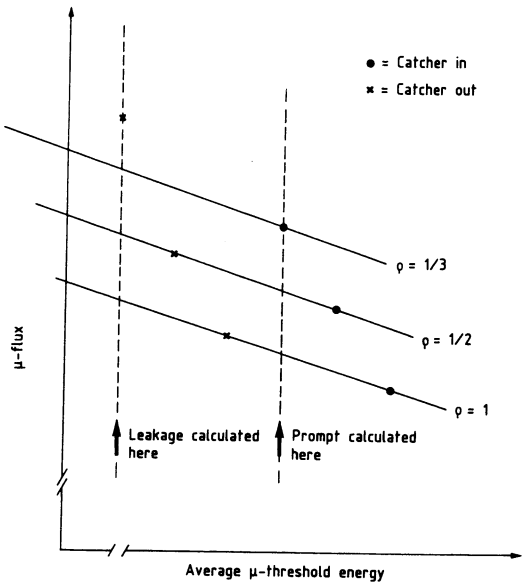

Figure 50: Correction for different amount of absorber before extrapolation.

APPENDIX C

ABSOLUTE CALIBRATION OF μ-FLUX DETECTORS IN SHIELD

C.1 INTRODUCTION

For checking the calculation of the conventional neutrino background an accurate knowledge of the muon flux in the iron shielding of the neutrino beam line was necessary. The muon flux was permanently monitored by silicon detectors, see Heijne [23], which had an excellent relative accuracy, but were hard to calibrate absolutely because of delta-ray background. So far the absolute calibration was carried out with the help of nuclear emulsions, but the accuracy obtained (see [23]) was not good enough for our needs. For this reason a muon flux measurement was performed with scintillation counters mounted on the movable supports in the gaps of the muon shield.
To reduce the muon rate the spill time was increased from 23 μs to ca. 100 ms and the beam intensity lowered by a factor of ca. 20. For normalization a secondary emission grid was used. The beam configuration during the beam dump experiment (no pulsed magnets after the extraction and last active element 400 m before the target) was favourable for a precision flux measurement.

C.2 DESIGN OF MUON TELESCOPE

The telescope consisted of two parallel square scintillators of 1.2 cm^2 size, spaced by 5 mm, shielded against delta-rays with 15 mm tungsten and looked at by two small photomultipliers (see fig.51). The tungsten shielding was subdivided in a piece of 5 mm and 10 mm, as shown in fig.51, to avoid coincidences from muons which traverse only the upstream scintillator and create delta-rays in the tungsten which travers the downstream scintillator. To avoid accidental coincidences due to cerenkov light production by the high intensity muons and delta-rays, air light guides were used instead of plastic ones.

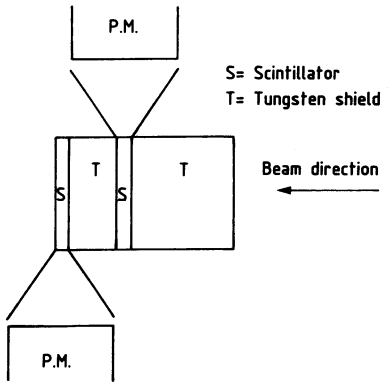

Figure 51: Muon telescope.

Coincidences caused by traversing muons were recorded.
For the geometrical acceptance of an angular distribution as expected in this experiment a Monte Carlo simulation gave an effective surface of 98% of the scintillator cross-section.

In order to check the tungsten delta-ray shielding and the efficiency of the telescope several tests were performed.
A measurement with and without tungsten shielding showed that the effect of delta-rays was of the order of 15%.

With the help of a multichannel analyzer the pulse height of the telescope was recorded when put in a muon beam of 1.8 sec spill length. It was found that the pulse height of a minimum-ionizing particle was well above discriminator threshold.

In order to check the effectiveness of the tungsten shield a 1.7 times scaled-up telescope was built and exposed together with the smaller one in muon beams under a variety of conditions. Because of the equal angular acceptance but different thickness of shielding a possible inefficiency would show up as a higher flux seen by the small telescope. This effect did not occur to an accuracy of 1%.

The pulseheight spectrum of the coincidences was compared with that of the singles, having the telescope under the same conditions as during the final measurements (pit2, beamdump, special low intensity, slow spill) and using a fast multichannel analyzer. Again it was seen that the pulses leading to coincidences were well above discriminator threshold.

The telescopes were placed in special boxes, designed by the CERN EF division, which could be mounted on the movable support that carried the calibration box in the pits of the iron shielding.
Telescopes were placed in pit 2, 4 and 5 with cross-sections of resp. 1 cm^2, 3.5 cm^2 and 3.5 cm^2.
For each telescope singles, coincidences and 100ns delayed coincidences were recorded.
In pit 2 measurements were carried out at 0, 15, 30, 45 and 60 cm from the beam axes, in pit 4 at 0, 30 cm and in pit 5 at 0 cm. The beam intensity was about 10^{12} protons per burst with a spill length of 100 millisec.

C.3 MEASUREMENTS

The correction for deadtime and accidental coincidences was derived from the contents of the delayed coincidences channel.[1] The maximum correction was 1% at a coincidence rate of 700 KHz during normalization with the SEM-grid (see below). The flux measurement was done at a rate below 200 KHz.
The ratio singles/coincidences was always smaller than 2.
The ratio delayed coincidences/coincidences was smaller than 0.06 .
In fig.52 the ratio of the telescope in pit 2 (tel2) and pit 4 (tel4) when both at beam axes is plotted against the rate of tel2.

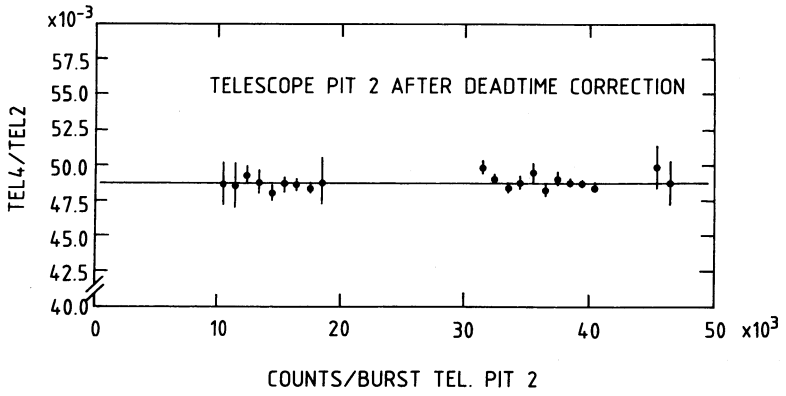

Figure 52: Rate dependence of the telescope in pit 2.

Because the rate of tel4 was low (< 30KHz) it was not affected by deadtime effects. From the straight line fit of fig.52 it follows that the applied correction was adequate.

---

[1] CORRECTION = (DELAYED COINCIDENCES)·(0.5 – R1·R2)/(1 + R1 + R2 + R1·R2)
R1,2 = (SINGLES – COINCIDENCES)/COINCIDENCES for channel 1,2

Because the BCTs did not work in the slow spill, a reliable fixed solid state detector (SSD) was needed which would be stable at low intensity and could be used for relative normalization. Comparing them with the telescope in pit 2, the upstream central SSD in pit 1 (further referred to as SSD28) and the SSD with the same position in pit 2 (further referred to as SSD68) were found to be stable to within 1% in the intensity range of the flux measurement.

C.3.1 ABSOLUTE NORMALIZATION

For the absolute muon flux determination the signal of the SSD used for normalization should be known as a function of protons per burst. Here a problem occurred. The ratio SSD28/SSD68 changed by 13 % in going from fast to slow spill. Also the two SSDs in the calibration box of pit2 (here called SSD78 and SSD79) changed sensitivity (see table 38). In order to overcome this problem another normalization was found using the secondary emission (SEM) grid in front of the dump (see fig.16). This SEM-grid was made of a horizontal and vertical array of 15 titanium strips of 3.5 mm width and 1.5 mm distance placed in a separate vacuum tank. The integrated signal of the strips showed the following behaviour:

1. Linear with BCT in fast spill (see fig.54)
2. Linear with telescope in slow spill (see fig.53)[2]
3. No change in signal over 2 months of running within 1% (table 39)
4. No change in signal before and after muon flux measurement in fast spill within 0.3%
5. No dependence on position of impact point and beam width during calibration runs.
6. The integration time at fast spill was already bigger than 200 ms. The signal was obtained by sampling the integrators at two points and subtracting, so rounding errors of the ADCs cancelled by taking enough statistics [105.]
7. Beam profiles in slow and fast spill were compatible.
8. The ratio vertical/horizontal of the SEM-grid was the same in slow and fast spill conditions.

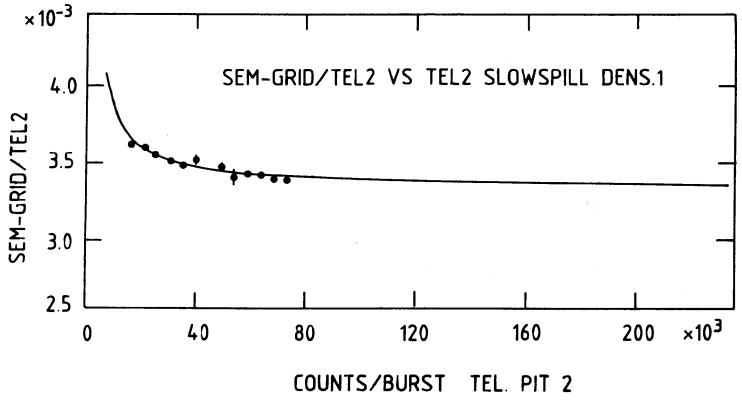

Figure 53: SEM-grid/tel2 versus tel2 in slow spill.

As one can see in fig.53 and 54, the signal of the grid had an offset of 0.36 cts. per channel caused by electronic noise and radioactivity of the environment. This offset did not change before and after the normalization by more than 5%, giving an error smaller than 0.5%. In table 40 the behaviour of some SSDs is given when

[2] The x-scale of fig.53 can be interchanged by the x-scale of fig.54

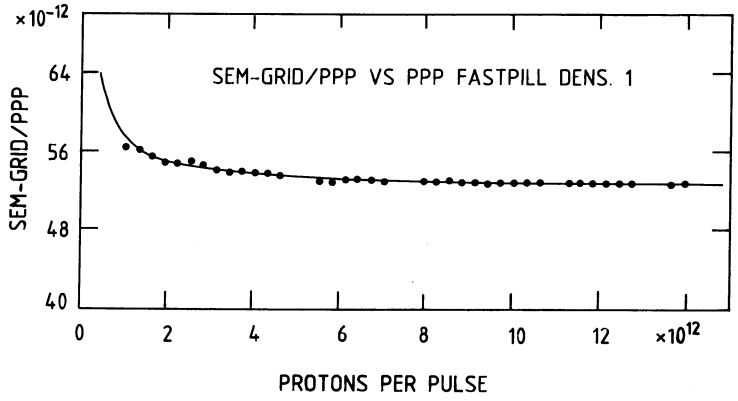

Figure 54: SEM-grid/BCT versus BCT in fast spill.

normalized with the SEM-grid. To obtain an absolute flux measurement the following procedure was applied:

1. SSD68 and SSD28 (upstream detector in resp. pit 2 and 1) were used for relative normalization because at typical intensity during slow spill their accuracy was better than that of the SEM-grid.

2. For spills with high intensity the SEM-grid was used to calibrate the telescope in pit 2 at central position (maximal intensity during slow spill was 1/4 of normal intensity at fast spill (fig.53 and 54))

3. During normal fast spill the SEM-grid was calibrated with the BCT in order to arrive at protons per pulse (see fig.54)

With this method the absolute muon flux given in table 41 was obtained.

C.4 CONCLUSIONS

If one compares the μ-flux measured by the telescope with the one derived from the SSD-measurements during fast spill operation given in table 41 one sees that:

1. The ratios of the fluxes within the same pit at different radii are the same within 5%

2. The SSD-fluxes are higher than the telescope-fluxes by a typical factor of 1.15

The conclusion is that the old SSD calibration was wrong.

Table 38: Change of some SSDs normalized to SSD68: fast spill/slow spill.

SSD28	1.13
SSD78	1.04
SSD79	0.95

Table 39: SEM-grid/BCT target density 1.

GRID/BCT		
DATE (1982)	(cts/10^{10} proton)	offset(cts)
	SPS-period 3B	
15/7	0.528	10.2
17/7	0.525	9.2
18/7	0.529	7.4
	SPS-period 4A	
5/8	0.526	2.9
18/8	0.522	5.1
21/8	0.523	5.3
	SPS-period 4B	
2/9	0.528	2.8
10/9	0.529	3.2
12/9	0.525	9.4

Table 40: Change of some SSDs normalized to SEM-grid: fast spill/slow spill.

SSD28	1.09
SSD68	1.23
SSD78	1.18
SSD79	1.29

Table 41: Muon fluxes obtained with telescopes and SSDs.

for TEL: rel. error 0.5% for SSD: abs. error 5% flux in $\mu/10^{10}$prot/cm2
abs. error 2%

DENS 1

	PIT 2			PIT 4			PIT 5		
RADIUS	TEL	SSD	RATIO	TEL	SSD	RATIO	TEL	SSD	RATIO
cm 0	132.6	152.1	1.15	2.63	2.97	1.13	0.327	0.394	1.21
15	99.74	115.1	1.15						
30	56.60	65.3	1.15	1.99	2.18	1.10			
45	29.45	34.0	1.15						
60	15.25	17.0	1.12						

DENS 1/2

	PIT 2			PIT 4			PIT 5		
RADIUS	TEL	SSD	RATIO	TEL	SSD	RATIO	TEL	SSD	RATIO
cm 0	207.6	237.0	1.14	3.76	4.24	1.13	0.464	0.551	1.19
15	156.0	177.9	1.14						
30	88.37	102.2	1.16	2.85	3.10	1.09			
45	46.37	53.2	1.15						
60	23.91	26.9	1.13						

DENS 1/3

	PIT 2			PIT 4			PIT 5		
RADIUS	TEL	SSD	RATIO	TEL	SSD	RATIO	TEL	SSD	RATIO
cm 0	304.0	347.5	1.14	5.20	5.78	1.11	0.624	0.766	1.23
15	226.5	258.5	1.14						
30	129.2	148.5	1.15	3.94	4.22	1.07			
45	67.90	77.2	1.14						
60	34.98	38.6	1.10	1.90					

APPENDIX D

DETERMINATION OF THE NUMBER OF INCIDENT PROTONS

The method of obtaining the prompt signal by extrapolation to infinite target density (see chapter 1) is very sensitive to an error in the event rates. E.g. a change of 1 % in the density one (1μ) rate above 20 GeV would give a change of 5 % in the prompt (1μ)-rate.
To be sure that the events registered on tape were normalized with the correct number of protons on target (POT) some checks were made.

The calculation of the total number of POT was carried out twice by different people: the first time the analysis was performed in parallel with the event reconstruction, the second time all raw data tapes were reprocessed only for the POT calculation, using software different to that used in the first pass.

Bursts were discarded if steering equipment was in the beam or if the loss monitors (see section 3.1) showed a too high rate. The loss monitors were calibrated with aluminum foils of different thickness and the cut applied was the equivalent of 1 % of the expected prompt neutrino rate.
In fig.55a a typical example of a distribution of proton loss rate is shown, as measured for individual bursts in one of the loss monitors, together with the applied cut.

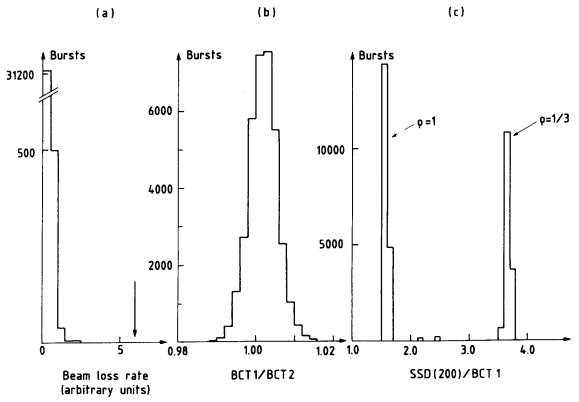

Figure 55: a: Proton loss rate in arbitrary units (the arrow indicates the threshold for rejection). b: Ratio of two BCT measurements. c: Ratio of a solid state detector and a BCT.

The amount of protons were registered with three beam current transformers (BCT, for positions see fig.14). These BCTs were compared with each other and gave always the same results within 0.2% at nominal beam intensity. In fig.55b the distribution of the ratio of two BCTs is plotted for about one half of the total running time.
The BCTs were also checked against the μ-flux in the pits of the iron shield measured by solid state detectors (see appendix B). From this check one could conclude that the BCTs were stable and that no runs with different target density were mixed, since the muon flux per POT depended on the target density. In fig.55c the distribution of the ratio of a solid state detector in pit2 and a BCT is shown.
The conclusion of the above tests was that the amount of protons given by the BCTs was accurate within 0.5%

.

The dead-time correction was calculated with three different methods which were to a large extent independent. The dead-time was derived most accurately from the signal of two small scintillation counters placed in gap 5 and 6 of the muon shield. The pulses of each of these counters were registered in two scalers: one was always enabled and the other was blocked if the trigger was not active because of the storage of an event. For the lifetime the ratio (blocked scaler)/(unblocked scaler) was taken. Since the muon flux was proportional to the amount of protons on target the counting rate of the scalers reflected the time structure of the proton intensity.

To monitor the stability of the method, the same procedure as above was followed with the signal of a 20 MHz clock. Of course the clock did not follow the proton intensity and small deviations from the first method are expected.
In addition to this method, the lifetime of the detector was calculated from the distribution of triggers per burst, independently of additional signals and timings. The lifetime was determined in this case from the deviation of the distribution of the number of events per burst from a Poisson distribution with the same mean value. This method is described in [107].

The lifetime measurements were simulated by Monte Carlo in order to check and monitor the experimental values. Input parameters for the simulation were: a spill length of 23 μs inside a beam gate of 33 μs; dead-time of the detector for an accepted event of 15 μs, 400 ns for a strobe and 200 ns for a veto plane hit; the average number of triggers, strobes and veto hits per proton; the average time dependent proton intensity of the spill, determined by recording the arrival time of triggers during the gate. The lifetime was simulated for each individual burst, using the real proton intensity as measured by the BCT.

In table 42 the lifetimes calculated by the different methods plus Monte Carlo results are given for a typical run.

Table 42: Comparison of different lifetime measurements.

lifetime	scintillator method	Poisson method	clock method
measured	0.768±0.006	0.764±0.008	0.784±0.005
Monte Carlo	0.774	0.764	0.783

As can be seen from this table, the scintillator and the Poisson method are in good agreement, the Monte Carlo simulation reproduces well all three experimental values. The lifetime given by the clock method is slightly higher than the other values because the clock rate was not proportional to the proton intensity. The final result of the analysis was an average lifetime of 86.4 % for the runs with the density one target and of 78.3 % for the density one-third target, with for both an uncorrelated error of 0.8% .

For safety reasons all scalers were also recorded in a 10 ms wide gate around the burst gate of 33 μs. Comparison of the counts from the above mentioned scintillators in the 10 ms gate and the burst gate showed that the burst gate had always the proper timing and no events were lost.

In fig.56 the event rate is given as function of run number over the full running period, separately for the runs with target density one and one-third.
The figure does not show any obvious systematic shift as function of time. In fig.57 the distribution of the deviation from the mean value of the event rate for individual runs is given, together with the expected Gaussian curve in case of random fluctuations.
Also a run-test [108] applied on the data of fig.56 showed perfect agreement with the hypothesis of random fluctuations of the individual rates around the mean value.

The final amount of protons on target was: (13.26 ± 0.13) 10^{17} for the density one target and (6.35 ± 0.07) 10^{17} for the density one-third target.

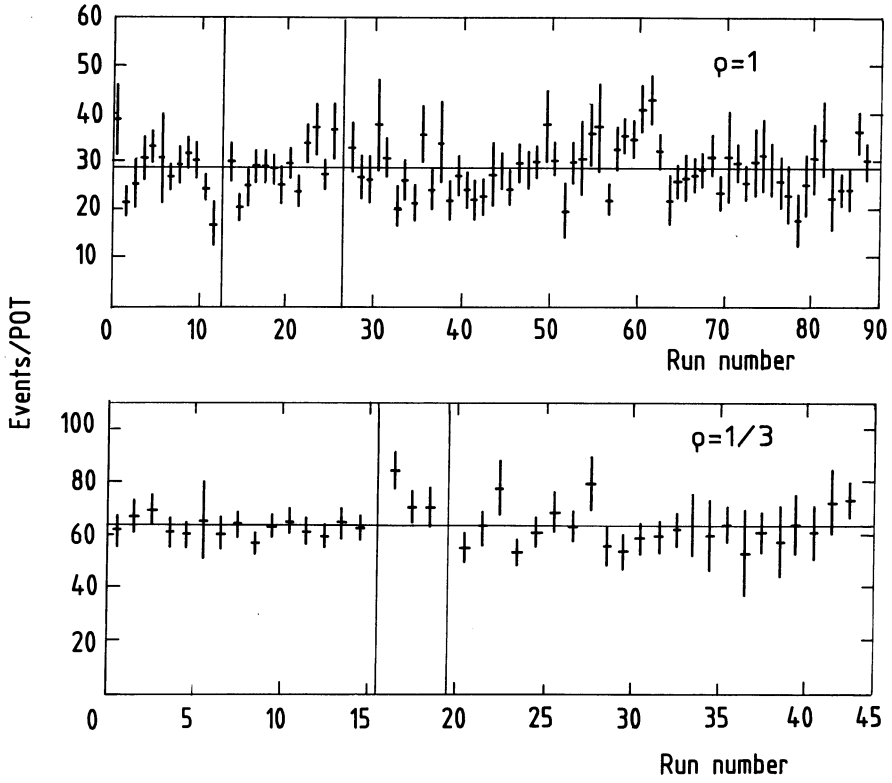

Figure 56: Event rate (arbitrary units) as function of the run number for two different target densities. The horizontal lines show the average rates; the vertical lines indicate the subdivision of data into three different running periods.

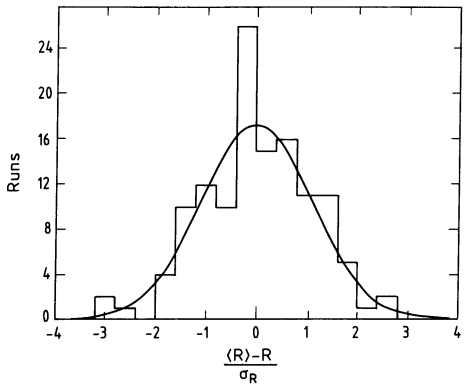

Figure 57: Distribution of the deviation of event rates of individual runs from the mean rate.

APPENDIX E

MEMORY ORGANIZATION OF MONITOR COMPUTER

Some addition to the standard software of the Hewlett Packard 21 MXE was made to cope with the large amount of data to be stored. In order to get information about the number of hits, mean pulse height and mean drift time of the proportional drift tubes and streamer tubes about 64k of fast memory was needed. Under the used operating system RTE-IVB [106] normal programs could address maximal 32k of memory, subdivided into 32 pages of 1k directly addressable by single instructions. To create a multi-tasking system these 32k of logical address space were mapped onto 32 pages of the maximal 1024 pages of physical memory, by means of 32 mapping registers.
A way of allowing arrays beyond the 32k normal program space was supplied by the RTE-IVB system in the creation of an Extended Memory Area (EMA). A program using this feature had to declare itself as an EMA-program and to specify the name of the common block (where only one was allowed) which would contain the large arrays. After loading of the program, a special EMA-segment of an integer amount (to be specified by the user) of pages was loaded at the top of the first page not already used by the program (see fig.58).

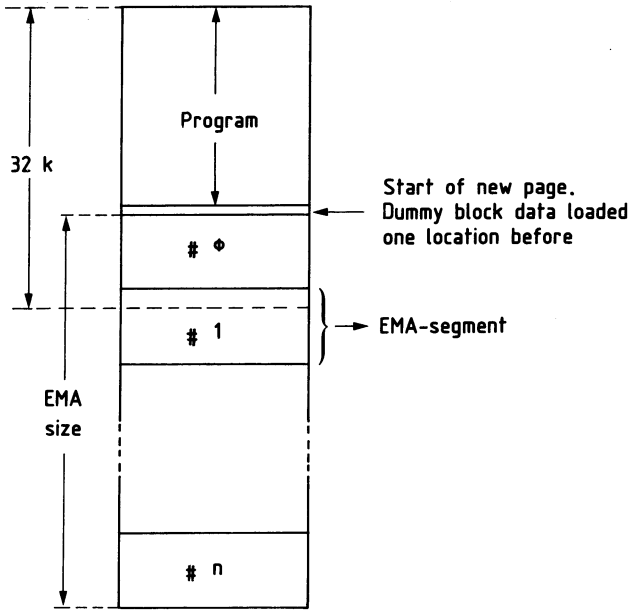

Figure 58: Extended Memory Area

Program plus EMA-segment had to be within the 32k of logical address space. By changing the mapping registers pointing to the EMA-segment during execution time, the EMA-segment could be mapped on the full extended memory area (see fig.58), giving the program access to it.
In its original form this feature was not useful for this experiment because:

1. It was slow: At every fetch from EMA the proper segment number was calculated, the segment mapped in and the address within the segment resolved.

2. EMA could not be shared among different programs.

Point one was overcome by doing the address and map book-keeping in the program itself. For this the system software had to be by-passed. This was achieved by loading at the last location of the last page used by the program a dummy block data of one element:

COMMON/EMASG/IDUMMY

By using in the program a common like:

COMMON/EMASG/IDUMMY,MSEG(1)

the EMA-segment could be directly accessed by means of the array MSEG. Changing of the segment to be mapped could be done with a routine supplied by the manufacturer. A special subroutine had been written to give any other program access to the data stored in EMA. The original EMA-program, which received events and stored the data in the EMA, was locked in memory, so that it could not be swapped out and the EMA was kept always at the same physical memory location. Another program, which wanted e.g. to display the mean PDT-pulse heights of a certain part of the detector, started as a normal program (with also a dummy common block as described before). When this program needed access to the EMA it called a subroutine which locked the calling program in memory and made it an EMA-program by changing the system tables. One had to enter in these tables the physical starting page of EMA, its size, the logical starting page of the EMA-segment (page whose first location coincided with MSEG(1) of the dummy common) and the number of pages of MSEG (not necessarily the same as that of the original EMA-program). Only during the short time of writing in the system tables the memory protection and interrupt had to be switched off. By this operation the display program had access to EMA in the same way as the original EMA-program. After the EMA-access had finished, the program changed itself back to its old status. In practice this procedure worked very well, it was fast and did not cause any trouble for other programs.

APPENDIX F

MATERIAL UPSTREAM OF THE DUMP

Table 43: Measured thickness of material in beam for neutrino beam dump experiment 1982.

Equipment	Material	Thickness [mm]	Effective thickness α [mm]	Absorption length λ [mm]	Loss α/λ	Distance to dumps [mm]
Ti beam window at downstream end of decay tunnel	Ti	0.100 ± 0.001	0.100	260	$3.8\ 10^{-4}$	771.5
Air gap	Air	102	102	$675\ 10^{3}$	$1.5\ 10^{-4}$	720 (average)
US beam window of BSG	Ti	0.100 ± 0.001	0.100	260	$3.8\ 10^{-4}$	669
Bias foil of BSG	Al	$0.025 \pm {}^{0.002}_{0.000}$	≈ 0.022 *	372	$0.6\ 10^{-4}$	468
Vertical grid of BSG for hor. profile	Ti	0.012 ± 0.001	≈ 0.0084 **	260	$0.3\ 10^{-4}$	458
Bias foil of BSG	Al	$0.025 \pm {}^{0.002}_{0.000}$	≈ 0.022 *	372	$0.6\ 10^{-4}$	448
Horizontal grid of BSG for vert. profile	Ti	0.012 ± 0.001	≈ 0.0084 **	260	$0.3\ 10^{-4}$	438
Bias foil of BSG	Al	$0.025 \pm {}^{0.002}_{0.000}$	≈ 0.022 *	372	$0.6\ 10^{-4}$	428
DS beam window of BSG	Ti	0.100 ± 0.001	0.100	260	$3.8\ 10^{-4}$	227
Air gap	Air	227	227	$675\ 10^{3}$	$3.4\ 10^{-4}$	113 (average)
Total Loss					$18.7\ 10^{-4}$	

*) Beam size of $\sigma \approx$ 10 mm assumed. Trough hole in BIAS foil of ϕ 10 mm are passing approximately 12% of protons seeing no material. Therefore, the effective average thickness is calculated as follows: thickness · 0.88 = effective thickness

**) Grid pitch 5 mm, strip width 3.5mm, gap 1.5mm. The average effective thickness is given by: thickness · 3.5/5 = effective thickness.

Table 44: Composition of the residual gas in the decay tunnel.

pressure = 2.10^{-2} torr	
hydrogen	51.7 mole %
nitrogen	16.0 mole %
oxygen	2.9 mole %
water	29.3 mole %

APPENDIX G

TABLES

Table 45: (1μ)-events as function of visible energy after scan correction.

E_{shower} > 1.5 GeV or P_μ > 1 GeV		
E_{vis} [GeV]	density 1	density 1/3
1 – 10	519	674
10 – 20	472	628
20 – 30	384	470
30 – 40	281	358
40 – 50	245	253
50 – 60	189	202
60 – 70	140	169
70 – 80	109	130
80 – 90	110	104
90 – 100	88	70
100 – 120	108	104
120 – 140	69	68
140 – 160	49	43
160 – 180	23	30
180 – 400	65	72
≥ 1	2851	3375
≥ 20	1860	2073
≥ 80	512	491

Table 46: (1μ) and (0μ) events as function of shower energy after scan correction.

E_{shower} > 1.5 GeV				
	(1μ)		(0μ)	
E_{shower} [GeV]	density 1	density 1/3	density 1	density 1/3
1.5 – 10	1416	1749	476	558
10 – 20	535	607	315	301
20 – 30	271	340	190	193
30 – 40	171	195	135	125
40 – 50	118	143	97	88
50 – 60	84	89	92	74
60 – 70	66	65	78	67
70 – 80	50	43	55	44
80 – 90	44	34	47	32
90 – 100	22	26	52	32
100 – 120	33	41	64	50
120 – 140	22	16	30	27
140 – 160	11	11	23	15
160 – 180	4	9	10	8
180 – 400	4	7	9	7
≥ 1.5	2851	3375	1673	1621
≥ 20	900	1019	882	762
≥ 80	140	144	235	171

Table 47: Corrected event rates for (1μ) and (0μ) in events/ton/10^{20} pot.

$E_{shower} > 2$ GeV				
	density 1		density 1/3	
E_{shower} [GeV]	(1μ)	(0μ)	(1μ)	(0μ)
2 – 10	681.3± 23.0	295.1± 17.2	1741.3± 52.4	660.7± 38.0
10 – 20	464.9± 19.2	237.9± 14.8	1136.8± 42.8	438.3± 30.2
20 – 30	232.6± 13.8	151.1± 11.5	610.8± 31.9	311.0± 24.1
30 – 40	146.9± 10.9	107.1± 9.7	350.7± 24.2	205.1± 19.4
40 – 50	101.1± 9.0	77.3± 8.2	258.1± 20.8	143.2± 16.3
50 – 60	71.3± 7.6	74.3± 7.9	159.9± 16.4	122.6± 14.9
60 – 70	55.5± 6.7	64.0± 7.3	116.4± 14.0	112.9± 14.2
70 – 80	43.2± 5.9	44.8± 6.1	75.6± 11.3	73.8± 11.5
80 – 90	37.1± 5.5	38.5± 5.7	59.6± 10.1	55.1± 9.8
90 – 100	18.9± 3.9	42.5± 6.0	45.3± 8.9	55.3± 9.8
100 – 120	27.3± 4.8	53.1± 6.6	73.1± 11.1	84.8± 12.3
120 – 140	18.7± 3.8	24.3± 4.6	28.4± 6.9	46.1± 9.0
140 – 160	9.4± 2.8	18.7± 4.0	19.6± 5.8	25.3± 6.7
160 – 180	3.2± 1.6	8.2± 2.6	15.7± 5.2	14.0± 5.0
180 – 400	2.8± 1.4	4.0± 1.8	5.2± 2.9	8.8± 4.0
≥ 2	1914.3± 39.0	1240.9± 33.5	4696.5± 87.4	2357.0± 68.2
≥ 20	768.1± 25.0	708.0± 24.7	1818.4± 55.2	1258.0± 47.9
≥ 80	117.5± 9.8	189.4± 12.7	246.9± 20.5	289.4± 22.6

Table 48: Rates of charged current ν_μ and $\bar{\nu}_\mu$ interactions per ton and 10^{20} POT after unfolding.

	density 1		density $^1/_3$	
E_ν[GeV]	ν_μ	$\bar{\nu}_\mu$	ν_μ	$\bar{\nu}_\mu$
2 – 10	315.1± 27.3	167.8± 22.0	948.4± 130.0	468.2± 47.0
10 – 20	313.2± 21.7	121.0± 11.7	960.5± 83.6	376.5± 32.0
20 – 30	280.9± 18.2	89.4± 11.5	704.2± 42.7	225.1± 22.5
30 – 40	188.1± 14.8	68.3± 8.1	534.7± 36.8	150.8± 16.8
40 – 50	166.9± 13.6	56.4± 7.7	371.7± 28.3	109.6± 18.3
50 – 60	114.0± 10.5	44.4± 6.7	288.0± 24.4	67.6± 11.7
60 – 70	99.0± 10.6	23.2± 5.0	266.6± 25.6	55.0± 10.2
70 – 80	86.9± 9.4	17.6± 4.4	198.9± 22.4	46.6± 9.4
80 – 90	67.6± 7.8	16.9± 3.8	159.3± 18.3	38.4± 9.5
90 – 100	63.1± 8.1	15.4± 3.9	129.3± 18.9	31.6± 8.6
100 – 120	76.5± 9.7	14.4± 5.2	158.0± 18.1	31.5± 8.6
120 – 140	41.0± 7.4	9.2± 3.0	110.3± 15.6	9.6± 3.0
140 – 160	30.6± 6.8	7.8± 2.6	52.1± 11.6	6.4± 2.3
160 – 180	24.7± 7.0	3.2± 1.6	45.3± 10.6	0.8± 0.6
180 – 400	21.0± 3.2	3.0± 0.4	49.1± 4.21	3.2± 0.1
≥ 2	1888.6± 51.5	658.0± 32.3	4976.4± 176.4	1620.9± 70.3
≥ 20	1260.3± 37.8	369.2± 20.6	3067.4± 85.2	776.2± 41.2
≥ 80	324.5± 19.6	69.9± 8.7	703.4± 39.1	121.5± 15.9

Table 49: Rates of charged current ν_e and $\bar{\nu}_e$ interactions per ton and 10^{20} POT from unfolding the $(0\mu) - 0.33 \cdot (1\mu)$ spectrum.

E_ν [GeV]	density 1	density $^1/_3$
2 – 10	25.4± 7.0	41.3±21.5
10 – 20	52.0±10.1	41.7±23.5
20 – 30	60.0±10.1	88.7±21.8
30 – 40	51.2± 9.1	77.0±18.3
40 – 50	37.5± 7.5	48.5±15.0
50 – 60	45.5± 7.5	61.3±14.0
60 – 70	38.4± 6.5	62.0±12.5
70 – 80	25.4± 5.4	41.4±10.3
80 – 90	22.0± 5.0	28.6± 8.4
90 – 100	30.6± 5.2	33.3± 8.5
100 – 120	35.9± 5.5	50.5±10.7
120 – 140	14.2± 3.8	26.7± 6.8
140 – 160	10.5± 2.8	13.8± 5.1
160 – 180	5.3± 2.0	6.3± 3.8
> 180	1.5± 0.9	3.3± 1.9
≥ 2	464.0±27.7±17.0	612.4±57.4±44.0
≥ 20	379.6±21.9±11.0	545.5±43.0±23.0
≥ 80	120.6±10.5± 2.0	164.2±18.7± 3.0

Table 50: Rates of prompt charged current ν_e and $\bar{\nu}_e$ interactions per ton and 10^{20} POT, conventional background from M.C. subtracted.

E_ν [GeV]	rate
2 – 10	2.5± 8.7
10 – 20	23.7±10.6
20 – 30	37.0± 9.5
30 – 40	35.5± 8.6
40 – 50	28.4± 7.6
50 – 60	39.1± 7.5
60 – 70	36.1± 6.9
70 – 80	23.4± 5.6
80 – 90	20.2± 5.1
90 – 100	28.7± 5.1
100 – 120	34.0± 5.6
120 – 140	13.2± 3.7
140 – 160	11.5± 3.1
160 – 180	4.9± 2.0
> 80	4.0± 1.7
≥ 2	342.2±27.5±26.1
≥ 20	316.2±21.7±14.4
≥ 80	116.5±10.7± 4.4

APPENDIX H

LIST OF COMMONLY USED ABBREVIATIONS

ADC = Analog to Digital Converter
BCT = Beam Current Transformer
BR = Branching Ratio
BSG = Beam Scan Grid
CAMAC = Computer Aided Measurement And Control
CC = Charged Current
CL = Confidence Level
CM = Centre of Mass
DAQ = Data Acquisition
DMA = Direct Memory Acces
DS = Down Stream
E_{had} = Hadronic Energy
EMA = Extended Memory Area
E_{sh} = Shower Energy
E_{vis} = Visible Energy
FWHM = Full Width at Half Maximum
MC = Monte Carlo
MIP = Minimum Ionizing Particle
MTBF = Mean Time Between Failures
MWPC = Multi Wire Proportional Chamber
NBB = Narrow Band Beam
NC = Neutral Current
NFM = Neutrino Flux Monitor
PDT = Proportional Drift Tube
PM = Photo Multiplier (tube)
POT = Protons On Target
QED = Quantum Electro Dynamics
QCD = Quantum Chromo Dynamics
RMH = Receiver-Memory-Hybrid
SEM = Secundary Emision Monitor
SPS = Super Proton Synchrotron
ST = Streamer Tube
US = Up Stream
WBB = Wide Band Beam

SUMMARY

In this thesis the results of a 400 GeV proton on copper beam dump experiment performed at the European centre for high energy physics CERN in Geneva are described, concerning the production of prompt neutrinos and muons.
The CHARM-I neutrino detector, a fine-grained sampling calorimeter with large fiducial mass, was used to record neutrino interactions. The muon energy spectrum was determined by measuring the muon flux at several depths in an iron muon shield just downstream of the dump.
The prompt event rates were separated from the conventional event rates by the technique of extrapolation to "infinite" target density. Two targets of different density were used, one made of solid copper and a copper/air segmented one, with one-third density of the first.
The distance between dump and neutrino detector was 490 m.
The amount of protons on the high density target was $13.26 \cdot 10^{17}$ and on the low density target $6.35 \cdot 10^{17}$.

The asymmetry between prompt muon neutrinos and prompt electron neutrinos was found to be $(\nu_\mu - \nu_e)/(\nu_\mu + \nu_e) = 0.21 \pm 0.08 \pm 0.03$ for neutrino energy above 20 GeV. A review of results from other experiments on this asymmetry is presented.
The production of charmed hadrons is discussed. A cross-section for the production of D-mesons was found of $\sigma_{D\bar{D}} = 921 \pm 150$ (stat.) $\pm$ 149 (syst.) per nucleus for 400 GeV protons on copper with A = 63.5 .
For the relative coupling strengths of ν_e and ν_μ to the weak neutral current a value of $g_{\nu_e \bar{\nu}_e}/g_{\nu_\mu \bar{\nu}_\mu} = 1.05 + 0.15 - 0.18$ is derived. This value is in agreement with universality of electron neutrino and muon neutrino for the weak interaction.
Concerning the production of tau neutrinos, an 90 % C.L. upper limit was found for the tau-neutrino flux of < 13 % of the total prompt neutrino flux.
An upper limit for the branching ratio of the decay of the neutral pion in a neutrino anti-neutrino pair is determined of $BR(\pi^0 \rightarrow \nu\bar{\nu}) < 6.5 \cdot 10^{-6}$ with 90 % C.L. .

SAMENVATTING

In dit proefschrift worden de resultaten beschreven van een 400 GeV proton beamdump experiment, uitgevoerd in het Europese centrum voor hoge energie fysica CERN te Geneve. Gekeken is naar de productie van prompte neutrinos en muonen. De dumps waren vervaardigd van koper.
De CHARM I neutrino detector is gebruikt voor de detectie van neutrino interacties. Deze detector bestond uit een bemonsterende calorimeter met fijne granulariteit en hoge fiduciale massa. Het energie spectrum van muonen werd bepaald door het meten van de muon flux op verschillende diepten in het ijzeren muonschild, onmiddellijk benedenstrooms van de dump.
De prompte interacties werden gescheiden van de conventionele interacties d.m.v. extrapolatie naar "oneindige" dump dichtheid. Hiertoe werden twee dumps van verschillende dichtheid gebruikt, een gemaakt van massief koper, de andere was gesegmenteerd, i.e. koper van luchtspleten voorzien met een gemiddelde dichtheid van eenderde van de eerstgenoemde.
De afstand tussen dump en neutrino detector bedroeg 490 m.
De hoeveelheid protonen op de dump met hoge dichtheid bedroeg $13.26 \cdot 10^{17}$, op de dump met lage dichtheid $6.35 \cdot 10^{17}$.

Als asymmetrie in de hoeveelheid prompte muon neutrinos en prompte elektron neutrinos werd gevonden $(\nu_\mu - \nu_e)/(\nu_\mu + \nu_e) = 0.21 \pm 0.08 \pm 0.03$, voor neutrino energie groter dan 20 GeV. Een overzicht van resultaten betreffende deze asymmetrie van andere experimenten wordt gegeven.
De productie van hadronen met quantum nummer charm $= \pm 1$ wordt bediscussieerd. Voor the werkzame doorsnede voor de productie van D-mesonen in interacties tussen 400 GeV protonen en koper kernen (A = 63) werd gevonden: $\sigma_{D\bar{D}} = 921 \pm 150$ (stat.) $\pm$ 149 (syst.) per nucleus.
Voor de relatieve koppelings sterkte van ν_e en ν_μ ten opzichte van de zwakke neutrale stroom werd een waarde $g_{\nu_e\bar{\nu}_e}/g_{\nu_\mu\bar{\nu}_\mu} = 1.05 + 0.15 - 0.18$ gevonden. Deze waarde is in overeenstemming met universaliteit van electron neutrino en muon neutrino voor the zwakke wisselwerking.
Een bovengrens werd gevonden voor de tau neutrino flux van 13 % van de totale prompte neutrino flux, met 90 % confidentie niveau.
Voor the kans op verval van het neutrale pion in een neutrino en een anti-neutrino werd gevonden $P(\pi \to \nu\bar{\nu}) < 6.5 \cdot 10^{-6}$ met 90 % confidentie niveau.

ACKNOWLEDGEMENTS

I thank the members of the CHARM-collaboration for their pleasant cooperation and especially for helping me with some subjects which entered into this thesis.

I am grateful to Prof. J. Ranft and Dr. P. A. Aarnio for the many questions they answered about the FLUKA Monte Carlo.

I thank Dr. Dafydd Thomas and Dr. Werner Herr for the careful reading of the manuscript.

STELLINGEN

1. Recente resultaten van LEP experimenten betreffende het verval van het Z-boson in onzichtbare vervalsproducten worden gebruikt om te bewijzen dat er drie typen neutrinos bestaan. Deze resultaten geven echter ook niet-triviale beperkingen op het gepostuleerde bestaan van supersymmetrische deeltjes.

2. In het artikel van Abe et al., "Determination of $\sin^2\Theta_W$ from Measurements of Differential Cross Sections for Muon-Neutrino and Anti-Neutrino Scattering by Electrons", is de bepaling van $\sin^2\Theta_W$ niet gebaseerd op de meting van de differentiele werkzame doorsnede $d\sigma/dy$.

   K. Abe et al., Phys. Rev. Lett. 62 (1989) 1709.

3. Het is mogelijk met behulp van een kathode, voorzien van een dunne laag amorf, gehydrogeniseerd silicium van de juiste specifieke weerstand, een snelle parallelle plaat detector (PPC) te maken, die signalen van enige tientallen pC per passerend minimum ioniserend deeltje geeft en niet buitensporig duur is.

4. In een beamdump experiment met hoge bundel energie is het aantal neutrinos veroorzaakt door K_{l3}-verval van K^0_L en K^0_S vrijwel gelijk.

   Dit proefschrift, pagina 51 tabel 8, pagina 56 tabel 13.

5. De LHC zal met de huidige ontwerp parameters geen luminositeit van $4{\cdot}10^{34}$ $cm^{-2}s^{-1}$ kunnen bereiken, vanwege instabiliteiten ontstaan door bundel-bundel interacties met lange dracht.

   C. Rubbia, perspectives for a hadron collider in the LEP tunnel, voordracht 2 nov. 1989 CERN.

6. Het is voordeliger, ter bestreiding van de NOx-emissie van kolen gestookte centrales, het verbrandings proces te veranderen, dan na afloop de verbrandings gassen chemisch te zuiveren.

   F. Bergsma (sr), Ind. Eng. Chem. Process Des. Dev. 1985, 24, 1-7

7. De werking van oppervlakte deeltjes detectoren, gebaseerd op een smalle geleidende strip als anode aangebracht op een isolator (micro strip detector) of een doorgeplateerd gat als anode in een isolerende folie (hole chamber), wordt sterk beinvloed door ladings transport over het isolerende oppervlak tussen annode en kathode; gezien de afstand van enige millimeters tussen anode en kathode in het tweede voorbeeld is het twijfelachtig dat dit idee ooit zal leiden tot een bruikbare detector.

   A. Oed, Nucl. Instr. Meth. A263 (1988) 351; Proc. of ECFA Study Week on Instrumentation Technology for High-Lumininosity Hadron Colliders, 14-21 sept. 1989 Barcelona Vol. 2 p 435 .

8. Bundels in supergeleidende versnellers zijn moeilijker te controleren dan bundels in versnellers met conventionele magneten vanwege een reductie in dynamische apertuur, veroorzaakt door hogere orde multipool bijdragen tot het magnetische veld.

9. Door het continu registreren van de draaihoek van de diverse tandwielen en servo sturing van gangwissel, koppeling en gas kan een efficiente en mechanisch eenvoudige automatische versnellingsbak voor automobielen gemaakt worden.

10. Met behulp van de laser techniek, ontwikkeld voor compact disc spelers, is het mogelijk nauwkeurige plaats en hoek encoders te maken.

CERN, 16 februari 1990 Felix Bergsma